Experimental Studies of Cluster Ions Containing Water, Ammonia, Pyridine and Bisulphate

Mauritz Johan Ryding

THESIS FOR THE DEGREE OF
DOCTOR OF PHILOSOPHY IN NATURAL SCIENCE, SPECIALISING IN CHEMISTRY

UNIVERSITY OF GOTHENBURG

Department of Chemistry
University of Gothenburg
Göteborg, Sweden, 2011

Experimental studies of cluster ions containing water, ammonia, pyridine and bisulphate

Mauritz Johan Ryding

ISBN 978-91-628-8332-4
Available online at http://hdl.handle.net/2077/26671

Department of Chemistry
University of Gothenburg
SE-412 96 Göteborg
Sweden

Printed by Kompendiet
Göteborg, Sweden 2011

So great a writer, all men swore,
They never had not read before.

Ambrose Bierce (1842–1914)
The Devil's Dictionary

Abstract

Molecular cluster ions are fascinating subjects of study. Bridging the size gap between molecules and bulk, they often display non-trivial size dependent behaviour and properties. As an example, for some cluster types there are certain sizes that are found in unusually high abundance in a produced cluster distribution, these are referred to as “magic numbers”. Apart from being interesting in their own right and serving as useful model systems in a number of applications, molecular clusters have a very real and important role in the vast and dynamic system we refer to as the atmosphere. Molecular clusters act as precursors for the formation of atmospheric particles. As such, it is necessary to learn as much as possible about the formation, growth, physical properties and chemistry of these clusters, because the particles they form will ultimately have a large effect on the global climate.

This work investigates the properties of some ionic molecular clusters and their gas phase reactions with heavy water and ammonia, and also the effects of collision induced dissociation on air. This is done in cluster beam experiments, using two different experimental setups.

The first instrument is a quadrupole-time-of-flight instrument, consisting of an electrospray ion source, a quadrupole mass filter, a collision cell and a time-of-flight mass spectrometer. In this instrument, relative reaction cross sections were measured for $H^+(H_2O)_n$, $H^+(NH_3)_1(H_2O)_n$ and $H^+(\text{pyridine})_{1-3}(H_2O)_n$ colliding with D_2O; and for $H^+(H_2O)_n$, $H^+(\text{pyridine})_{1-2}(H_2O)_n$ and $H^+(NH_3)_1(\text{pyridine})_1(H_2O)_n$ colliding with NH_3. The results for the reaction $H^+(\text{pyridine})_1(H_2O)_n + NH_3$ were used to improve a kinetic model of the atmospheric positive ion composition. Abundance spectra and evaporation patterns were recorded for all clusters. It was found that protonated clusters containing water and pyridine do not have magic numbers in the investigated size range (≤ 1500 u), unlike clusters consisting of water, pyridine and ammonia. Furthermore the magic numbers of $H^+(NH_3)_1(\text{pyridine})_1(H_2O)_n$ were the same as those recorded for $H^+(NH_3)_1(H_2O)_n$. Cluster reactions with D_2O proceed through a short-lived reaction complex. The clusters add the heavy water molecule and subsequently lose a D_2O, HDO or H_2O molecule; the latter two reaction channels are associated with a cluster mass increase of one or two atomic mass units, respectively. The formation of a HDO species in a cluster requires proton mobility, and is known to occur in $H^+(H_2O)_n$ clusters. The reaction channel leading to formation of HDO was not observed for protonated water clusters containing an ammonia or pyridine molecule, which is attributed to the proton being bound in place by the Brønsted base. However, the experiments indicate proton mobility in clusters with two or three pyridine molecules, $H^+(\text{pyridine})_{2-3}(H_2O)_n$. Quantum chemical calculations suggest that this may be due to transfer of the proton to a water molecule, forming H_3O^+, or due to proton transfer between the two pyridine molecules along a wire of hydrogen bonds.

The second instrument is a double sector instrument, having a magnetic sector, a collision cell and an electrostatic sector. Collision induced dissociation of $H^+(NH_3)_m(H_2O)_n$ clusters (m = 4–6) indicate that clusters having six NH_3 prefer to lose NH_3, while clusters with four or five NH_3 prefer to lose H_2O.

List of publications

Paper I

Isotope exchange and structural rearrangements in reactions between size-selected ionic water clusters, $H_3O^+(H_2O)_n$ and $NH_4^+(H_2O)_n$, and D_2O

Patrik U. Andersson, Mauritz J. Ryding, Osamu Sekiguchi and Einar Uggerud

Physical Chemistry Chemical Physics, 2008. ***10****(40): p. 6127-6134.*

Paper II

Isotope exchange in reactions between size-selected ionic water clusters, $H^+(pyridine)_m(H_2O)_n$, and D_2O

Mauritz J. Ryding, Alexey S. Zatula, Patrik U. Andersson and Einar Uggerud

Physical Chemistry Chemical Physics, 2011. ***13****(4): p. 1356-1367.*

Paper III

Proton mobility and stability of water clusters containing the bisulfate anion, $HSO_4^-(H_2O)_n$

Alexey S. Zatula, Patrik U. Andersson, Mauritz J. Ryding and Einar Uggerud

Physical Chemistry Chemical Physics, 2011. ***13****(29): p. 13287-13294.*

Paper IV

Reactions of $H^+(pyridine)_m(H_2O)_n$ and $H^+(NH_3)_1(pyridine)_1(H_2O)_n$ with NH_3: experiments and kinetic modelling under tropospheric conditions

Mauritz J. Ryding, Åsa M. Jonsson, Alexey S. Zatula, Patrik U. Andersson and Einar Uggerud

Atmospheric Chemistry and Physics Discussions, 2011. ***11****(9): p. 24535–24566.*

Paper V

Structural rearrangements and magic numbers in reactions between pyridine containing water clusters and ammonia

Mauritz J. Ryding, Patrik U. Andersson, Alexey S. Zatula and Einar Uggerud

Manuscript in preparation

Paper VI

Stability and Structure of Protonated Clusters of Ammonia and Water, $H^+(NH_3)_m(H_2O)_n$

Preben Hvelplund, Theo Kurtén, Kristian Støchkel, Mauritz J. Ryding, Steen Brøndsted Nielsen and Einar Uggerud

Journal of Physical Chemistry A, 2010. ***114****(27): p. 7301-7310.*

Table of Contents

1 Introduction

Apart from being fascinating subjects of scientific study in their own right, molecular clusters play an important role in many different areas of scientific and common interest. For instance, molecular clusters play a major role in the atmosphere by acting as precursors for secondary particle formation. Uncertainties associated with the abundance and properties of clusters contribute to the uncertainties connected with atmospheric particles in general. The aerosol effect is a primary uncertainty in prediction of changes in the greenhouse effect and global temperature [1]. Molecular clusters are also of interest from the perspective of air quality and human health, because the clusters—being of nanometre size—can penetrate to the deepest part of the human respiratory tract.

This work deals with the experimental study of charged clusters consisting of water, ammonia, pyridine and bisulphate and the way these clusters react with D_2O and NH_3. Prior to these studies, many of the cluster types had not been investigated experimentally. The motivation for these experiments stems from the relevance of the clusters for atmospheric chemistry. For instance, in what way does the reaction cross section of clusters vary with size, and how do the reaction mechanisms change? Clusters often exhibit non-trivial size dependence; for instance the so-called magic numbers, clusters having an abnormally high abundance compared to their peers. Which cluster types have magic numbers, and are magic numbers important from an atmospheric chemistry perspective? Will clusters with magic numbers have a greater or lesser reaction cross section than expected and will magic numbers influence which reactions that take place?

The clusters were studied by cluster beam experiments, in which cluster ions were produced by an ion source and transferred into a high vacuum instrument where they underwent gas phase reactions or were made to collide with air, resulting in collision induced dissociation. Spontaneous loss of water molecules from clusters was also investigated in order to establish evaporation patterns. Some of the questions put forward above were answered by the experiments, while new intriguing enigmas arose. The experiments were supported with quantum chemical calculations of cluster structure and reaction transition states in order to shed additional light on the findings. Experimental results were also used to refine kinetic modelling efforts of atmospheric ion abundances.

This introduction is followed by Chapter 2 where a general background of the Earth's atmosphere and the atmospheric role of molecular clusters in it is discussed. Chapter 2 also provides information on working with cluster ions experimentally, and gives additional theoretical context for the particular reactions studied. Chapter 3 deals with the two different experimental setups used: a quadrupole time-of-flight unit (QTOF) that was used in the experiments presented in Papers I–V, and a double sector mass spectrometer used for the experiments presented in Paper VI. Results are summarised in Chapter 4 followed by some final conclusions and an outlook in Chapter 5 and Chapter 6, respectively.

2 Background

2.1 The atmosphere of Earth

The Earth's atmosphere is the layer of gas and ions surrounding the Earth. Since there is no sharp limit between the outer atmosphere and space in terms of pressure, the altitude where the atmosphere ends is somewhat arbitrary. Air, in the sense of a uniform gas mixture of primarily nitrogen and oxygen, is found below 80 km above the surface. Compared to the radius of the Earth itself—on average 6378 km at the equator [2]—this is a rather thin shell.

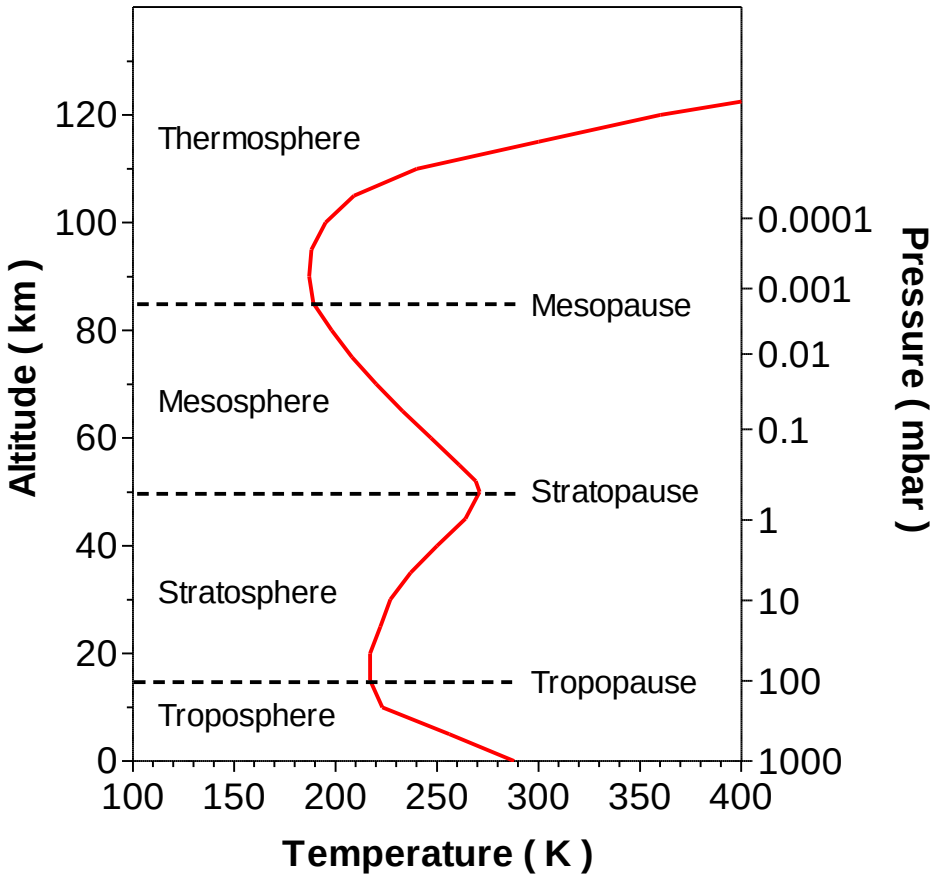

Figure 1. Temperature profile of the atmosphere. Adapted from Brasseur and Solomon [3].

While the atmospheric pressure decreases with height in a roughly exponential manner [4], temperature both decreases and increases with altitude, as seen in Figure 1. The atmosphere can be divided into different zones based on the way the temperature or other properties vary with height.

The atmosphere below 80 km is known as the homosphere, because the composition of the air is a uniform mixture. Above this is the heterosphere, where stratified layers begin to emerge in the gas composition. Heavier species such as molecular nitrogen and oxygen are found in the lower layers and lighter species such as helium atoms and finally hydrogen atoms are found in the higher layers [5]. The ionosphere is the region

of the atmosphere where free ions are readily produced by solar radiation or galactic cosmic rays and ranges from 60 km and up [4, 5].

The different zones of the atmosphere as divided by temperature are as follows. The troposphere is the zone of the atmosphere closest to earth. The tropospheric boundary layer is the region of the troposphere that is directly influenced by the surface. The free troposphere then extends to about 12 km above the surface (higher in the tropics, lower in the Polar Regions). Because the ground is heated by solar radiation the temperature near the Earth's surface is higher, and drops off at an average rate of 6.5 K per kilometre [5]. Since warm air is lighter than cold air, the troposphere is characterised by a high degree of vertical mixing of air masses. Above the troposphere—and separated from this by the tropopause—lies the stratosphere. Within the stratosphere is the ozone layer, which absorbs solar UV radiation, heating this region and causing a temperature inversion. The stratosphere takes its name from the stratified nature of the air layers here, a consequence of the stability imposed by a temperature that increases with height. The exchange of air masses between the troposphere and the stratosphere is also a limited. Above the warming effect of the ozone layer, there is the layer called the mesosphere, where temperature once again decreases with height. The upper limit is marked by the mesopause, which is the coldest region of the atmosphere. The final layer, the thermosphere, is characterised by very low pressure and a temperature that is increasing again due to absorption of high energy radiation from the sun. The mean free path in the thermosphere is so long, that temperatures of 1000 °C can be reached. However, because the gas particles are so scarce, the heat capacity of the thermosphere is very small [5].

2.2 Aerosols and molecular clusters in the atmosphere

2.2.1 General properties of aerosols

An aerosol is a dispersion consisting of solid or liquid particles in a gas. Atmospheric aerosols are thus particles in the atmosphere and the surrounding air that they are dispersed in. The atmosphere is an ever changing and very complex system; it follows that atmospheric aerosols also have these attributes with size and concentration varying with region, time and altitude. The majority of the total atmospheric particle mass can be found in the troposphere with concentrations up to 10^8 cm^{-3} [6, 7].

Particle diameter spans several orders of magnitude, from a few nanometres to a few tenths of a millimetre or so, the limits are somewhat arbitrary. For practical purposes we can consider a reasonable size range of particles to be between 3 nm and 100 μm in diameter [6]. Several properties of particles—such as charging limit and settling velocity—do not depend on the diameter; instead they vary with the surface or volume, resulting in a squared or cubed size range [6]. Particle concentrations are usually given as the number of particles per volume or total particle mass per volume. The fact that the volume of a particle can range some 15 orders of magnitude, combined with the very low number of large particles compared to the smallest ones, means that it is difficult to represent the entire size range with the same property.

The particle concentration (in number of particles or in mass) in the troposphere is not uniformly distributed with size. Rather, it is typically found as several log-normal[a] distributions referred to as "modes". Whitby *et al.* [8-10] initially suggested three modes to describe atmospheric aerosols, but presently four are often used: *ultrafine mode (sometimes called nucleation mode), nuclei (Aitken) mode, accumulation mode* and *coarse mode* [7]. Each size mode represents particles with different sources, formation mechanisms, chemical compositions, and paths of removal from the atmosphere. Furthermore, all modes are not always present in all air masses. A summary of the different modes is given in Table 1.

Table 1. Particle modes in tropospheric aerosols.

Mode	**Ultrafine**	**Nuclei**	**Accumulation**	**Coarse**
Size range (µm)	≤ 0.01	0.01–0.08	0.08–about 2	about 2–100
Sources	Gas-to-particle conversion.	Gas-to-particle conversion. Direct emission from combustion.	Combustion, smog. Growth of smaller particles by gas condensation. Coagulation of smaller particles, with themselves or with Acc. mode particles.	Mechanical abrasion, desert dust, salt particles from sea-spray. Biological particles (pollen, spores *etc.*).
Composition	Sulphates, water, organics. Possibly amines.	Elemental carbon, organics and low volatile gases.	Hygroscopic organics, water, water soluble inorganics.	Minerals, inorganics and organics.
Removal	Growth into nuclei mode particles.	Growth into Acc. mode particles by coagulation or gas condensation. Rainout.	Rainout, washout.	Settling or impact at ground level. Washout.
Atmospheric lifetime		Minutes to hours.	Several days.	Few hours or few days.
Total number	Significant.	Most.	Few percent.	Less than few percent.
Total mass	Insignificant.	Least.	Large part.	Large part.

Summarised from Finlayson-Pitts and Pitts [7] and Hinds [6]. Input also from Kurtén et al. *[11].*

[a] A particle log-normal distribution is when the particle concentration is a Gaussian distribution when plotted as a function of the logarithm of the particle size (such as the diameter).

Large particles are too heavy to diffuse. However, they readily settle due to gravity. Small particles are too light to be affected by gravitational settling. In contrast, they diffuse rapidly by Brownian motion and consequently tend to coagulate *i.e.* collide with each other to form larger particles. While coagulation can happen between particles in the same size mode, it is generally a quicker process between particles of different sizes because it combines the faster diffusion of smaller particles with the high surface area of larger particles [7]. Smaller particles can also be removed by rainout, when water droplets form around the particles and falls to the ground. Larger particles can be absorbed by falling raindrops, a process referred to as washout. Accumulation mode particles neither settle nor coagulate to any significant extent; thus, they are typically removed by rainout and washout which accounts for their longer atmospheric residence time compared to coarse or nuclei mode particles [7].

The primary stratospheric particle is a small (a few hundred nm) droplet of sulphuric acid and water. The main source of the sulphuric acid is believed to be conversion from SO_2 emitted into the stratosphere by volcanic eruptions. The stratified nature of the air layers means that there is little mass exchange in the vertical direction in the stratosphere. Hence, the particles have lifetimes of several months and up to a year and spread globally [12].

2.2.2 Effects of atmospheric aerosols on climate

According to the latest report on climate change by the Intergovernmental Panel on Climate Change (IPCC) [13], the influence of human activities on the climate is much larger than what is expected without any human input. Figure 2 shows the modelled change in radiative forcing for different contributing factors such as CO_2, surface albedo and contrails relative to the pre-industrial era. The radiative forcing—as defined here—is the change in net irradiance (the difference in incoming and outgoing radiation energy) at the tropopause, assuming fixed tropospheric and surface temperatures but allowing the stratospheric temperature to equilibrate. The radiative forcing of CO_2 is 1.66 Wm^{-2}, meaning that since the pre-industrial era, the difference between incoming and outgoing radiative energy has increased by 1.66 W for each square meter of the tropopause. As seen from the IPCC estimate, the overall influence of particles (total aerosol) is atmospheric cooling; however there are large uncertainties regarding the magnitude and a low level of scientific understanding.

The influences of particles on global warming takes place through several different mechanisms. There are the direct effects, for instance reflection and absorption of radiation by atmospheric particles themselves or deposition of particles on snow and ice leading to lower albedo of the snow cover. The indirect effects are aerosol effects on cloud formation and chemistry. Aerosol particles acts as cloud condensation nuclei, *i.e.* they act as the seed around which a cloud droplet forms. With more cloud condensation nuclei available, the clouds formed have a larger quantity of droplets that are smaller in size compared to a normal cloud. This has two effects: firstly, the cloud becomes whiter and has a higher radiative albedo; secondly, the lifetime of the cloud increases since precipitation is suppressed when the droplets are smaller. In the fourth IPCC assessment report these are referred to as the cloud albedo effect and the cloud lifetime effect.

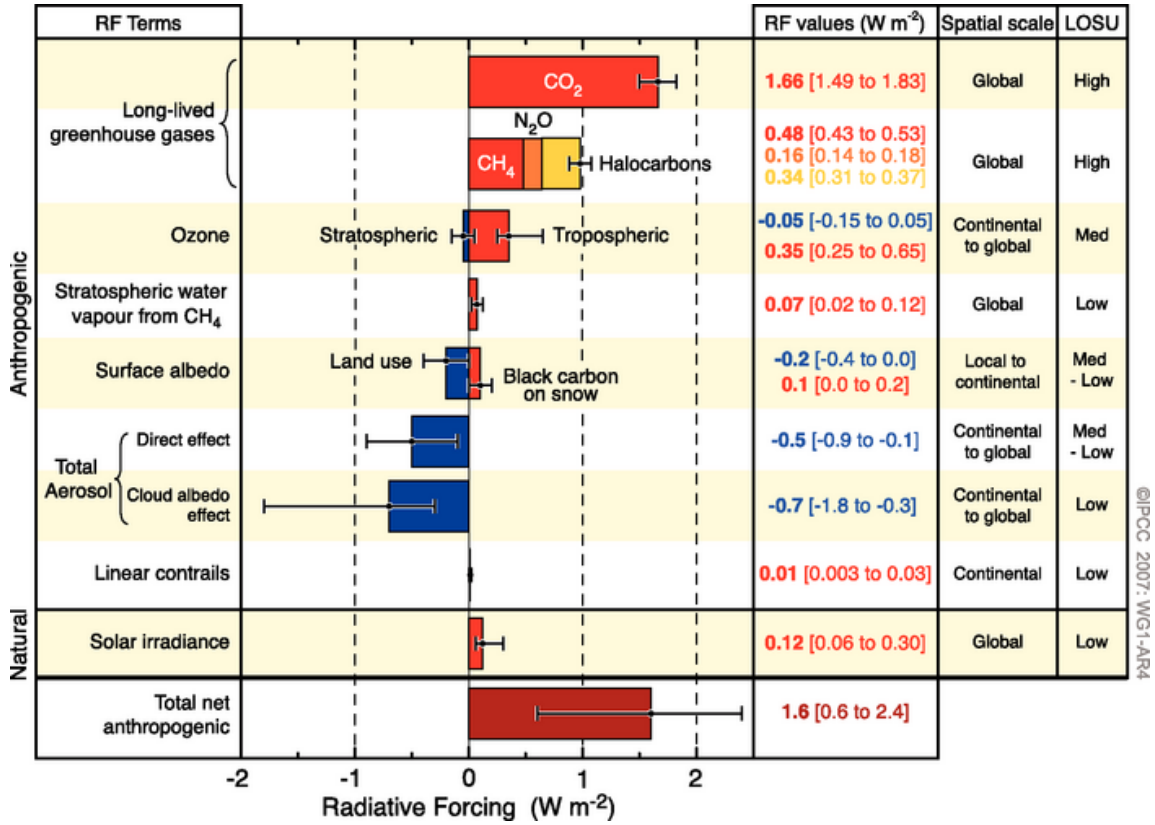

Figure 2. Estimated Impact on average global atmospheric radiative forcing (RF) from different sources due to human influence for 2005. Also indicated is the level of scientific understanding (LOSU) of those sources. Taken from the fourth Assessment report of the IPCC [1] (WGI Figure SPM.2).

As seen from the total net anthropogenic radiative forcing in Figure 2, the major uncertainties in current estimates of global warming stem from the effects of aerosols. Therefore, progress in our understanding of the topic is necessary in order to correctly estimate the magnitude of climate change.

2.2.3 Impact of aerosols on health

In urban areas, particle emission from combustion and other aerosol sources affect the health and well-being of humans.

Humans process 10–25 m^3 of air during a normal day [6]. Naturally, quite a few particles enter our respiratory system. The respiratory system has several ways of removing particles before the inhaled air reaches the alveoli in the deepest part of the lungs. The respiratory system can be seen as a branching network where the air passages becomes finer and finer. In the upper airways, larger particles are removed by inertial impaction to the walls as the airflow changes direction; further down, smaller particles are deposited by gravitational settling and diffusion to walls of small airways [6]. Once deposited to a wall, the particles are removed by the mucociliary escalator or by macrophages. The number of particles that can reach the deepest parts of the lungs is dependent upon aerodynamic size, density and shape. Smaller particles penetrate more readily into the alveolar region of the lungs, and are therefore a greater risk to human health. Hughes *et al.* [14] found that 10^{11} ultrafine particles are deposited each day in the respiratory tract of a person living in the Los Angeles area. From an air quality

perspective, particle concentrations are often measured as total mass load of particulate matter with aerodynamic size below 10 or 2.5 micrometres, referred to respectively as PM_{10} and $PM_{2.5}$. Colbeck and Lazaridis [15] noted that several studies have shown that increased levels of $PM_{2.5}$ lead to lowered life expectancy, by about a year for a $PM_{2.5}$ increase of 10 μgm^{-3}. Colbeck and Lazaridis also note that a recent study by Pope *et al.* [16] indicate that lowering $PM_{2.5}$ by the same amount (10 μgm^{-3}) leads to an increase in life expectancy of 0.61 ± 0.2 years. However, there is still a considerable uncertainty with respect to which physical or chemical properties of the particles that have the largest impact on health, and by which mechanisms they work.

2.2.4 Sources of atmospheric aerosols

There are several ways to form atmospheric aerosols and they vary with the part of the atmosphere that is considered, which part of the globe, and what the local conditions are. Naturally, the properties of particles depend on their origin. Therefore, the particles are often divided according to their source, *e.g.* natural or anthropogenic particles, primary or secondary particles. Anthropogenic sources are "man-made", such as combustion of fossil fuels, while natural sources are those occurring without the influence of man. The distinction between anthropogenic sources and natural sources can be blurry, for example, the difference between particles from natural forest fires contra forest fires due to human action. On the global scale, natural sources dominate the total emitted particulate mass. However, anthropogenic emissions dominate in densely populated and industrialised areas [6].

A primary particle source is one where the particles are emitted directly into the atmosphere, while a secondary source is one where particles are formed by reactions of gaseous substances in the atmosphere [7]. Examples of primary sources are combustion, mechanical wear and tear, salt particles from sea-spray, pollen, desert dust, *etc.* [7]. As mentioned above, "mechanically" generated particles tend to be large and fall in the coarse mode size range, while combustion produced particles are found in the nuclei mode and accumulation mode size ranges.

The formation of aerosols in the atmosphere (*i.e.* secondary atmospheric aerosols) is a complex process which varies with height, location and time of day; all mechanisms and steps are not fully understood. In the continental boundary layer, secondary particle formation can typically be divided into two parts. First the formation of a charged or neutral molecular cluster—sometimes referred to as a nanometre sized condensation nuclei, or nano-CN. Once formed, the cluster grows into a particle [17]. Formation of clusters and particles in the atmosphere will be covered in the following sections.

2.2.5 Formation of molecular clusters in the atmosphere

Four different processes are often suggested as the main mechanisms for formation of nano-clusters: binary homogeneous nucleation by water and sulphuric acid; ternary homogeneous nucleation of water, sulphuric acid and ammonia; homogeneous nucleation by iodine species; and ion-induced nucleation of the binary or ternary type or with organic species [17]. Other mechanism have also been suggested and investigated, such as involvement of amines other than ammonia. Modelling work by Kurtén *et al.* [11] on the binary reactions between H_2SO_4 and HSO_4^- with eight different amines found in the atmosphere (ammonia, methylamine, dimethylamine, diethylamine,

etc.) indicate that the amines were more effective than ammonia in enhancing condensation of sulphuric acid molecules on sulphuric acid/amine clusters, both for charged and neutral clusters.

The different mechanisms mentioned above vary not only by the difference in participating substances. They are also linked to the difference in environments where the mechanisms are observed. Binary homogeneous nucleation of water and sulphuric acid is expected only in places with high abundance of these two compounds, such as industrial plumes. Ternary homogeneous nucleation is suggested as the mechanism for nucleation in the continental boundary layer. Homogeneous nucleation of iodine species is observed in the coastal boundary layer [17, 18]. Ion-induced nucleation is thought to be most important in the upper troposphere and lower stratosphere [17-19].

Homogeneous nucleation is a process by which particles are formed from supersaturated gases without help from ions or condensation nuclei, only the gases that condense take part in the process. In contrast, heterogeneous nucleation involves ions or condensation nuclei as a starting point for growth. There is some ambiguity in what is implied by the terms, arising from looking at particle formation on different size scales. The secondary atmospheric particles are—as mentioned above—likely formed by growth around a molecular cluster, *i.e.* heterogeneous nucleation. The cluster itself can be formed by both heterogeneous nucleation (with ions) and homogeneous nucleation (binary, ternary or iodine species). Furthermore, secondary particles can act as cloud condensation nuclei, leading to heterogeneous formation of cloud droplets.

Homogeneous nucleation of pure water particles does not happen readily in the atmosphere, due to the difficulties of forming a stable neutral pure water cluster, $(H_2O)_n$, without very high supersaturation levels (at room temperature a saturation ratio of 3.5 is required [6]). This is attributed to the Kelvin effect: the equilibrium vapour pressure is higher above a curved surface than above a flat surface. For a given level of supersaturation the consequence is that droplets below a certain size will evaporate since the molecules leave the surface more readily as the curvature increases. However, particles above a certain size will grow. The size where the droplet will neither shrink nor grow is the Kelvin diameter for that particular saturation ratio. For most atmospheric levels of air water-content, the Kelvin diameter is so large that any neutral water clusters will evaporate before having a chance to reach the critical diameter [6]. In contrast to homogeneous nucleation, heterogeneous nucleation of water usually requires just a few percent of supersaturation, and can sometimes happen even below supersaturation. Thus, heterogeneous nucleation is the primary mechanism for atmospheric cloud formation [6]. Heterogeneous nucleation works in different ways for different types of nuclei: an insoluble nuclei in a droplet leads to a larger "starting size" compared to homogeneous nucleation, *i.e.* it is easier for the particle to reach the critical Kelvin diameter needed for growth; the presence of a charge adds stability to a cluster (especially if the molecules are strong dipoles) and enhances the initial growth rate by electrostatic attraction of the dipoles in the gas phase; the presence of a soluble salt, such as NaCl, lowers the equilibrium vapour pressure around a water particle [6].

The ions that are the precursors for ion induced nucleation of clusters are present in all parts of the atmosphere. In the troposphere and stratosphere, ionization is due to galactic cosmic rays and radioactive decay and leads to formation of positive and negative molecular oxygen ions [4]. Pure protonated water clusters dominate the stratospheric positive ion composition above 35 km in height; below this, protonated

hydrated and non-hydrated clusters with acetonitrile are found [4]. Section 2.2.7 will deal with cluster ions in the ionosphere.

2.2.6 Growth of clusters into particles

The clusters/nano-CN, can grow into particles in several ways. Clusters formed by homogeneous nucleation can continue to grow by condensation of the same species that formed the cluster. This is a complete homogeneous nucleation from gaseous species to particles as discussed in the previous section. With a charge present in the cluster, ion-induced heterogeneous nucleation from gas to particle occurs. Clusters can also grow by undergoing self-coagulation: the clusters combine to form larger particles by electrostatic attraction or van der Waals attractions or simply by Brownian diffusion.

In the tropospheric boundary layer, charged and neutral clusters are always present [20]. However, the formation of larger particles (≥ 3nm) from clusters is usually observed in bursts, known as nucleation events. This two step process of particle formation can be described as an activation of the clusters: the formed nanoclusters constitute a reservoir, until they are activated and start to grow [18]. While the homogeneous and heterogeneous mechanisms do not require vapours other than the ones that participated in the nucleation of the cluster, cluster activation is accomplished by other compounds. If the compounds are insoluble in the cluster itself, they can still condense on the cluster surface resulting in growth, *i.e.* the cluster acts as a centre for heterogeneous nucleation of these other compounds. However, there is a competition between condensation of vapour on the cluster and condensation on already existing aerosol surface. If the vapours are soluble in the cluster, growth is accomplished by dissolving the gas phase vapours in the condensed phase. The efficiency of this process depends on the solubility and the vapour pressure of the compound [18]. Secondary organic aerosol formation has been suggested to include multi-phase chemical reactions, where vapours condensed on the cluster or dissolved in it are transformed to products with lower vapour pressures by chemical reactions such as oxidation or oligomerization [18].

Both charged and neutral clusters are found in the atmosphere at all times. A recent review [21] of observations gave the concentration of small air ions—*i.e.* charged molecules and clusters—to 200–500 cm^{-3} per polarity. Although charged clusters are much more stable than neutral ones the abundance of neutral clusters is thought to be 10–100 times larger. Consequently, ionic cluster formation has been estimated to result in no more than 10% of the total particle formation rate in the lower troposphere [18]; recombination of ionic clusters may also account for ≈10% of the neutral clusters [20]. Recent experimental results indicate that ionization by galactic cosmic rays may increase the binary (H_2SO_4/H_2O) and ternary ($H_2SO_4/H_2O/NH_3$) nucleation rates of 1.7 nm particles in the tropospheric boundary layer by 2–10 times [19]. Typical growth rates of nanometre sized particles are 1–20 nmh^{-1}; it can be lower if the air is clean and higher in polluted areas. Growth rates are also higher during the summer compared to the winter. The formation rate of 3 nm particles during a boundary layer nucleation event is approximately between 10^{-2}–10^{1} particles $cm^{-3}s^{-1}$; however, it can be several orders of magnitude higher [22].

2.2.7 Protonated clusters in the ionosphere

The discussed formation mechanisms for clusters are those that are considered most important for formation of atmospheric particle precursors. It is implied that they occur in the lower atmosphere, where the majority of secondary aerosol formation takes place. However, cluster ions are also found much higher up in the ionosphere.

Aqueous cluster ions are found in the D-region of the ionosphere, which extends between 60 and 90 km above the surface. During day-time, X-rays and extreme ultraviolet radiation from the sun produce O_2^+ and N_2^+ ions from the air molecules, accompanied by the formation of free electrons. NO^+ ions are formed from NO by ultraviolet radiation from hydrogen atoms in the sun (Lyman-α radiation, 121.6 nm). The N_2^+ ions react with molecular oxygen to form O_2^+; the main positive radiation products are therefore O_2^+ and NO^+ with the latter ion normally dominating [4]. At night, galactic cosmic rays also lead to some degree of O_2 and N_2 ionization. Formation of protonated water clusters begin with the ions O_2^+ and NO^+ undergoing a series of reactions with the final steps $O_2^+(H_2O)_2 + H_2O \rightarrow H^+(H_2O)_2 + O_2 + OH$ and $NO^+(H_2O)_2 + H_2O \rightarrow H^+(H_2O)_2 + HNO_2$ [4, 23]. The protonated water dimer then grows by the addition of other water molecules. The binding energy released upon addition of H_2O to the clusters is dissipated through interactions with the surrounding gas; hence, the growth process is pressure dependent. The abundance of protonated water clusters, $H^+(H_2O)_n$, in the D-region ranges from 10^3 to 10^4 cm^{-3} (sizes n = 2–8, sometimes higher) [4]. There is a sharp decrease in abundance above roughly 82–85 km in height [4], that can be attributed to dissociative recombination of protonated water clusters with free electrons [24-26]. There is a corresponding increase in the abundance of free electrons above this height, *i.e.* the concentration of cationic water clusters is small when the concentration of electrons is large and *vice versa*.

2.2.8 Pyridine-containing clusters in the atmosphere

Ammonia and sulphuric acid/bisulphate are prime candidates for involvement in atmospheric nucleation processes, their role and nature have been investigated intensively (*e.g.* [19, 27-30]); however, pyridine has not enjoyed the same level of attention in this context.

Early measurements of tropospheric ion composition by Perkins and Eisele indicated unknown ions that were later identified as pyridinium, picolinium and lutidinium (among others) [31, 32]. Pyridinium often dominates the tropospheric positive ion spectra [33], although strong local and temporal variations in concentration are observed. Figure 3 shows the structure of pyridinium, picolinium and lutidinium. Beig and Brasseur [34] included these compounds in kinetic modelling work on positive and negative cluster ions in the atmosphere. They found that clusters of the type $H^+(\text{pyridine})_1(NH_3)_m(H_2O)_n$ could dominate the positive ion spectrum between 1 and 6 km above the ground and between 0 and 6 km if charged aerosols are not included. This is a consequence of the high proton affinity of pyridine (930 $kJmol^{-1}$ [35]). At ground level, the number density of these "pyridinated cluster ions" was estimated to ≈ 300 cm^{-3}. Pyridine is also an interesting tropospheric compound in light of the previously mentioned results of Kurtén *et al.* [11], indicating that amines other than ammonia might have a large impact on ternary nucleation processes of both neutral and charged clusters.

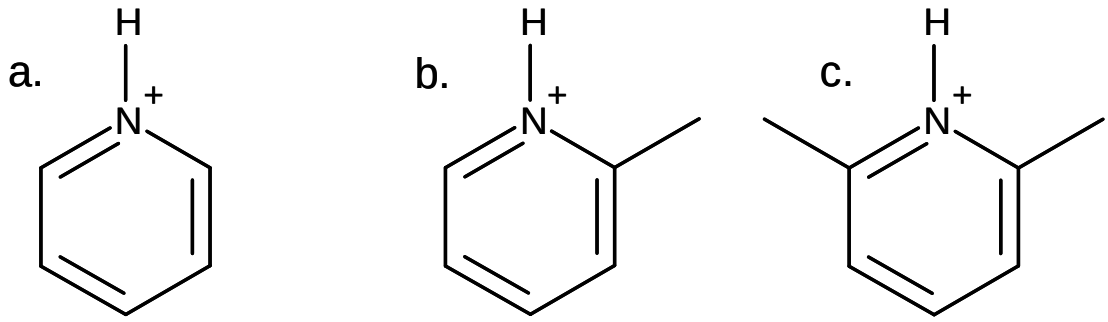

Figure 3. a) Pyridinium, b) α-picolinium and c) 2,6-lutidinium.

Sources of atmospheric pyridine and pyridine derivatives include biomass burning, automobile exhaust, coal tars and tobacco smoke [36-38], while the main atmospheric sinks are likely reactions with OH radicals [32, 39-41]. Yeung and Elrod [41] measured reaction rate coefficients for the reaction of pyridine and some of its derivates with the OH radical. Based on their results they calculated atmospheric lifetimes of 44 days for pyridine and 1 to 10 days for various substituted pyridine compounds. Other suggested atmospheric sinks of significance are reactions with HNO_3 in polluted environments [40] and reactions with atomic chlorine [42].

Using mass spectrometry, Eisele measured approximately 10 ppt of pyridine at Sapelo Island, Georgia, USA [32]. Measurements by Tanner and Eisele [43] on Hawaii indicated roughly 2.5 ppt molecular pyridine. Schulte and Arnold [33] identified pyridinium as the dominant ion in air-plane based measurements in the free troposphere over Europe. More recently, measurements of day-time air ions at an urban site (SMEAR III station, Helsinki, Finland) identified protonated poly(alkyl) pyridines as one of the primary positive compound types [44]. Pyridine ions and alkyl substituted pyridine ions were observed in both day-time and night-time ion spectra—with approximately a factor two higher concentration during night-time—at the remote SMEAR II station in Hyytiälä, Finland [45].

2.3 Cluster ions in the laboratory

Molecular clusters are also of fundamental interest outside of atmospheric contexts. Using clusters as model systems, it is possible to investigate solvation mechanisms of ions and electrons, and to extract information on thermodynamic properties and dynamics. This work is mainly concerned with different types of cluster ions where the main component is water; for example, $H^+(H_2O)_n$, $H^+(NH_3)_1(H_2O)_n$, $H^+(\text{pyridine})_m(H_2O)_n$ or $HSO_4^-(H_2O)_n$. Such clusters are studied in cluster beam experiments, which typically focus on reactions with gas phase molecules under high vacuum conditions.

2.3.1 Experimental considerations

Working with nanometre-sized clusters involves special limitations. While aerosol beams can be produced using aerodynamic-lens systems, and aerosols can be size selected by impactors, the inertia of clusters is simply too small for these approaches to work satisfactorily. The low inertia also means that clusters have large Brownian diffusion compared to the larger aerosol particles, and consequently have a tendency to

suffer diffusion losses to walls and other surfaces in the experimental equipment. A typical instrument employed for the detection of aerosols is the Condensation Nuclei Counter (CNC). In a CNC, a solvent—often butanol—is condensed on the particles to make them grow before being counted by a laser. Most commercial CNC systems have a lower detection limit of around 3 nm due to diffusion losses and insufficient growth by smaller particles. These limitations have practical consequences when it comes to measurements of nanometre-sized particles and there is often a distinction made between particles above and below 3 nm (see for instance [18]). This size may be used as a dividing line between what is to be considered a nanoparticle and what is to be considered a molecular cluster. However, it is important to bear in mind that the limit is simply the smallest particle that can be detected by a traditional CNC instrument. Table 2 shows the mass and equivalent diameter for some pure water clusters. According to the table, a 3 nm particle corresponds to about 500 water molecules.

Table 2. Neutral water clusters, $(H_2O)_n$. Mass in kilograms and corresponding equivalent diameter (assuming a sphere of 1.0 g/cm³).

n	Mass (kg)	Equivalent diameter (nm)
1	3.0×10^{-26}	0.4*
10	3.0×10^{-25}	0.8
100	3.0×10^{-24}	1.8
500	1.5×10^{-23}	3.1
1000	3.0×10^{-23}	3.9
10000	3.0×10^{-22}	8.3
100000	3.0×10^{-21}	17.9

** For comparison, the O–H bond length is 0.96 Å [46].*

There are many ways to transport, store, and detect ionic species with masses ranging from a few atomic mass units (u) up to several thousand. Thus, if it is possible to work with charged clusters, many of the problems associated with smaller particles will disappear. However, many of the techniques used to study ions require high vacuum environments. Working with clusters in vacuum is generally an attractive prospect: transport is easier, there are less side reactions with background gas, and excitation of cluster energies can give some valuable insights when the cluster cannot shed its excess energy to the surroundings. Of course, from the viewpoint of atmospheric relevance it might be desirable to perform experiments at atmospheric pressure. It should also be mentioned that it is by no means impossible to perform experiments on neutral clusters: neutral cluster beams can be produced [47-50]; and size selection can be accomplished, for instance, by scattering the clusters with a crossing helium beam [50].

2.3.2 *Cross sections and rate coefficients*

The cross section is a concept that—in the physical and chemical sense of the word—is related to the probability of collision or reaction between two things, in our case between a molecule and a cluster. The term refers to the (hypothetical) surface perpendicular to the path of a photon, molecule or particle that constitutes the target for collision[b]. In most cases, this surface is assumed to be circular. Importantly, cross sections do not necessarily depend upon the size of the colliding entities (for instance clusters and molecules) in any trivial manner. In fact, it is a somewhat abstract property that can depend on also other properties—of both colliding particles. It should also be mentioned that there is a difference between the collision cross section, *i.e.* the probability for collision between two species, and the reaction cross section, *i.e.* the probability for having a reaction between the two; a collision does not necessarily mean that a reaction will occur. The cross section for collision between a cluster and a gas molecule in an experiment can be written as an analogue to the Lambert–Beer law:

$$\sigma = -\ln\left(\frac{I}{I_0}\right)/(cL), \qquad (1)$$

where I/I_0 is the ratio of the cluster abundance exiting and entering a volume, c is the concentration of the gas in the volume, and L is the length of the cluster's path through the volume [51].

The simplest form of cross section between a molecule and a cluster is the geometric cross section, illustrated in Figure 4. A molecule approaches the cluster on a path parallel to an axis passing through the cluster centre. The distance between the axis and the trajectory of the molecule is called the impact parameter, b. The largest impact parameter that results in geometric collision is $b_g = r_{cluster} + r_{molecule}$, and gives a geometric cross section $\sigma_g = \pi\, b_g^2$. If the cluster is large compared with the molecule, the geometric cross section is essentially the same as the physical cross section of the cluster.

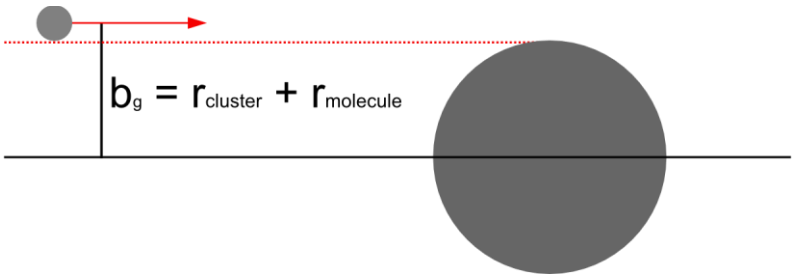

Figure 4. Geometric impact parameter, $\mathbf{b_g}$.

Collision rates between ions and neutral dipole molecules in gas phase are often estimated with Average Dipole Orientation (ADO) theory, developed by Su and Bowers

[b] The unit **barn** (b), originating from the field of nuclear physics can be used to express cross sections and corresponds to 10^{-28} m^2.

[52, 53]. The principle of the ADO cross section is illustrated in Figure 5. An ion with charge q, is situated on an axis, while a neutral dipole molecule approaches the ion with an impact parameter b, as illustrated in the top panel of Figure 5. Dependent upon the electrical potential around the ion, the electrical properties of the dipole (such as polarisability), and the relative velocity v, there is a capture radius r_c around the ion where the dipole will be attracted to the ion and a collision will occur. Thus, the ion and the dipole will collide if $b \leq r_c$ at the point of closest approach, or equivalently if $b \leq b_c$, where b_c is the capture impact parameter. If $b > r_c$ but not too large, the dipole will change its trajectory as seen in the lower panel of Figure 5.

When applied to cluster-ion/dipole reactions, measured reaction rates often exceeded the collision rates predicted by ADO theory. Kummerlöve and Beyer [54] sought to rectify this and presented two new models for molecule–cluster collision cross sections that will be used in this work (Section 4.2.2 and Paper II). The two models both treat the cluster ion and neutral dipole as hard spheres. The charge is still considered a point charge. In the Hard Sphere Average Dipole Orientation model (HSA) the charge is fixed at the cluster centre, while in the Surface Charge Capture model (SCC) the charge is free to move around in the cluster.

The Hard Sphere Average Dipole Orientation model considers two different cases. In the first case, the ADO capture radius of the charge located at the cluster centre is larger than the cluster radius, in this case the capture impact parameter from the ADO theory can be used to calculate the cross section. If the opposite is true, and the cluster is larger than the ADO capture radius at the current relative velocity, the cross section ought to be the geometric cross section. However, the presence of the charge at the cluster centre will enhance the geometric cross section to some degree. Even if $b > b_g$, there is the possibility that the deflection of the dipole trajectory might be enough to bring it in contact with the cluster. The maximum impact parameter where this can happen is the deflection impact parameter b_d. Whichever of b_c and b_d is largest at the current relative velocity determines the HSA cross section.

In the Surface Charge Capture model, the charge is assumed to be drawn to the cluster surface by the interaction with the dipole. This effectively extends the range of the ADO capture radius described above by the radius of the cluster, *i.e.* the impact parameter becomes $b_{SCC} = r_{cluster} + b_C$.

In their work, Kummerlöve and Beyer estimated the cluster radius from the bulk density and estimated the radius of the inbound molecule from its gas viscosity. If one wants to investigate the influence of cluster size on cross section, one can assume $r_{cluster} = r_1 \times n^{1/3}$ where r_1 corresponds to the bulk radius of the monomer comprising the cluster. In such a way, it is possible to derive expressions where the above cross section models are a function of cluster size. Assuming that the inbound dipole is the same monomer the cluster is composed of, the SCC cross section can be expressed as a power law of the form $\sigma_{SCC} = \pi r_1^2 n^{2/3} + 2\pi r_1 b_c n^{1/3} + \pi b_c^2$. The geometric cross section can be expressed as $\sigma_{geo} = \pi r_1^2 \times (n^{2/3} + 2n^{1/3} + 1)$.

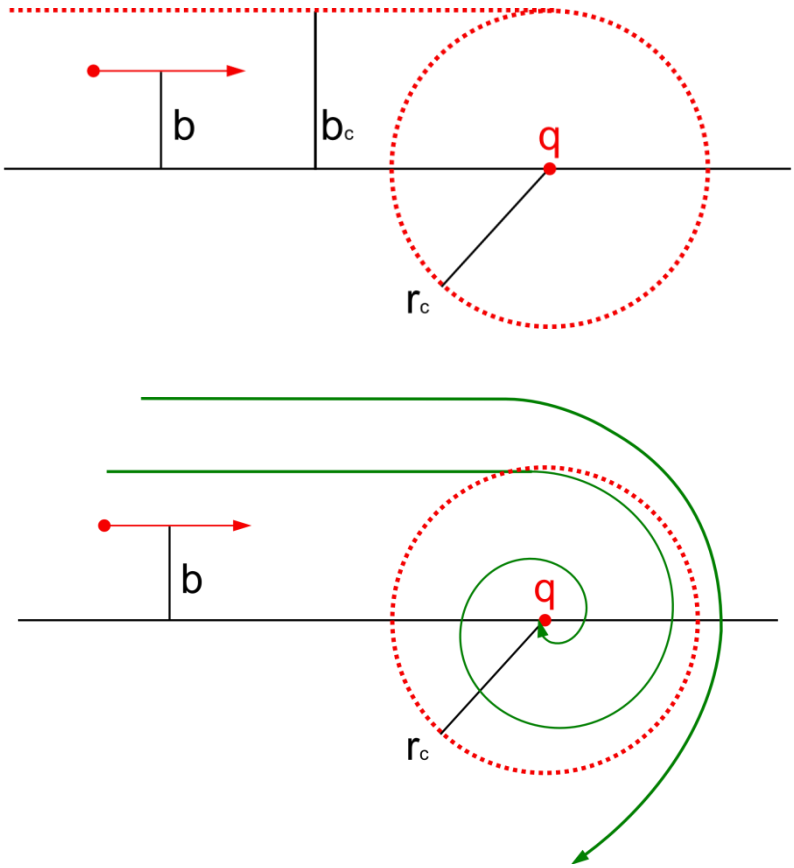

Figure 5. Top panel: Illustration of the ADO capture radius $\mathbf{r_c}$ ***around an ion with charge*** $\mathbf{q}$***, and the corresponding capture impact parameter*** $\mathbf{b_c}$***. Lower panel: dipole trajectories when caught and when deflected by the ion.***

When studying the collision/reaction between a cluster and a molecule using the QTOF 2 instrument (described in Section 3.1), it is for the current experimental setup not possible to get an accurate reading on the collision gas pressure. Thus, the concentration c in Equation (1) is unknown. Consequently, it is necessary to express the reaction cross section in relative terms. In an experiment, the cross sections of all cluster types and sizes are expressed relative the cross section of a single cluster. As seen from Equation (1), the relative cross section becomes

$$\sigma_{relative}(n) = \frac{\sigma(n)}{\sigma(r)} = \frac{A(n)}{A(r)}, \qquad (2)$$

where the absorbance $A = -\ln(I/I_0)$, n denotes a cluster size, and r denotes the reference cluster size. Ideally, the reference cluster has a known cross section allowing all other cross sections to be calculated. In order to calculate a relative reaction rate coefficient from the expression $k = \sigma v$, the difference in relative velocity v for different cluster sizes must be accounted for.

Hence, the relative rate coefficient becomes

$$k_{relative}(n) = \frac{A(n)v(n)}{A(r)v(r)}. \quad (3)$$

In the experimental setups used for this work, clusters are given a kinetic energy by the instrument, E_{LAB}, and are collided with gas phase molecules. The energy relevant for the collisions is the centre-of-mass energy, $E_{COM} = E_{LAB} \times m/(m + M)$, where m and M are the masses of the gas molecule and the cluster, respectively. This expression assumes that the gas molecule is stationary (T = 0 K) and is therefore a nominal collision energy. In practise, the thermal motion of the gas molecules leads to a distribution of collision energies with the average collision energy being somewhat higher than the nominal one. The full-width-at-half-maximum (FWHM) of the collision energy distribution is approximately $(11.1 k_B T \times E_{COM} \times M/(m + M))^{1/2}$, corresponding to ≈ 0.17 eV at 298 K, $M/(m + M) \approx 1$ and E_{COM} = 0.1 eV (the latter a typical value in the experiments herein) [51, 55]. The average centre-of-mass collision energy resulting from the distribution is obtained by adding a term $3/2 k_B T \times M/(m + M)$ to the nominal collision energy. Using the above values, the term corresponds to about 0.04 eV, or, the thermal kinetic energy of the gas molecules [51, 55]. The shifts in reduced collision energy and the effect of the energy broadening are deemed to be of little importance for the experimental results in this work, and the nominal collision energy is usually given.

2.3.3 Abundance spectra

An abundance spectrum is a measurement of the different abundances in a cluster distribution. Cluster distributions are produced and measured in different ways using different experimental setups and the distributions can have different properties and meanings. Figure 6 shows an abundance spectrum of pure protonated water clusters, $H^+(H_2O)_n$, produced in the QTOF 2 instrument (Section 3.1). A distribution of water clusters like the one in Figure 6 is formed by successive evaporation of water molecules from larger clusters (Section 3.1.1). The overall shape of the cluster distribution—the width, height and curvature of the mass spectrum—is dependent upon the specific type of cluster source used and its configuration, as well as the detection efficiency and other properties of the instrument. In contrast, the detailed structure in the distribution is dependent upon the properties of the specific clusters themselves and assuming all clusters have undergone at least one decay is usually independent of production conditions. By dividing the spectrum with a fitted polynomial curve, one can remove from the distribution the general features associated with the specific instrument and means of production. Thus, one obtains a detailed structure abundance distribution that is dependent only upon the properties of the clusters [56].

The detailed structure in the abundance spectrum includes the "magic numbers": clusters with a markedly higher abundance than their neighbours. In Figure 6, examples of magic numbers can be seen for n = 21, n = 28 and n = 55. Magic clusters are usually assumed to have higher stability than their neighbours, which would be the reason for their comparably high abundance as their formation is thermodynamically favourable. Furthermore, the stable magic numbers would be less likely to fragment. For metallic clusters, magic numbers are associated with the formation of an energetically favourable close-packed geometrical shape (such as icosahedra) or by electronic shell

closings (see *e.g.* [57, 58]). The situation can be more complicated for non-metallic molecular clusters because the shapes and interactions of molecules are different from metallic atoms. In fact, high abundance of a cluster does not necessarily mean that the cluster is particularly stable, it is possible to have increased abundance as a consequence of decreased dissociation energy of the subsequent cluster, which will then have more of a tendency to evaporate and form the magic number [56].

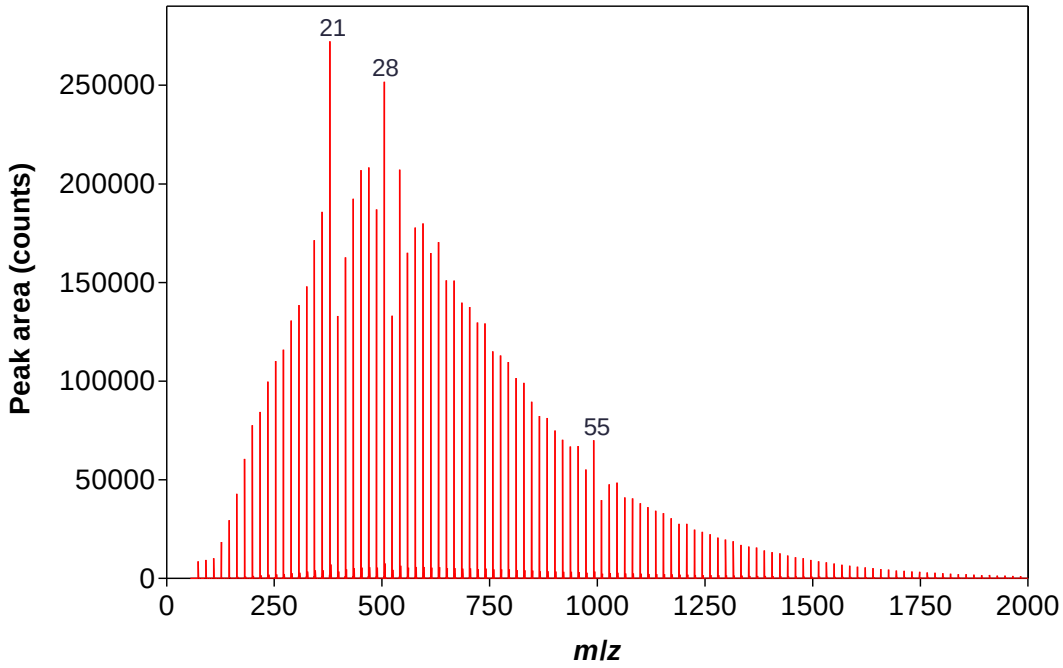

Figure 6. Abundance spectrum for pure water clusters $H^+(H_2O)_n$. Obtained with the QTOF 2 instrument using a kinetic energy of 0.6 eV in the Lab frame. The magic numbers 21, 28, and 55 are marked.

The magic cluster $H^+(H_2O)_{21}$ was first identified by Lin in 1973 [59] and has been the subject of high scientific interest since then. Early on it was suggested that these clusters possess a particularly high stability due to a pentagonal dodecahedral structure [60]. However, the exact nature of the cluster structure is still not conclusively determined. This is also true regarding the question of whether the charge is found in the form of H_3O^+ (Eigen form) or $H_2O–H^+–OH_2$ (Zundel form), and also whether the charge is located at the centre of the cluster or at the surface (*cf.* [61, 62]). Experimental work by Shin *et al.* [63] that probed the $H^+(H_2O)_{21}$ cluster O–H bonds with infrared laser light indicated that all O–H stretches have the same vibrational frequency. This is an indication of a symmetric structure where all water molecules have the same degree of coordination.

Analysis of abundance spectra by Hansen *et al.* [56] indicate that the dissociation energy for water molecules is not particularly high for $H^+(H_2O)_{21}$. On the other hand it is indicated that the $H^+(H_2O)_{22}$ cluster has lower than expected dissociation energy. The magic number $H^+(H_2O)_{21}$ can thus be interpreted as a shell closing of sorts; its high abundance is not due to high stability of the cluster itself, but is a consequence of an increased evaporation of water molecules from the next larger cluster.

2.3.4 Cluster ions reacting with D_2O

Many of the experiments presented in this work focus on protonated aqueous clusters, including some with ammonia, pyridine or bisulphate present, and their reactions with heavy water at comparably low collision energies in the high vacuum environment that is the QTOF 2 instrument.

A few naming conventions will be used in this work to refer to the isotopes of hydrogen in different charge states; these are shown in Table 3.

Table 3. Names of hydrogen atoms and ions. Adapted from Bunnet and Jones [64].

	General	**^{1}H**	**^{2}H**
The atom (H)	Hydrogen	Protium	Deuterium
The cation (H^+)	Hydron	Proton	Deuteron

The reaction between the cluster and heavy water takes place through a short lived reaction intermediate [65, 66]. Addition of the D_2O molecule to the cluster leads to release of binding energy, which makes the intermediate hotter than the cluster reactant. As stabilisation by surrounding gas is absent in the high vacuum environment of the instrument, the reaction complex will decompose by evaporation of a molecule—typically a water molecule—within ~1 μs (Paper I). For a cluster of type $H^+(X)_m(H_2O)_n$, where X is a molecule other than H_2O, the reaction can be written:

$$H^+(X)_m(H_2O)_n + D_2O \rightarrow [H^+(X)_m(H_2O)_n(D_2O)]^* . \quad (4)$$

The formed reaction complex then decomposes, with different products possible:

$$[H^+(X)_m(H_2O)_n(D_2O)]^* \rightarrow H^+(X)_m(H_2O)_n + D_2O \quad (5a)$$

$$[H^+(X)_m(H_2O)_n(D_2O)]^* \rightarrow H^+(X)_m(H_2O)_{n-1}(HDO) + HDO \quad (5b)$$

$$[H^+(X)_m(H_2O)_n(D_2O)]^* \rightarrow H^+(X)_m(H_2O)_{n-1}(D_2O) + H_2O. \quad (5c)$$

The similar dissociation energies of H_2O, HDO and D_2O means that generally only one water molecule will leave during fragmentation of the intermediate and the reaction enthalpy is close to zero (quantum chemical calculations in Paper I give the zero-point reaction energies of Reactions (5b) and (5c) as −0.004 eV and −0.009 eV, respectively). While the first reaction pathway returns the original reactants, the second and third pathways result in product clusters that have exchanged one or two of their protium atoms for deuterium, producing a mass increase in the product clusters of 1 u and 2 u, respectively.

The reaction pathway (5b) requires the formation of HDO molecules inside the cluster intermediate and is a result of an intermolecular H/D exchange mechanism. The H/D exchange process is catalyzed by the presence of a free moving hydron in the

cluster (Paper I–II and [65, 66]), and may progress through a series of quick individual rearrangement steps on a time scale of 50–500 ps [67].

If the lifetime of the intermediate is sufficiently long compared with the time scale of the intermolecular H/D rearrangements then a complete randomization may be achieved with respect to which hydrogen that bonds to which oxygen before a water molecule leaves. This can be referred to as complete hydrogen scrambling. Assuming a completely randomised intermediate, the expected abundances of each product—H_2O, HDO and D_2O—can easily be calculated using combinatorics. Figure 7 shows the probability of forming the three possible products upon decay of such a reaction complex, $H^+(X)_m(D_2O)_1(H_2O)_n$.[c] The calculations assume that there is no isotope bias for evaporation; all water molecules have the same probability of leaving. Honma and Armentrout [65] showed in experiments on the mirror reaction of (4), $D^+(D_2O)_n + H_2O$ for n = 1–4, that there were no indications of a significant isotope effect on the reaction branching ratios.

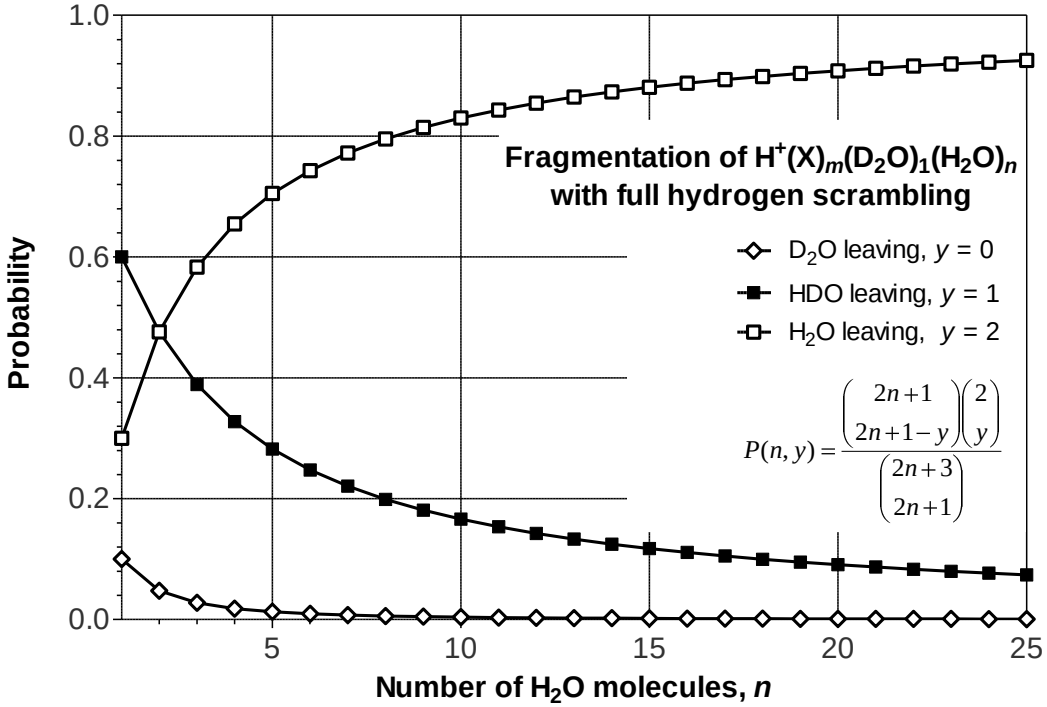

Figure 7. Probability to form one of the molecules D_2O, HDO or H_2O upon decomposition of a reaction intermediate $H^+(X)_m(D_2O)_1(H_2O)_n$ with complete hydrogen scrambling, given as a function of original cluster size (n) and the number of deuterium atoms left in the product (y).

The product of the second exchange reaction (5c) can also be formed in the absence of a free hydron in the cluster. The product is then formed through a ligand exchange mechanism where D_2O enters the cluster and H_2O leaves to form $H^+(X)_m(D_2O)_1(H_2O)_{n-1}$. There are no H/D rearrangements expected in the absence of a free hydron, which

[c] In all calculations it is assumed that the molecule X do not contain any hydrogen atoms that are able to take part in the intermolecular H/D exchange process. That is, the number of hydrogen atoms in the reaction complex is $2n + 3$.

means that the water molecules stay intact in the cluster intermediate. This ligand exchange mechanism can also result in formation of the original cluster (5a). If there is no selection bias regarding which water molecule that leaves the intermediate, the probabilities of forming the $H^+(X)_m(D_2O)_1(H_2O)_{n-1}$ and $H^+(X)_m(H_2O)_n$ products are $n/(n+1)$ and $1/(n+1)$, respectively. The probabilities are shown in Figure 8 below.

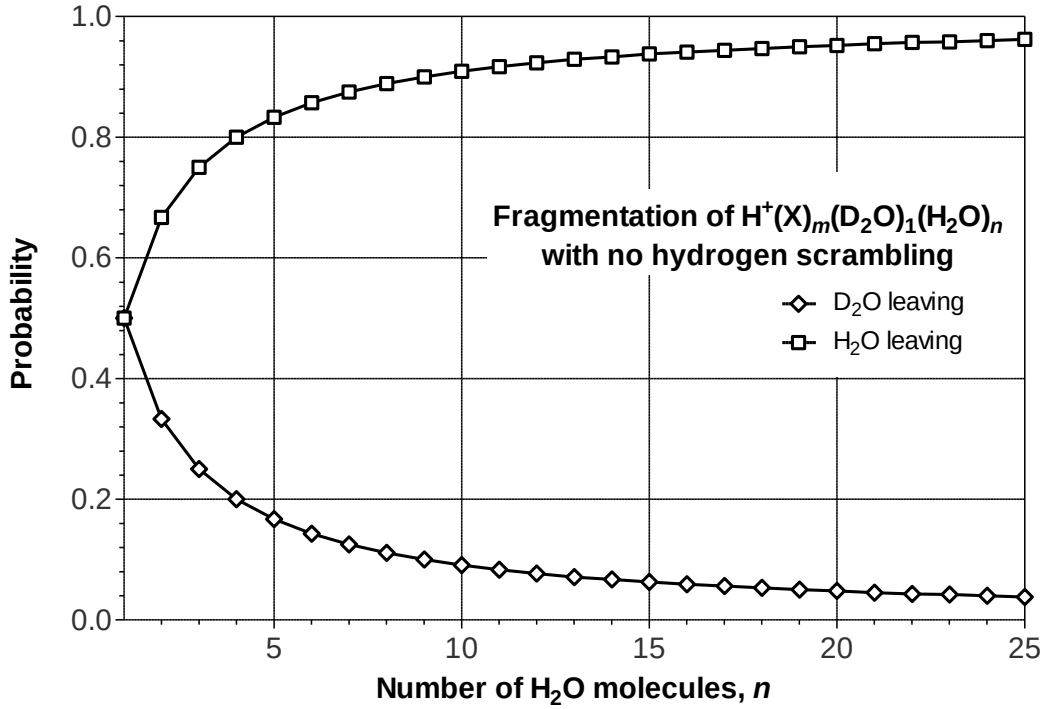

Figure 8. Probability to form one of the molecules D_2O or H_2O upon decomposition of a reaction intermediate $H^+(X)_m(D_2O)_1(H_2O)_n$ with no hydrogen scrambling, given as a function of original cluster size (n).

Reaction (5c) can occur as a result of both the H/D exchange mechanism and the ligand exchange mechanism, while Reaction (5b) is exclusive to the H/D exchange mechanism. Therefore, it is possible to compare the relative abundance of the two products to the values predicted for a completely randomised intermediate (Figure 7) in order to determine which exchange mechanism is at work. This is done by calculating the ratio κ_{HDO} as:

$$\kappa_{HDO} = \frac{I(5b)}{I(5b) + I(5c)} \ , \qquad (6)$$

where $I(5b)$ denotes the abundance of products from Reaction (5b), and $I(5c)$ denotes the abundance of products from Reaction (5c). In an experimental situation where we detect products by the difference in their mass-to-charge ratio relative the reactant cluster, it is convenient to refer to the abundance of a specific product as $I(m/z + x)$, where m/z is the parent ion mass-to-charge ratio, and x is the shift in the products mass-to-charge ratio.

Thus the κ_{HDO} ratio can be expressed as

$$\kappa_{HDO} = \frac{I(m/z+1)}{I(m/z+1) + I(m/z+2)}. \quad (7)$$

A cluster whose reaction intermediate undergoes a complete hydrogen scrambling has a κ_{HDO} value that is equivalent to a value calculated from the statistical abundances in Figure 7. If some fraction of the clusters reacts via ligand exchange, the measured abundance of products from Reaction (5b) would decrease and the measured abundance of products from Reaction 5c would increase. As a result, κ_{HDO} would be less than κ_{HDO} for an H/D randomised cluster. The κ_{HDO} value can vary from 0 for a cluster that reacts solely through ligand exchange, switching a H_2O for a D_2O, to a maximum value corresponding to the κ_{HDO} for emission of a water molecule with random composition. The difference between the experimental and the theoretical κ_{HDO} values can then be used to gain some insight into the hydron mobility in the clusters.

When performing experiments on the reaction $H^+(X)_m(H_2O)_n$ + D_2O, some complicating factors need to be considered. One is possible contamination of the collision gas by HDO. Expected values for κ_{HDO} for different levels of contamination can be seen in Figure 9.

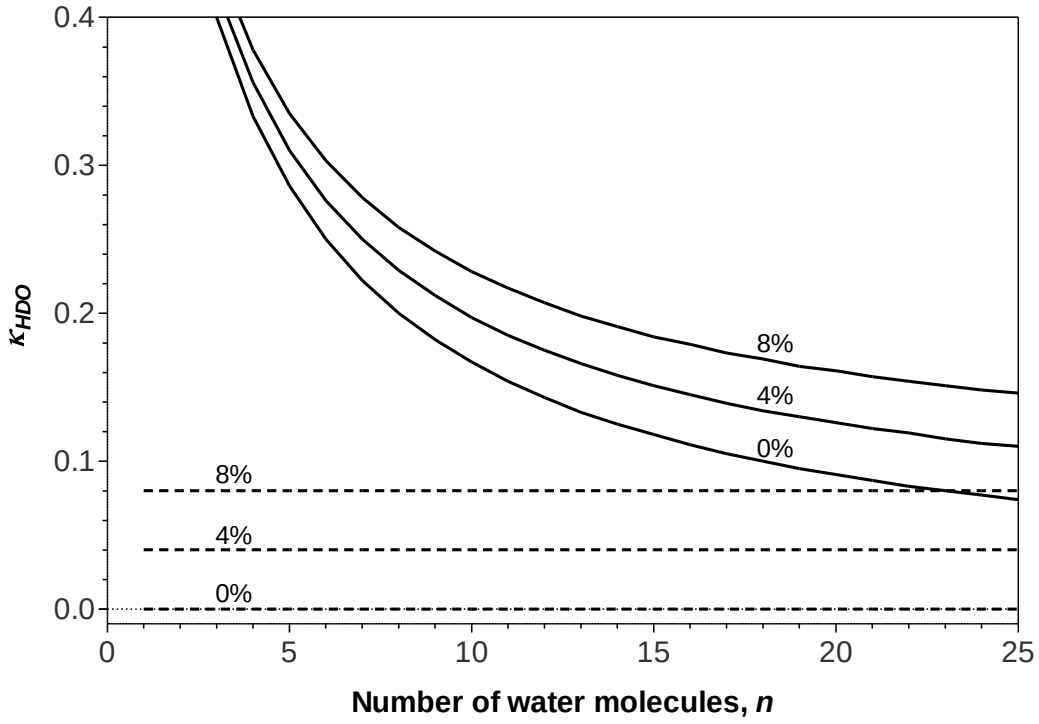

Figure 9. Calculated values of κ_{HDO} for $H^+(X)_m(H_2O)_n$ clusters reacting with D_2O through H/D exchange mechanism (solid lines) and ligand exchange mechanism (dashed lines), at 0%, 4% and 8% HDO contamination of the D_2O collision gas.

For a type of cluster that reacts by the ligand exchange mechanism, $H^+(X)_m(H_2O)_n + D_2O \rightarrow H^+(X)_m(D_2O)_1(H_2O)_{n-1} + H_2O$, the effect of having some HDO contamination in the D_2O gas is simply that some of the products of Reaction (5c) will instead be detected as products of Reaction (5b). Consequently, the κ_{HDO} value will increase from 0 to a value corresponding to the degree of contamination. If 10% of the gas phase D_2O molecules are in fact HDO, then 10% of the abundance $I(m/z + 2)$ will be detected as $I(m/z + 1)$ and $\kappa_{HDO} = 0.1$. This also means that the lowest measured value of κ_{HDO} constitutes a maximum value for the possible HDO contamination. If the cluster is of a type that has complete hydrogen scrambling, then other combinatorics must be employed in order to calculate the consequences.

Another issue that must be addressed for experiments with $H^+(X)_m(H_2O)_n + D_2O$ is the possibility of double collisions. In the experiments it is assumed that only one collision takes place; yet, nothing prevents more collisions with other D_2O molecules. In order to avoid double collisions, the D_2O-pressure is kept at a level where less than 10% of the reactant clusters collide with D_2O; however, this level must be balanced to maintain measurable product intensity. Even if 50% of the clusters experience a second collision, the effect on the κ_{HDO} value is negligible, as seen in Figure 10. This is because the majority of the reactions incorporate two deuterium atoms. For a cluster that has already increased in mass by 1 u or 2 u this leads to masses of +3 u or +4 u relative the parent ion and will not affect the κ_{HDO} value.

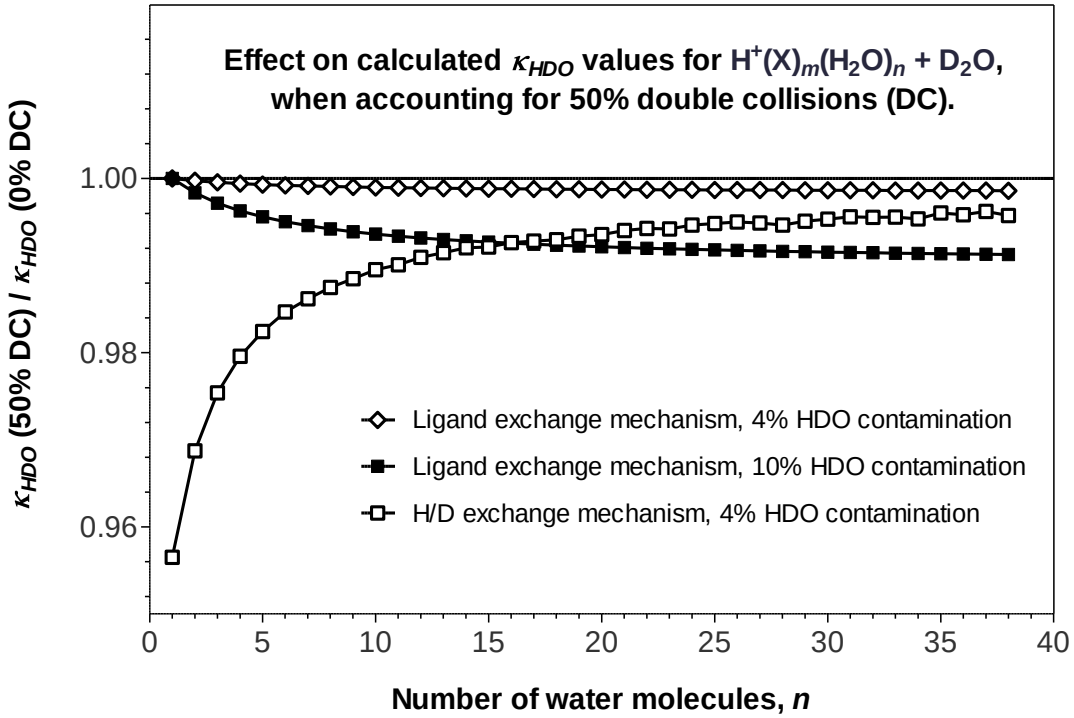

Figure 10. The ratio between κ_{HDO} as calculated for 50% and 0% double collisions. The calculation is done for the reaction where $H^+(X)_1(H_2O)_n$ reacts with D_2O via a ligand exchange mechanism or an H/D exchange mechanism, at different HDO contaminations of the D_2O collision gas.

Four different timescales matter for the reaction between the protonated aqueous clusters and D_2O. The first of these is the timescale for the intermolecular H/D rearrangements inside the intermediate. The second is the lifetime of the intermediate: the time from addition of D_2O until decomposition. The third is the lifetime of the reactant cluster itself, how long the cluster exists without shrinking due to spontaneous evaporation of molecules. Finally, the experimental timescale: the length of time that passes between cluster creation and detection or between cluster size selection and detection.

The relationship between the H/D rearrangement timescale and the intermediate lifetime determines if a complete hydrogen scrambling will be reached before decomposition [65]. This is not always the case, although it is most often desirable that the intermediate achieves full hydrogen scrambling during its lifetime. However, the intermediate's lifetime should be shorter than the experimental time scale, since detection of an intact reaction complex would not yield information on whether the cluster reacts through ligand exchange or H/D exchange (some values are given in Table 4 below). The cluster lifetime should preferably be long compared to the intermediate lifetime and not too much shorter than the experimental time frame; it would be hard to gain any insight from experiments if all clusters disintegrated into molecules. The optimum experiment is one where the cluster lifetime is long enough so that all clusters traverse the instrument and are detected before spontaneously evaporating H_2O. In these experiments, less than 20% of clusters experience evaporation and the consequences thereof can be corrected for as done in Section 4.2.2. Furthermore, the evaporation patterns generally give clear indications of the presence of magic numbers, as is discussed in Section 4.1.2.

Table 4. Experimental time frame and reaction complex lifetime for the reaction $H^+(H_2O)_n + D_2O$, in the QTOF 2 experiments presented in this work. The reaction complex lifetimes were calculated using Rice–Ramsperger–Kassel–Marcus (RRKM) theory (ignoring rotational effects) for 0.1 eV reduced collision energy.

n	**QTOF 2 Experimental time frame (μs)**	**Reaction complex lifetime (μs)**
5	160	0.04
10	173	0.79
15	180	1.26
20	184	1.58
25	188	1.00
	Time from cluster selection to detection.	From RRKM calculations, details in Paper I.

2.3.5 *Cluster ions reacting with NH_3*

While cluster reactions with NH_3 collision gas are similar in many ways to reactions with D_2O, there are some particular issues that need to be considered. For instance, because the dissociation energy of NH_3 is higher than that of H_2O, the reactions typically involve loss of more than one H_2O after addition of NH_3 to the cluster. Furthermore, the absence of deuterium labelling means that we are unable to detect instances of H/D rearrangements in the reaction complexes. The reaction we have studied is:

$$H^+(X)_m(H_2O)_n + NH_3 \rightarrow H^+(NH_3)_1(X)_m(H_2O)_{n-x} + xH_2O. \quad (8)$$

This reaction is assumed to proceed through the formation of a reaction complex by addition of NH_3 to the original cluster. This is followed by loss of one, two or three water molecules. The exact number of water molecules lost depends on the interplay between the dissociation energies of H_2O and NH_3 as well as the collision energy. Reaction enthalpies for clusters containing up to seven water molecules are given in Table 5.

Table 5. Reaction enthalpies in kJmol^{-1} for protonated water clusters' reactions with NH_3.

Reaction	***n =***	**1**	**2**	**3**	**4**	**5**	**6**	**7**
$\mathbf{H^+(H_2O)_n + NH_3 \rightarrow H^+(NH_3)_1(H_2O)_n}$		−248.8	−178.9	−147.1	−120.3	−96.1	−79.8	−64.7
$\mathbf{H^+(NH_3)_1(H_2O)_n \rightarrow H^+(NH_3)_1(H_2O)_{n-1} + H_2O}$		86.2	61.9	51.9	44.4	38.5	38.1	35.1
$\mathbf{H^+(H_2O)_n + NH_3 \rightarrow H^+(NH_3)_1(H_2O)_{n-1} + H_2O}$		−162.6	−117.0	−95.2	−76.0	−57.6	−41.7	−29.5
$\mathbf{H^+(H_2O)_n + NH_3 \rightarrow H^+(NH_3)_1(H_2O)_{n-2} + 2H_2O}$			−30.8	−33.3	−24.1	−13.2	−3.2	8.5

Calculated using data from [35, 68].

When analysing the results of an NH_3-collision-gas experiment it is necessary to deal with side products from pre-reaction evaporation. The cluster lifetime of some 20% of the clusters in the cluster beam is shorter than the experimental timeframe, and spontaneous evaporation of H_2O occur after size selection. This results in a distribution of clusters $H^+(X)_m(H_2O)_n$, $H^+(X)_m(H_2O)_{n-1}$, $H^+(X)_m(H_2O)_{n-2}$, $H^+(X)_m(H_2O)_{n-3}$, … prior to reaction. This distribution of reactant clusters had little significance in the case of D_2O collision gas, as the primary product peaks can only originate from a reaction of the parent ion $H^+(X)_m(H_2O)_n$. In the experiments with NH_3 as collision gas, the reactions of clusters that have lost one or more H_2O prior to reaction overlap with the products of the selected parent ion cluster. In order to determine the extent to which abundance of a product can be attributed to a reaction of the parent ion, a simple "peak attribution" model was devised. Figure 11 shows the outcome of this model for $H^+(\text{pyridine})_1(H_2O)_{17}$ reacting with NH_3.

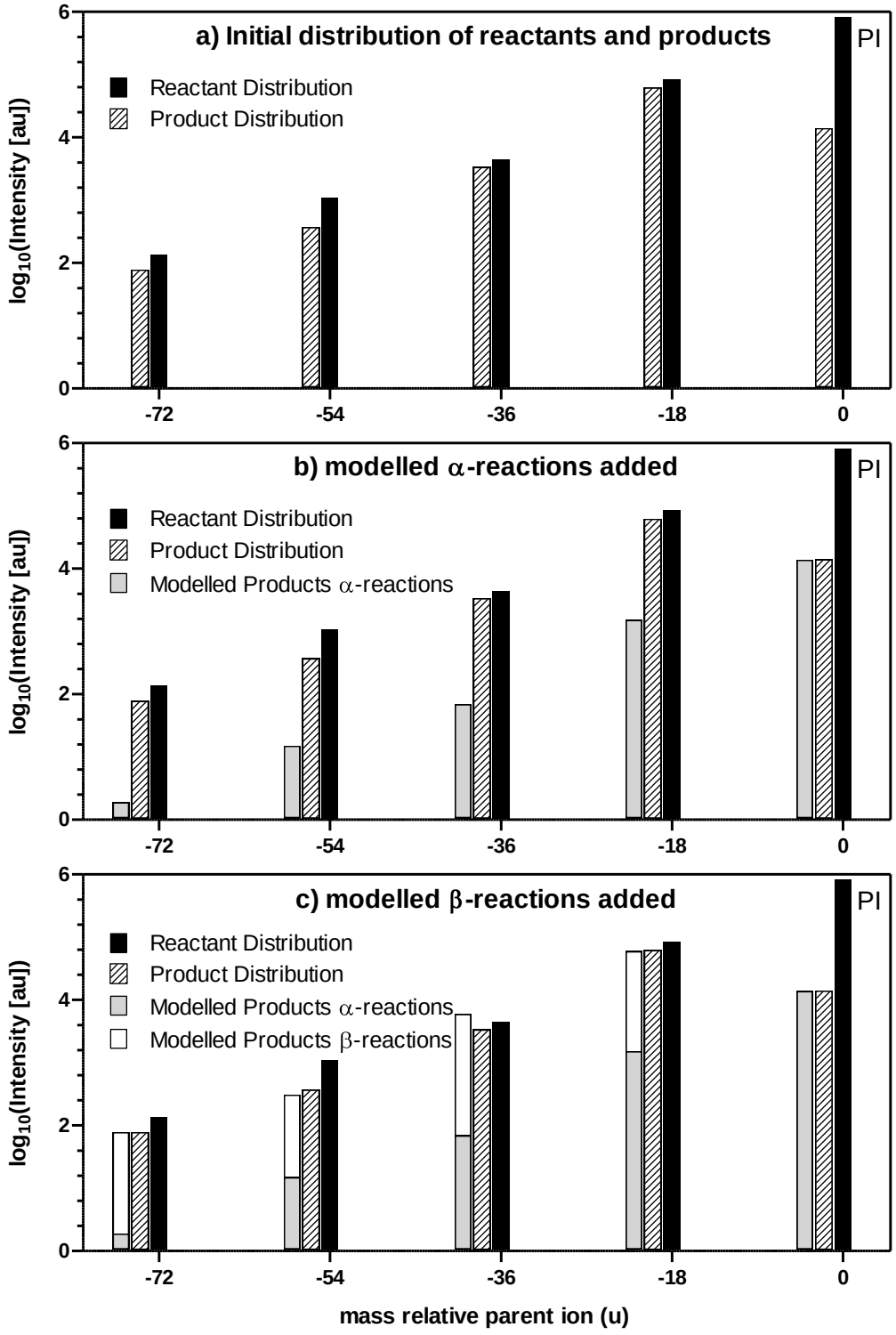

Figure 11. Illustration of the peak attribution model. Details in text.

Figure 11a shows the logarithm of the initial reactant distribution (RD) intensities and product distribution (PD) intensities for a mass spectrometric measurement of $H^+(pyridine)_1(H_2O)_{17} + NH_3$. The peaks are shown as a function of mass relative to the parent ion (RPI); hence the rightmost peak at relative mass 0 is the parent ion, designated by PI. The −1 u peak is the first product peak, representing the parent ion

adding NH_3 and losing H_2O. The peak at −18 u RPI represents the cluster formed by the loss of H_2O from the parent ion prior to reaction. The reactions of the clusters are categorised as α, β or γ reactions, dependent upon whether the cluster after incorporation of NH_3 loses 1 H_2O, 2 H_2O or 3 H_2O, respectively. Consequently, products resulting from α, β and γ reactions will have masses relative the particular reactant that are lower by 1, 19 and 37 u, respectively.

The first product peak in the distribution, at −1 u RPI, can only be formed by an α-reaction of the parent ion:

$$H^+(\text{pyridine})_1(H_2O)_n + NH_3 \rightarrow H^+(NH_3)_1(\text{pyridine})_1(H_2O)_{n-1} + H_2O. \qquad (9)$$

A factor α relating the intensity of this product peak to the parent ion is calculated so that PD(−1 u RPI) = α_n×PI, with the subscript n indicating that the α-value is valid for the reaction of the parent ion cluster (having n water molecules). It is then assumed that the α-reactions of all other reactants in the current measurement can be approximated by the α-factor for a correspondingly sized parent ion—determined in a separate measurement. Thus, the contribution from the second peak in the reactant distribution, found at −18 u RPI, to the second product peak, at −19 u RPI, can be estimated as $MP(-19\text{ u RPI})_\alpha = \alpha_{n-1} \times RD(-18\text{ u RPI})$, where MP = modelled product. Figure 11b shows the distributions of reactants and products, with the modelled contributions from α-reactions added. Note that the modelled product peaks are offset from the measured product peaks on the mass axis for clarity.

Since there is a discrepancy between the modelled abundance of the −19 peak and the measured abundance, it can be concluded that the α-reaction of the −18 peak is not enough to explain the experimentally measured abundance. The missing intensity can only be attributed to a parent ion β-reaction:

$$H^+(\text{pyridine})_1(H_2O)_n + NH_3 \rightarrow H^+(NH_3)_1(\text{pyridine})_1(H_2O)_{n-2} + 2H_2O. \qquad (10)$$

A factor β is calculated to represent the fraction of parent ion clusters that lose $2H_2O$ after reacting with NH_3, *i.e.* $PI \times \beta_n = PD(-19\text{ u RPI}) - MP(-19\text{ u RPI})_\alpha$. We again assume that we can use factors calculated for correspondingly sized parent ions and apply them to the reactant clusters in the current measurement. The β-contributions of all reactant clusters have been added to the modelled intensity in Figure 11c. As can be seen, the model overestimates the abundance of the product peak at −37 u RPI. It can therefore be concluded that $H^+(NH_3)_1(\text{pyridine})_1(H_2O)_{n-3}$ results from reactions of clusters that have lost one or two H_2O prior to reaction, and not from the parent ion cluster.

3 Experimental equipment and experimental procedure

3.1 Quadrupole time-of-flight instrument QTOF 2 and its components

The instrument used for the experiments in Papers I–V is a modified mass spectrometer, QTOF 2 from Micromass/Waters, Manchester, UK. It consists of four main components: an electrospray ion source, a quadrupole mass filter, a collision chamber with a modified gas inlet, and a time-of-flight (TOF) mass analyzer. A schematic overview of the instrument is shown in Figure 12. Cluster ions are produced at atmospheric pressure by the electrospray source, and enter the instrument; a specific cluster size can be selected by the quadrupole, and transferred to the collision cell, where the clusters react with the collision gas (if present). The resulting products are analyzed by the time-of-flight unit.

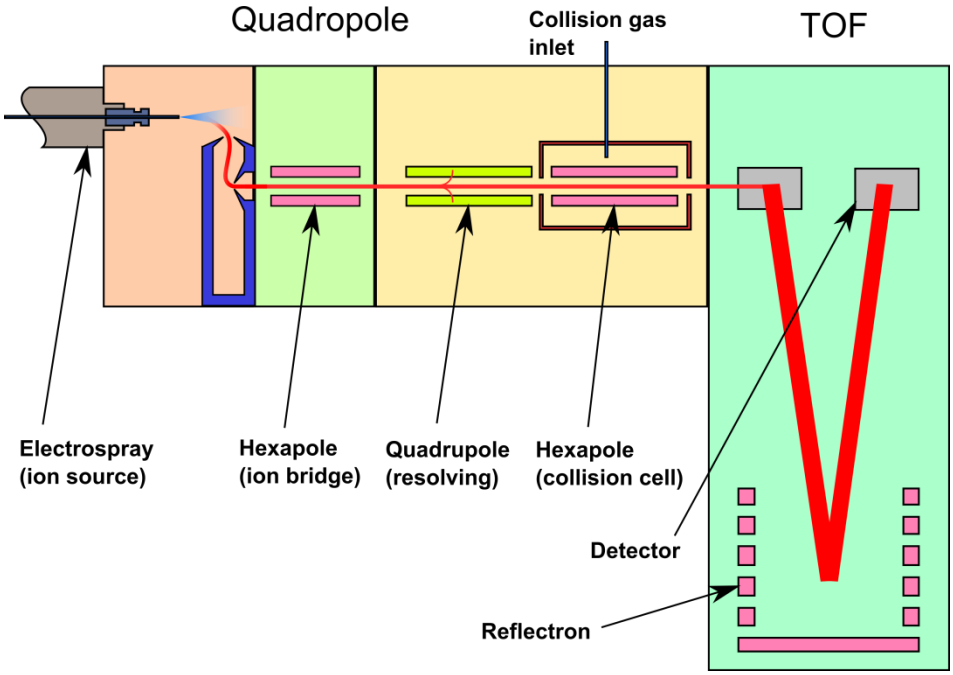

Figure 12. Schematic overview of the QTOF 2 mass spectrometer.

3.1.1 Electrospray ion source

Electrospray ionization has become a very important technique in several areas, and in 2002 John Fenn was awarded with one quarter of the Nobel Prize in Chemistry for his work on developing the technique. Even so, there is no conclusive theory as to the exact nature of the processes behind the final stages of forming ions from a sprayed solution. Electrospray ionization is a soft ionization technique and as such it is particularly suitable for producing ions of macromolecules because it can do so without inducing fragmentation.

A solution containing the molecule one wishes to ionize is pumped through a capillary and into a needle. A common setup used is a syringe in a syringe-pump that

feeds the solution at a typical rate of 5–20 μLmin^{-1}. The needle itself is held at a few kV potential relative an electrode. With a sufficiently high voltage, a Taylor cone is formed at the needle opening as the liquid is deformed by the electric field (Figure 13). The liquid exits the Taylor cone in a fine jet, producing a plume of small, micrometer sized, multiply-charged droplets. A flow of dry nitrogen gas (desolvation gas) is used to evaporate solvent molecules from the droplets. The droplets shrink until they reach the Rayleigh limit where their surfaces become too small to accompany any more charges. At this point the droplets fragment by sending out liquid jets, causing them to lose some mass and a large fraction of their charges [69]. Further evaporation and fragmentation takes place until only singly-charged or multiply-charged ions remain. The electrospray design can also use gas streams other than the desolvation gas, for instance nebulizer gas coming from behind the needle which enables higher flow of solvent. The temperature of the desolvation gas and capillary can be adjusted.

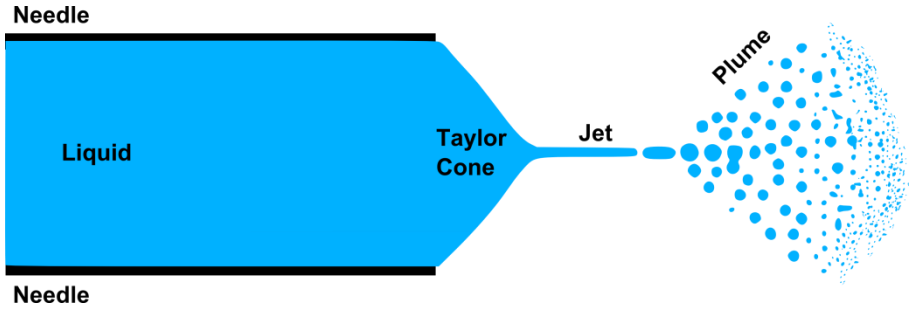

Figure 13. Illustration of an electrospray capillary, Taylor cone, jet, and plume of droplets.

Electrospraying is performed at atmospheric pressure, with only a small portion of the produced spray transferred to lower pressures through a series of small skimmer and capillary openings. For most electrospray setups this is accomplished in two stages. First, the extracted portion of the plume is transferred to a region with pressure of about 100 Pa, with the droplets/ions cooled by the adiabatic expansion of the gas. This is followed by a transfer to a region of high vacuum, where the desolvation of the ions is completed. If the operating conditions of the electrospray are not correctly tuned it is possible for the desolvation of the ions to be incomplete. Rather, a distribution of charged molecular clusters containing both the solvent and the analyte will be produced. This behaviour of the electrospray is taken advantage of in order to produce the clusters studied in this work.

Clogging of capillaries and skimmers can be a problem, especially if the sprayed solution contains inorganic salts. To avoid these problems, the use of different instrument geometries is common. The QTOF 2 used for experiments in this work is fitted with an electrospray having the *z-spray* configuration (exclusive to Micromass). In the *z-spray* configuration, a skimmer is placed orthogonal to the spray plume and extracts the droplets having small mass and high charge using an electric field between the needle and the skimmer. The droplets are transferred from atmospheric pressure to about 1–2 mbar; the rest of the plume hits a detachable baffle positioned directly in front of the electrospray needle. Behind the first skimmer is a second skimmer positioned orthogonal to the first skimmer; again, part of the spray plume is extracted

and finally enters the ion optics in the high vacuum region. The first skimmer is fitted inside a somewhat larger cone with an opening of a few mm. It is possible to have a flow of gas (cone gas) in the narrow space between the skimmer and the cone, exiting the cone counter-current to the path of the droplets. In most of our experiments the cone gas was not used, since it most often caused decreased size of the aqueous clusters.

3.1.2 Linear quadrupole mass filter

Quadrupole mass filters are high vacuum instruments; the one inside the QTOF 2 operates at around 8×10^{-6} mbar. A linear quadrupole is a fairly simple device for performing mass-to-charge ratio (m/z) based selection of ions. It consists of four metallic rods (typically 1–2 cm in diameter and 15–25 cm in length) placed symmetrically around the axis traversed by the ion beam (z-axis) as shown in Figure 14. Opposing pairs of rods have an applied voltage consisting of a DC component (U) and an AC component $V\times\cos(wt)$, where $w/(2\pi)$ is the frequency of oscillation [69].

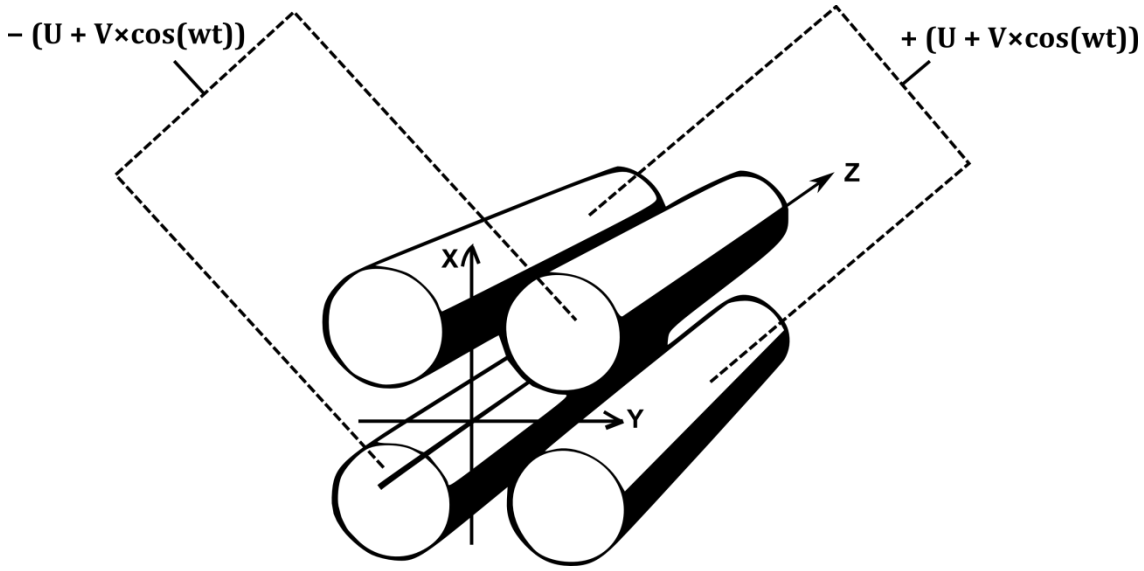

Figure 14. Schematic of a linear quadrupole mass filter.

The applied voltages result in time-varying electric fields in the quadrupole. The path of an ion traversing the quadrupole oscillates around the z-axis; there is a small average force towards the centre where the field is zero. Dependent upon the amplitude of the oscillations and if the motion is stable, the ion will either collide with the rods or exit the quadrupole on the other side. In essence, the quadrupole acts as a mass filter with properties determined by U and V. The magnitude of U and V determines which m/z ratio the ions must have in order to pass the filter. Increasing U and V while maintaining the ratio U/V increases the m/z ratio of the ions passing through [69]. The range of the m/z ratio for which the ions have stable trajectories in both the x- and y-direction is determined by the U/V ratio [69]. By increasing U relative to V a higher resolution is achieved.

The quadrupole can also be used as a high pass filter by completely removing the DC voltage; this is referred to as RF-only mode. However, the transmission is not uniform

over all masses in the resulting high pass window. Instead it decreases as m/z increases far above the cut-off point.

A quadrupole mass filter has several attractive properties: high scan speed, compact design and high throughput of ions (although when used for scanning a m/z range, it has lower throughput than a time-of-flight unit, *cf.* Section 3.1.4). However, in order to maintain a relatively high transmission it is necessary to put some restraints on the resolution. A rod quadrupole is designed to approximate the electric field of four hyperboles and requires high mechanical precision in the shape and positioning of the rods (down to tens of μm) [69]. The inaccuracies in the design and construction lead to severe loss of transmission if the resolution is pushed beyond a certain point. Therefore, a typical quadrupole is operated at a resolution sufficient to separate ions with a unit difference in mass.

3.1.3 Collision cell

The collision cell is a small compartment measuring 16 cm in length situated inside the QTOF 2. The ion beam passes through the collision cell after leaving the quadrupole; a hexapole ion guide inside facilitates the transport of ions through the cell. In the original configuration of the instrument, a tube connected to the cell allows for argon gas to flow into the compartment. By colliding the beam ions with argon at high collision energies, fragmentation of the ions occur and makes it possible to obtain additional information about the constituents and configuration of the ions. For the particular instrument used, the gas inlet is fitted with a T-junction that also connects to an external gas feed, the nature of which is shown in Figure 15.

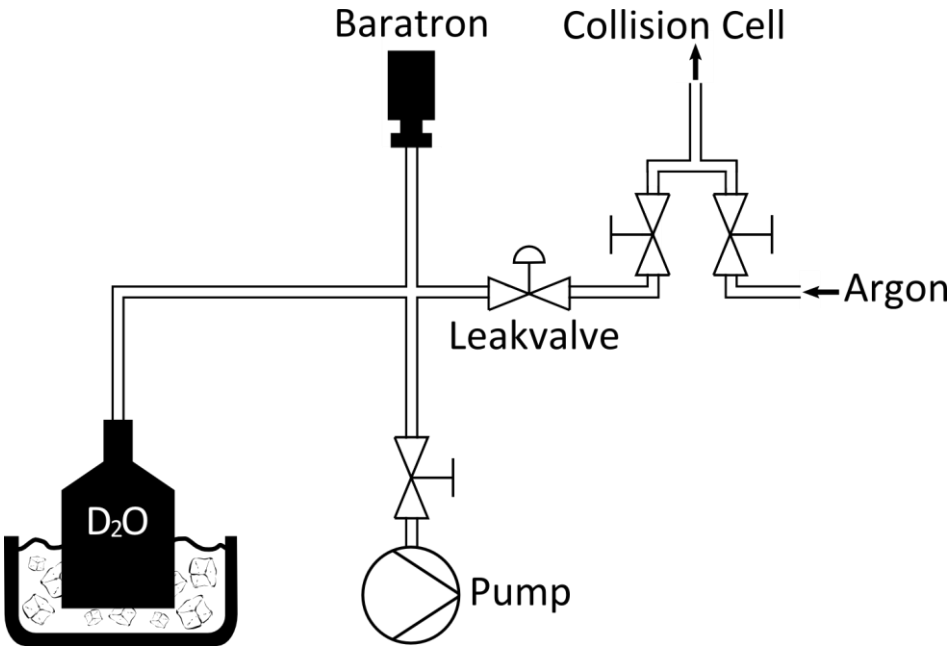

Figure 15. Schematic of the collision gas–inlet system with attached D_2O container.

When using D_2O as collision gas, a stainless steel container of 20 mL containing high grade D_2O is attached to the inlet system. The container hangs in an ice-bath in order to

keep a stable vapour pressure of D_2O above the solid (equilibrium vapour pressure of D_2O (s) at −0.02 °C is 4.79 mbar (3.59 torr) [70]). Stainless steel tubing connects the container to an ultra-high vacuum leak valve that regulates the flow of D_2O into the collision cell. There is also a baratron manometer used to monitor the vapour pressure, and a pump that can be used to empty the feed system of gas. Collision gas pressures up to $\sim 10^{-4}$ mbar can be used without too high loss of beam intensity, although the pressure is usually an order of magnitude lower when interaction of clusters with D_2O is studied.

Water (and other) molecules adsorbs readily on metal surfaces. Consequently, the walls of the collision chamber can contain high amounts of contaminants. These can enter the collision cell as impurities in the collision gas or from the ion source. We estimate the amount of gas phase H_2O that enters the cell when using water in the electrospray to $\sim 10^{-8}$ mbar (compare to the typical collision gas pressure $\approx 10^{-5}$ mbar). Not only can these contaminants react with the clusters if they leave the walls and enter the gas phase, they can also react with the collision gas and form new contaminants. An example of this is formation of HDO from H_2O and D_2O. The presence of contaminants can be reduced by flushing the collision cell with a comparably high flow of pure D_2O vapour for times up to a few days.

For the experiments where NH_3 is used as collision gas, the D_2O container is simply replaced by a gas cylinder containing high purity NH_3.

3.1.4 Orthogonally accelerated time-of-flight mass analyzer

A time-of-flight (TOF) instrument is based on the simple principle of transferring kinetic energy to an ion using an electric field. The energy uptake by the ion in the field is $E = ezU$, where z is the integer number of electron charges e of the ion and U is the voltage of the field. The energy transferred to the ion depends only on the charge and not on the ion mass. The ion accelerates as the potential energy of the ion in the field is converted to kinetic energy. The kinetic energy relates to the ion mass m_i, and after acceleration (*i.e.* upon exiting the electric field) the velocity of the ion is $v = (2ezU/m_i)^{1/2}$ assuming that the ion was initially at rest [69]. Thus, ions can be separated in time according to their mass-to-charge ratio if they move along a certain distance at constant velocity in a field free region. For a flight length l (typically in the range 1–2 meters for TOF instruments) the flight time of the ion becomes: $t = (m_i/z)^{1/2} \times l/(2eU)^{1/2}$ and depends on the square root of the mass-to-charge ratio of the ion [69]. The principle is illustrated in Figure 16. In the QTOF 2 instrument a micro-channel plate detector at the end of the flight path detect the ions. The recorded flight time is converted to a m/z-spectrum. It should be stressed that the flight time depends not only on ion mass, it depends on the number of charges the ion carries as well, with the consequence that heavy ions having multiple charges appear at lower m/z ratios in the spectrum compared to singly charged ions of the same mass.

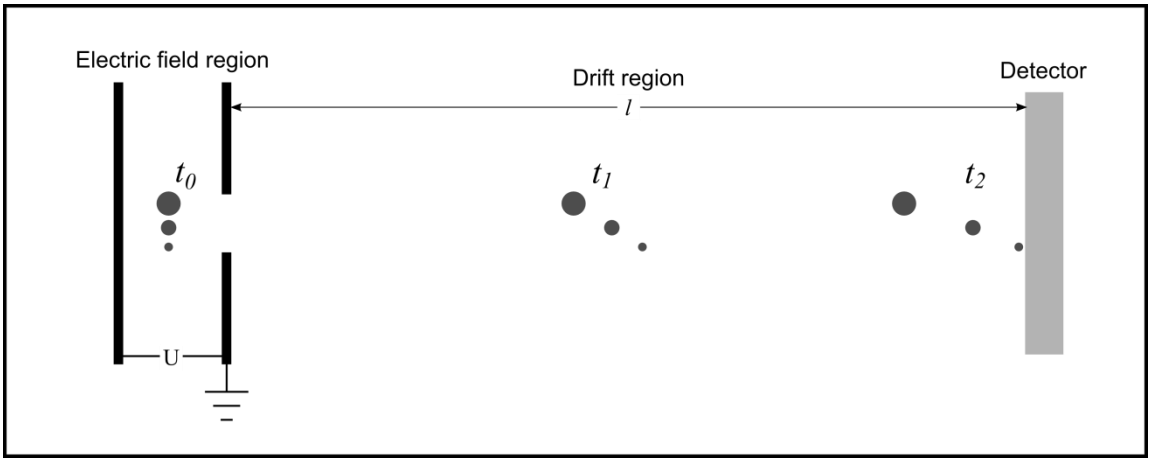

Figure 16. The principle of the time-of-flight instrument. Charged clusters of different mass are accelerated by an electric field* U *and allowed to traverse a field free region of length* l*. This leads to spatial separation with time (*t_0, t_1, t_2**), and different time-of-arrival at the detector.

The TOF unit in the QTOF 2 uses orthogonal acceleration. The continuous ion beam is focused to have as small width as possible, and a section of it is separated by applying a sharp pulsed electric field orthogonally to the beam (in the case of the QTOF 2, 980 V were used). A finite length of the beam is thus pushed into the accelerating region of the TOF unit. The separated beam is accelerated into the drift tube by a voltage of 5–10 kV, which is orthogonal to the original beam path (and parallel to the pulsed field). The QTOF 2 uses 9.1 kV acceleration for positive ions and 7 kV acceleration for negative ions. The ions keep their velocity component in the original direction, meaning that they will fly through the drift tube at an angle relative the original beam.

The ions in the original beam have kinetic, directional and spatial distributions, which lead to a spread in kinetic energy when the ions fly through the drift tube. This results in lower resolution as there will be a spread in flight times for ions of the same m/z. In order to improve the resolution many TOF instruments have a reflectron, which is a series of rings perpendicular to the flight path. In the reflectron, the ion movement is slowed and then reversed by a retarding electric field. Ions with higher kinetic energy have a slightly longer flight path, because they penetrate deeper into the field. Thus, the spread in flight time for ions of the same m/z is reduced [69]. On the orthogonally accelerated TOF units, the detector is placed behind the point of the initial acceleration such that the ion flight path is shaped like a "V" perpendicular to the initial beam. This can be seen in Figure 12 above. This configuration is referred to as single-V mode. Still higher resolution can be achieved by applying several reflectors, resulting in a "W" mode configuration.

Ideally, once the heaviest ion has reached the detector at the end of the drift tube, the ion beam has filled up the cavity of the orthogonal accelerator again and a new pulse can immediately be applied to transfer more ions into the constant field. If the flight time of the heaviest ions is long, some of the ion beam is lost as the orthogonal accelerator waits for the drift tube to empty. This reduces the efficiency by which the instrument uses produced ions for detection. The pulsed field cycle time is thus related to the maximum ion-mass to be detected, with typical values of a few tens or hundreds of microseconds [69]. A spectrum is collected for each cycle; the spectra are combined over a few seconds to improve signal to noise ratio and to reduce the amount of data.

The resolution of the TOF is comparably high, and the possible mass range is very high. The resolution of a TOF unit is given as the ratio $m/\Delta m$, FWHM; m being the ion mass, Δm the width of the peak and FWHM meaning full width at half maximum. Heavier ions are in the TOF unit for longer times; consequently, their variations in flight time will be greater. As a result, peak widths increase with ion mass and the resolution is more or less the same for the entire spectrum. A typical resolution sufficient for most applications is $m/\Delta m$ = 5000 (FWHM); 10000 would be a high resolution [69].

High vacuum is required for operating a TOF unit in order to avoid electrical discharge and adsorption of water and other vapours on the detector, as this could cause degradation. The pressure also influences the probability of ions colliding with background gas molecules. The mean free path for air molecules can be estimated as $\lambda = 66\ \text{nm}/P(\text{in bar})$. Typical TOF operating pressures are around 10^{-7} mbar, giving a mean free path of 660 m for the gas molecules. Collisions between ions and gas molecules would thus be scarce for the ≈ 2 m of the flight tube.

3.1.5 Experimental procedure

This Section describes the experimental procedure used in the experiments employing the QTOF 2 mass spectrometer (Papers I–V). Reagent and solutions are summarised in Table 6 at the end of the section.

For the experiments using D_2O as collision gas, liquid D_2O was added to the stainless steel container on the external gas inlet. Repeated cycles of freezing, pumping and heating were performed on the heavy water in the container in order to extract any dissolved gases. The collision cell and connected tubing from the external gas inlet were conditioned by flushing them with D_2O vapour for 8–15 hours, followed by pumping away excess gas. The conditioning cycle was repeated over a period of 3–5 days, with each cycle consuming a few mL of liquid D_2O. Contamination of the collision gas by HDO was still observed in all experiments.

When using NH_3 collision gas, a gas cylinder containing high purity NH_3 was connected to the gas-inlet system. There were no observations of NH_3 undergoing transformation into deuterated contaminants, NH_2D, NHD_2 or ND_3. Furthermore, the relaxation time after pressure changes was considerably shorter when using NH_3 compared to when using D_2O. The only concern for contaminants was the possible emission of adsorbed molecules from the interior surfaces of the QTOF 2.

For the measurements performed with an empty collision cell, all connections from the gas-inlet system were closed. If performed after an experiment using collision gas, sufficient time was given to allow the collision cell to evacuate.

Cluster ions were produced by the electrospray ion source at atmospheric pressure using various aqueous solutions (Table 6) that were fed to the electrospray from a syringe. Typical solution flow rates were 15–30 $\mu L min^{-1}$. Care was taken to ensure that the syringe and connecting capillary were clean. Conditioning of the capillary by washing it with solvent or solution was required before experiments and when switching solutions.

Because an electrospray is originally designed to remove the solvent from the core ion to produce desolvated charged molecules, some adjustments to the typical operating parameters were necessary to produce a distribution of water-containing clusters. The electrospray was operated with little or no heating of the capillary or desolvation gas.

Furthermore, the different gas flows had to be optimised. The desolvation gas flow was low or nonexistent and the cone gas was turned off. Special attention to the adjustment of the nebulizer gas was necessary, as the amount of produced cluster ions depended strongly on this gas flow.

After production, the ions entered the QTOF 2 interior via two differentially pumped stages. In the quadrupole mass filter, either a broad mass range, for instance 0–2000 u, was allowed to pass through in order to record an abundance spectrum, or a single cluster size was selected to react with the collision gas. In the latter case, up to 38 water molecules were found in the clusters studied. Flight times in the quadrupole are in the range of 130–470 μs for clusters of mass 55–700 u.

After the quadrupole, size selected clusters entered the collision cell and reacted with the collision gas (if present). The pressure of the collision gas was adjusted so that the number of reacting clusters was kept below 10% for the entire mass range studied. A low concentration of collision gas reduces the number of multiple collisions between gas and clusters. This is desirable because our primary interest is in the outcome of single collisions. However, too low a gas pressure reduces the single collision frequency to the point where problems arise in the signal to noise ratio of the mass spectrum product peaks, and statistical uncertainties in measured abundances begin to increase. In addition, the impact of the contaminating HDO desorbing from interior surfaces is greater at low D_2O pressures. Having 5–10% collisions is considered sufficiently low to avoid any significant influence of multiple collisions on experimental results.

The centre-of-mass collision energy (E_{COM}) between the clusters and collision gas was 0.085 eV or 0.1 eV. For the lightest clusters (less than 100 u) the collision energy was adjusted so that the collision energy in the lab-frame (E_{LAB}) was kept at 0.6 eV, as the beam intensity started to decrease below this point. Residence times in the collision cell were between 110 and 160 μs for these energies.

After exiting the collision cell, the reaction products and remaining reactants were accelerated to 16 eV and entered the orthogonally accelerated TOF unit, operating in single-V mode at 2×10^{-7} mbar. Flight times for ions of mass 55–700 u in the TOF are 10–37 μs. The resolution of the TOF unit was $m/\Delta m$ = 5000 (FWHM).

Ion detection in the TOF-unit is done by a pair of microchannel plates in chevron configuration. The sensitivity of the detector was adjusted to ensure that it correctly reproduced a wide range of peak intensities without contributing significant noise to the signal. If the detector in the TOF unit is not sensitive enough, it may take a simultaneous hit from two or more ions to register as a count. This will result in a negative bias for the intensity of smaller peaks. The detector sensitivity was checked using pure sodium chloride clusters produced from a 17 mM aqueous solution. For each $Na^+(NaCl)_m$ or $Cl^-(NaCl)_m$ cluster there was a series of peaks arising from the chlorine isotopes. By comparing the ratio of detected intensities between two peaks to literature values one can estimate detection bias towards smaller or larger peaks. An example is shown in Figure 17.

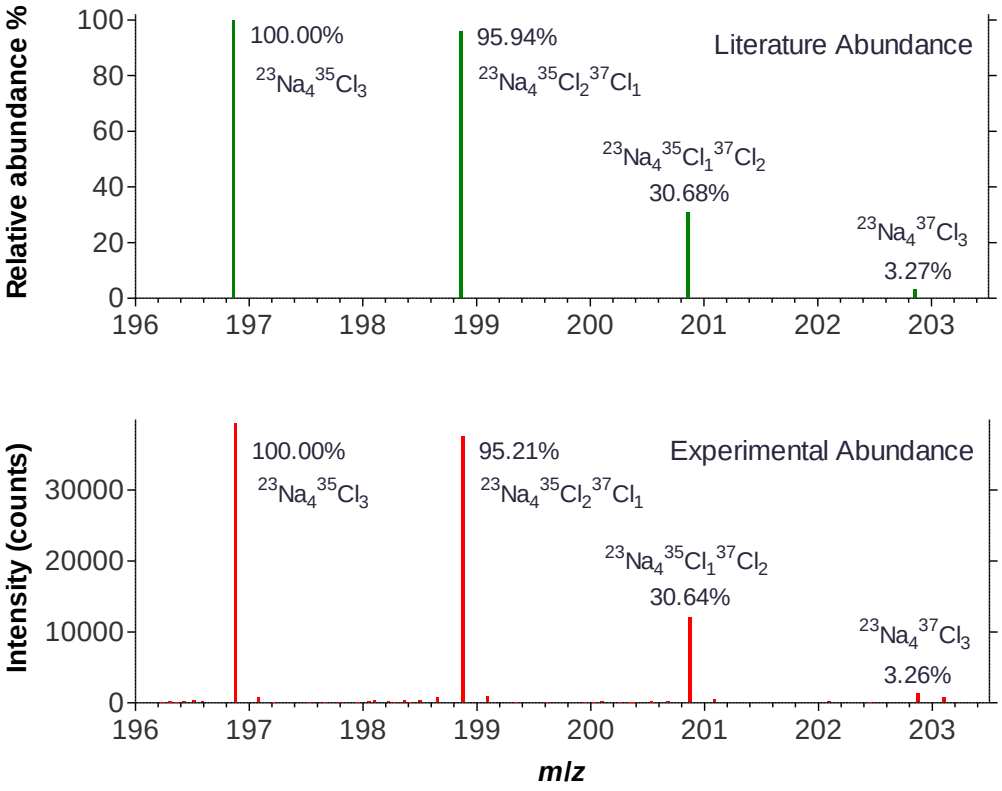

Figure 17. Calibration of QTOF 2 using $Na^+(NaCl)_3$ clusters. Comparison of isotope distribution abundances: as obtained experimentally, shown in the lower panel (integrated peaks); and literature values, given in the top panel.

After an ion has impacted on the detector, there is a relaxation time in the detector system during which no other ions can be detected. Although this time is small (5 ns) it can reduce the measured intensity of larger peaks if only one of several ions arriving simultaneously is detected. The software that operates with the QTOF 2 (*Masslynx v 4.0*) can compensate for this to some degree (referred to as dead-time correction, DTC). Nevertheless, it is prudent to limit the number of ions in the beam, by adjusting the electrospray settings. For these experiments the intensities were limited so that the maximum spectral peak had no more than 300 counts per second.

During the experiments, reference measurements were performed at regular intervals. Analysis of the reference ion spectra can be used to compensate for varying collision gas pressure in the cell, which tends to decay asymptotically with time. Pressure correction was necessary for some of the experiments using D_2O as collision gas; however, it was not necessary for the NH_3 collision gas experiments.

The sampling time for each cluster was usually 2 min and longer if the ion intensity in the beam was low. When using collision gas, separate background measurements with an empty collision cell were performed for each cluster. Abundance spectra were obtained with the collision cell empty.

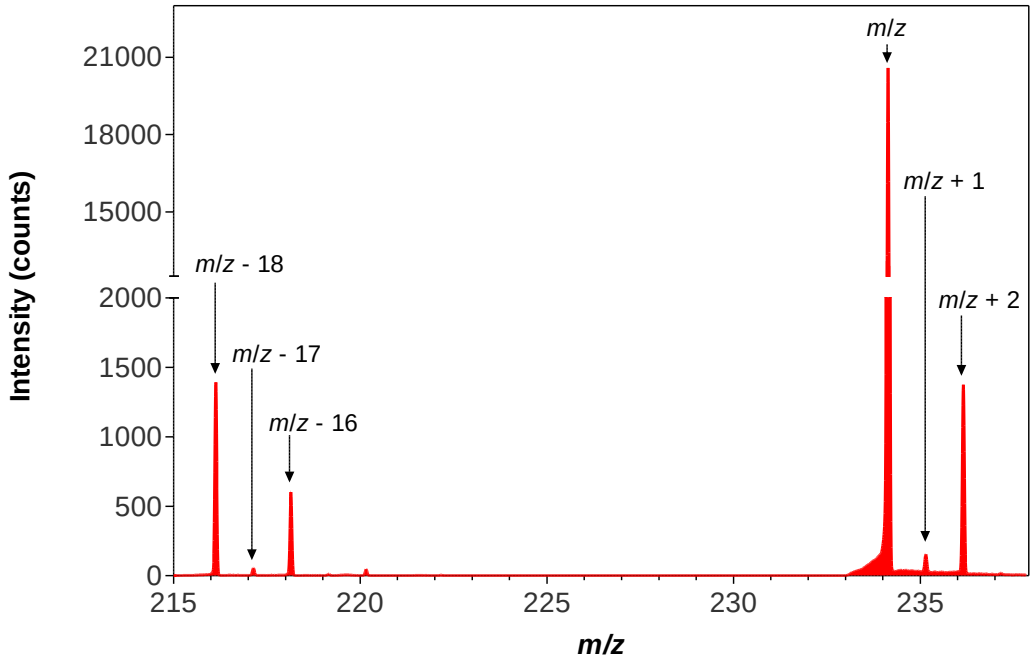

Figure 18. Recorded spectrum for the reaction $H^+(NH_3)_1(H_2O)_{12} + D_2O$. Peaks are indicated by their mass relative the parent ion mass-to-charge ratio m/z. Observe that there is a break on the ordinate and two different scales.

A typical mass spectrum as obtained in these experiments is seen in Figure 18. It shows the product peaks resulting from the reaction $H^+(NH_3)_1(H_2O)_{12} + D_2O$. As indicated in the figure, the majority of clusters that enter the collision cell do not react as the mass spectrum is clearly dominated by the parent ion (designated m/z). The $m/z + 1$ peak is quite small, indicating that $H^+(NH_3)_1(H_2O)_n$ clusters react mainly by ligand exchange reactions. The $m/z - 18$ peak represents evaporation from reactant clusters, while the $m/z - 17$ and $m/z - 16$ peaks arises from post-reaction evaporation of H_2O product clusters (Section 4.2.1).

Table 6. Aqueous solutions and reagents used in the QTOF 2 experiments

Solution	Paper	Produced clusters	Reagents
H_2O	I	$H^+(H_2O)_n$	H_2O, no. 95270 for HPLC, Fluka
15 mM NH_3	I	$H^+(NH_3)_1(H_2O)_n$, $H^+(H_2O)_n$	H_2O, no. 95270 for HPLC, Fluka; 25% NH3 (aq), Pro analysi, Merck
2.5 mM pyridine	II, IV, V	$H^+(pyridine)_{0-2}(H_2O)_n$, $H^+(H_2O)_n$	H_2O, no. 95270 for HPLC, Fluka; pyridine, 99.5%, BDH Chemicals Ltd.
100 mM pyridine	II	$H^+(pyridine)_3(H_2O)_n$	H_2O, no. 95270 for HPLC, Fluka; pyridine, 99.5%, BDH Chemicals Ltd.
15 mM $NaHSO_4$ + 15mM crown ether	III	$HSO_4^-(H_2O)_n$, also $OH^-(H_2O)_n$, $O_2^-(H_2O)_n$, $SO_4^{2-}(H_2O)_n$	H_2O, no. 95270 for HPLC, Fluka; $NaHSO_4$, 99%, Sigma-Aldrich; 15-crown-5-ether, 98%, Aldrich
17mM NaCl	I –V	$Na^+(NaCl)_n$, $Cl^-(NaCl)_n$	NaCl: 99.5%, Prolabo
2.5 mM pyridine + 30 mM NH_3	IV, V	$H^+(NH_3)_1(pyridine)_1(H_2O)_n$	H_2O, no. 95270 for HPLC, Fluka; pyridine, 99.5%, BDH Chemicals Ltd.; 25% NH3 (aq), Pro analysi, Merck
D_2O collision gas	I–III		D_2O, 99.9% D-purity, Sigma-Aldrich
NH_3 collision gas	IV, V		NH_3, 99.96%, Aga

3.1.6 Data treatment and calculations

The raw data from the experiments with size selected cluster ions was first analyzed by use of the program *Masslynx* with corrections made for the detector dead-time. However, because the ion intensities had been limited (Section 3.1.5) the corrections were minor and thus only affected the parent ion peak. Data files from *Masslynx* were converted to *netCDF* format, and processed using a *Matlab* script designed to calculate the total ion count for specified spectral peaks. Peak intensities were normalised for comparison by dividing each peak area by the total ion intensity, which was taken to be the sum of the major spectral peaks. Reference measurements were analyzed and corrections made to compensate for the slow variation in collision gas pressure when this was considered non-negligible. Finally, for each peak the corresponding normalised intensity in the background measurement was deducted. Measured abundance spectra were analyzed in *Masslynx* by combining the peak intensities of all scans, and correcting for dead-time intensity loss.

As mentioned previously, it is convenient to refer to the abundance of a product cluster as $I(m/z + x)$, where m/z is taken to mean the mass-to-charge ratio of the reactant cluster ion and x is the relative shift in mass-to-charge ratio of the product cluster. Henceforth, I will denote a normalised, background corrected intensity.

3.2 Double sector mass spectrometer Separator 1 and its components

The separator 1 instrument is a home-built double sector mass spectrometer, having a BE geometry, meaning it have both a magnetic sector and an electrostatic sector, in that order. A schematic representation can be seen in Figure 19. As shown, the instrument consists of an ion source, working by electrospray ionization (ESI) or corona discharge; a sector magnet; a collision cell; and a hemispherical electrostatic analyser, fitted with a channeltron detector.

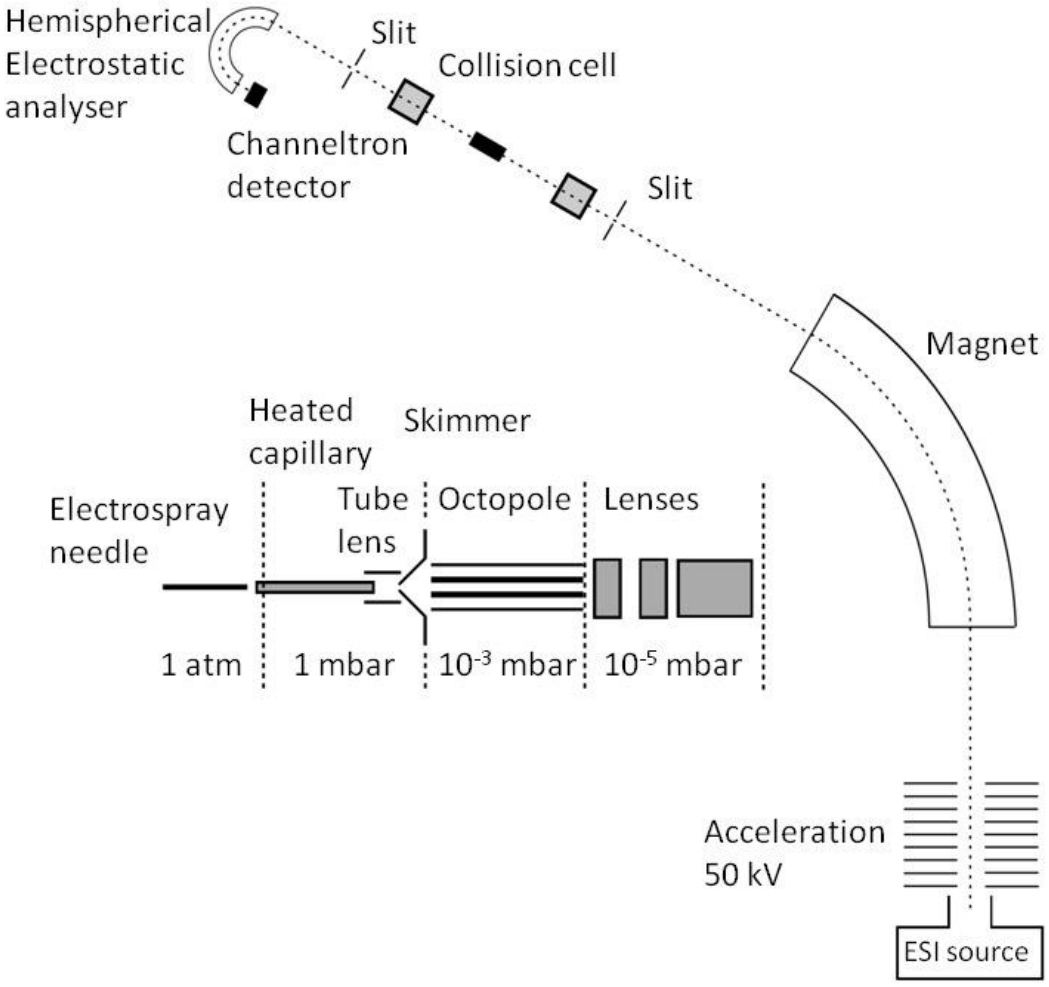

Figure 19. Schematic overview of the Separator 1 instrument. The inset shows details of the ion source.

3.2.1 Cluster ion production by corona discharge

The Separator 1 instrument is fitted with equipment for electrospray ionisation. However, for the experiments in this work (Paper VI), the electrospray needle was replaced with a needle from a scanning-tunnelling-microscope (STM). This allowed for ionisation by corona discharge. Corona discharge for mass spectrometry works by applying a high voltage (a few kV) between two electrodes in a neutral fluid, and is often used with air at atmospheric pressure. One electrode is sharply pointed, while the other is flat. The geometry of the needle enables a very strong local electric field around the point; the air near the needle-point becomes ionised by the field and forms a plasma. When generating positive ions, the needle is the anode and the flat electrode is the cathode. Air molecules separate into positive ions and electrons inside the plasma and the electrons are accelerated towards the needle. The molecular cations wander towards the cathode in an ion current. Note that the plasma should not extend all the way between the electrodes, as this would result in arcing. During the journey to the cathode, the produced ions may experience charge exchange with other molecules or condensation of molecules, especially dipoles. The latter leads to formation of molecular clusters, *cf.* the ADO, HSA and SCC models for charge/charged cluster interactions with dipoles in Section 2.3.2.

3.2.2 Sector magnet

The magnetic sector works by generating a constant magnetic field ($\boldsymbol{B}$) through which the ions travel. The ions will experience a Lorentz force ($\boldsymbol{F_L}$) that is orthogonal to both the magnetic field and the path the ions travel, as illustrated in Figure 20 (note that the direction of the ion current is defined to be the direction in which positive ions move). The magnitude of the Lorentz force experienced by the ion is $F_L = qvB$, provided that the ion velocity $\boldsymbol{v}$ is orthogonal to the magnetic field, $\boldsymbol{B}$ [69]; q is the charge of the ion. Since the Lorentz force is perpendicular to the direction the ion travel, the ion flight-path curves with a radius r which can be found by equating F_L with the centripetal force: $F_c = mv^2/r$. We see now that for a given magnetic field strength and ion speed, there will be a certain mass-to-charge ratio that makes the ion flight path and sector magnet match, and allows the ion to exit on the other side. Thus we have: $m/q = rB/v$. If the ions are accelerated using a constant electric field of voltage U prior to the sector magnet, their kinetic energy will be $E_k = qU = mv^2/2$. Hence, the mass-to-charge ratio of the ion that can pass through the sector can be expressed in terms of the accelerating electric field, the sector radius and magnetic field: $m/q = (rB)^2/(2\mathrm{U})$ [69]. Expressed in terms of mass spectra units divided by the number of elementary charges this becomes $m/z = 10^3 N_A \times e(rB)^2/(2\mathrm{U})$, where N_A is the Avogadro constant and e is the elementary charge.

The resolution of a magnetic sector is typically in the range $m/\Delta m = 2000–7000$ based on peak width at 10% peak height [69]. This corresponds to a resolution of about 3600–12600 FWHM. The mass range of the sector magnets are limited by the maximum magnetic field that can be used, in this case the maximum practical field is 1.2 T. Taken together with the radius of curvature $r = 2$ m and acceleration voltage $U = 50$ kV, this gives Separator 1 a maximum ion mass-to-charge ratio $m/z = 5500$.

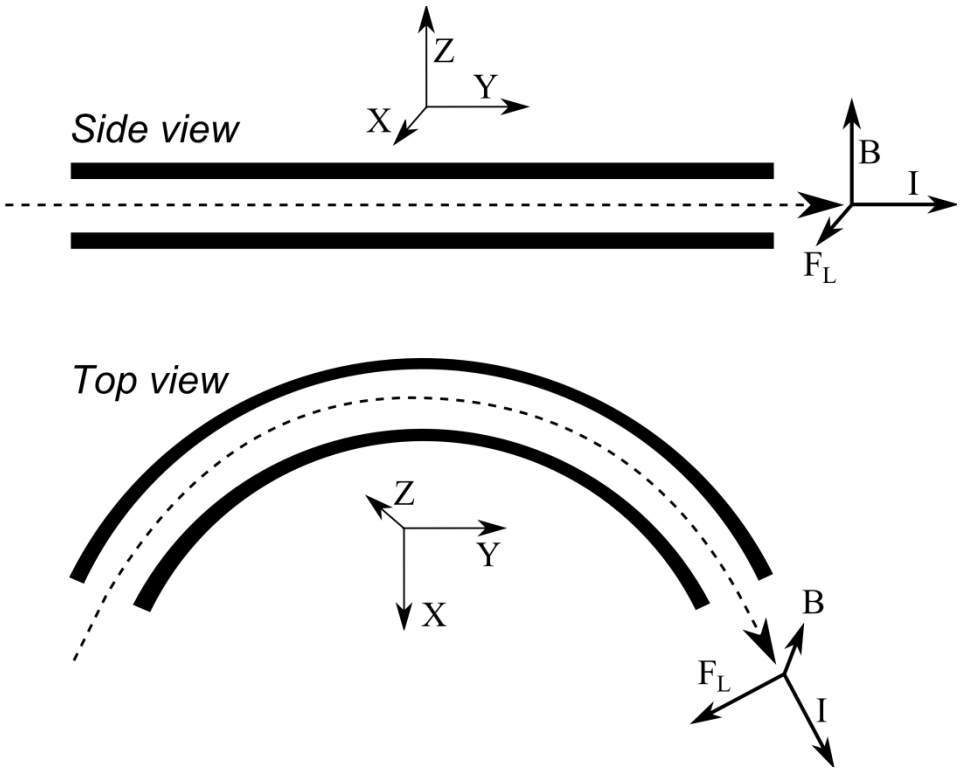

Figure 20. Schematic overview of a magnetic sector and the relationship between the ion current (I), the magnetic field (B) and the Lorentz force (F_L): when the magnet is viewed from the side and from above.

3.2.3 Electrostatic sector

While the magnetic sector works by a magnetic field applied in the direction perpendicular to the curvature of the instrument, the electrostatic sector works by applying an electric field in the same plane as the curvature [69]. For positive ions, a negative potential is applied on the inner plate, while a positive potential is applied on the outer plate. The radial electric field pulls the cation towards the inner plate and is opposed by the momentum of the ion, resulting in a curved flight-path. For a specific ion mass, the curvature of the flight path will match the physical curvature of the electrostatic sector only if the pull of the electric field equals the centripetal force necessary to achieve that curvature for that mass and velocity: $F_e = F_c$. The magnitude of the electric force is qE where E is the electric field strength experienced by the ion; hence, $m/q = rE/v^2$. Again assuming that the initial kinetic energy is given by a constant electric field: $E_k = qU = mv^2/2$, we get $r = 2U/E$ [69]. Thus, the radius only depends on the two electrical fields and not on the ion mass or charge [69]. A distribution of ions given the same kinetic energy by the accelerating field will have different respective velocities dependent upon mass $v = m^{1/2}(2qU)^{1/2}$; consequently, flight times through the electrostatic sector will differ. The electrostatic sector is normally used to separate ions by changes in their kinetic energy. This change in kinetic energy is given by a change in mass during free flight, for instance by evaporation of molecules. We can see from the requirement for passage through the sector, $m/q = rE/v^2$, that a different electric field strength is necessary for clusters with different masses. By scanning the voltage applied

to the electrostatic sector one can detect changes in ion mass taking place. The electrostatic sector has directional focusing properties in the plane of curvature, meaning that small deviations from the optimum ion flight path are corrected (in the x-y plane) [69]. In a hemispherical electrostatic sector, an electric field is applied also orthogonal to the curvature, allowing for focusing in the z-direction as well.

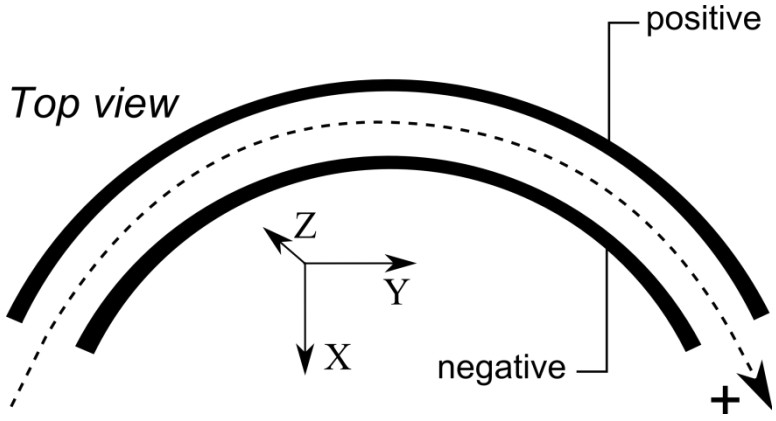

Figure 21. Schematic overview of an electrostatic sector as seen from above.

3.2.4 Experimental procedure

Clusters, $H^+(NH_3)_m(H_2O)_n$, were produced from gas phase molecules attaching to ions produced by corona discharge. The STM needle in the ion source was placed 3–5 mm from the receiving electrode, which in this case was the heated capillary (Figure 19); a potential of 2–4 kV relative the capillary was applied to the needle. Air was bubbled through a flask containing a 25% ammonia solution and led into the ion source compartment in order to increase the available gas phase ammonia molecules. The produced ions passed through a differentially pumped lens system and were accelerated to 50 keV by an electric field. The ions pass through the sector magnet (spanning a 72° angle and having a radius of curvature of 2 m, operating at a pressure of approximately 10^{-6} mbar) where a unique mass-to-charge ratio could be selected. Upon exiting the sector magnet, a field-free-region with a collision cell allows for collision induced dissociation of the cluster ions, using approximately 4×10^{-5} mbar of air. Analysis of cluster ion kinetic energy was performed by a hemispherical electrostatic sector (spanning 180°, radius of curvature 0.15 m) fitted with a channeltron detector.

4 Results and discussion

This chapter summarises the experimental results found in the papers attached to this thesis. The first section deals with the abundance spectra and measured evaporation of H_2O from the various clusters investigated in Papers I–V. Section 4.2 describes the results from cluster reactions with heavy water, as presented in Papers I–III. Cluster reactions with ammonia (Papers IV–V) are covered in Section 4.3, which also describes applying the results to kinetic modelling for atmospheric ion composition. Finally, Section 4.3 contains some of the results obtained with the Separator 1 equipment (Paper VI): collision induced dissociation of clusters containing several water and ammonia molecules.

4.1 Abundance spectra, evaporation and magic numbers

When using the QTOF 2 instrument to perform cluster experiments, it is not necessary to use collision gas. Much information can be obtained by studying the abundance spectra and evaporation patterns of the clusters without influence of gas phase reactions, especially regarding the presence of magic numbers. For many of the studied cluster types it was not previously known whether or not they had magic numbers. For atmospheric science it is particularly interesting to know how clusters containing ammonia or bisulphate evaporate.

4.1.1 Abundance spectra

This chapter will present the abundance spectra collected with the QTOF 2 instrument. The abundance spectra were collected with an empty collision cell, and the quadrupole mass filter set to run in RF-only mode. In order to minimise bias due to the non-constant transmission in the high pass window, the cut-off mass was ramped to cover the entire mass range measured.

Figure 22 shows the abundance spectrum from Paper I, with clusters $H^+(H_2O)_n$ and $H^+(NH_3)_1(H_2O)_n$, produced from 15 mM aqueous NH_3 solution. The prominent magic numbers of protonated water clusters are clearly visible for n = 21, 28, 30, and 55. Interestingly, these magic numbers are found for ammonia-containing clusters as well, except that in this case, the magic number clusters contain one water molecule less, *i.e.* they are found for n = 20, 27, 29 and 54 (although the 29 and 54 magic numbers are weak compared to the pure water cluster counterparts). There is also a magic number for the cluster $H^+(NH_3)_1(H_2O)_{18}$ (m/z = 342) that does not have a counterpart among the pure water clusters. Magic numbers for ammonia-containing clusters have been observed previously by Shinohara *et al.* [71, 72]. In addition to the magic numbers $H^+(NH_3)_1(H_2O)_{20}$ and $H^+(NH_3)_1(H_2O)_{27}$, they also found magic numbers for clusters containing more than one ammonia molecule: $H^+(NH_3)_m(H_2O)_{20}$ with m = 2–6 and $H^+(NH_3)_2(H_2O)_{26}$.

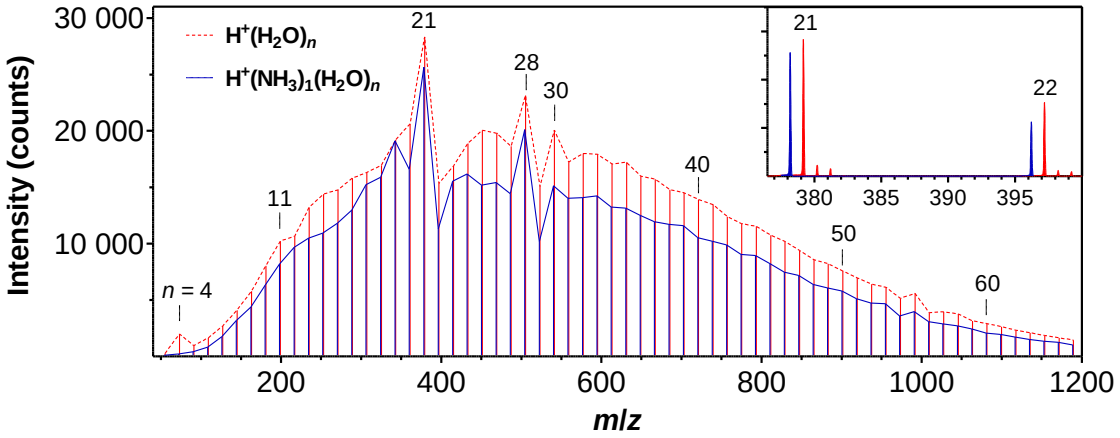

Figure 22. Abundance spectrum from Paper I, showing $H^+(H_2O)_n$ and $H^+(NH_3)_1(H_2O)_n$ clusters. The numbers above the distributions indicate the number of molecules for certain $H^+(H_2O)_n$ clusters. The inset shows a magnified region of the spectrum.

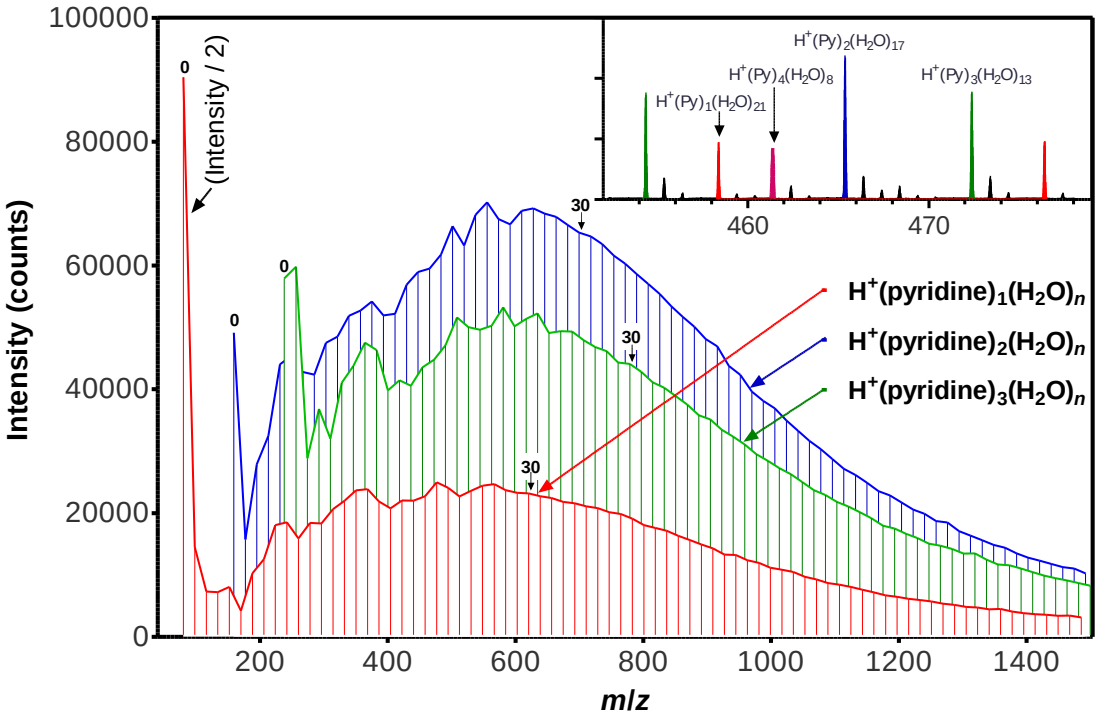

Figure 23. Abundance spectrum from Paper II, produced from 100 mM aqueous pyridine solution. Clusters shown are $H^+(pyridine)_1(H_2O)_n$, $H^+(pyridine)_2(H_2O)_n$ and $H^+(pyridine)_3(H_2O)_n$. n = 0 and 30 is marked for all clusters. The inset shows a magnified region of the spectrum.

Figure 23 above shows an abundance spectrum from Paper II, produced by spraying a 100 mM pyridine solution (note that one peak is shown with halved intensity). As can be seen, some ions in Figure 23 have an exceptionally high intensity. For the clusters $H^+(pyridine)_1$, $H^+(pyridine)_1(H_2O)$, and $H^+(pyridine)_2$, the intensity in the beam saturates the detector and peak splitting occurs. Hence for these peaks, the true abundance is higher than what is shown in Figure 23. Figure 23 also shows unusually high intensities for the clusters $H^+(pyridine)_3$, and $H^+(pyridine)_3(H_2O)_1$, the latter being

somewhat greater. This was also observed by Li *et al.* [73]. From the inset in Figure 23, it is evident that clusters with four pyridine molecules can be found in abundances similar to those of $H^+(pyridine)_1(H_2O)_n$; however, they are omitted from the spectrum for clarity. None of the other pyridine clusters exhibit intensities that would suggest a magic number in the present size range. The small protonated pyridine monomer, dimer, trimer and singly-hydrated trimer might be suspected to be overrepresented if these clusters are found in the atmosphere (the protonated monomer has been measured [44, 45]). However, this is also a question of kinetics, since the degree of hydration of these core ions will be a reflection of the air water-content.

Figure 24 shows an abundance spectrum obtained from a solution with 30 mM NH_3 and 2.5 mM pyridine (from Paper V). The resulting clusters were $H^+(NH_3)_1(H_2O)_n$, $H^+(pyridine)_1(H_2O)_n$, $H^+(pyridine)_2(H_2O)_n$ and $H^+(NH_3)_1(pyridine)_1(H_2O)_n$. The former three cluster series have already been discussed, and it is sufficient to say that the measured cluster distributions are in agreement with the results presented in Figure 22 and Figure 23. Interestingly, the cluster type $H^+(NH_3)_1(pyridine)_1(H_2O)_n$ can be seen to have the same magic numbers as the $H^+(NH_3)_1(H_2O)_n$ clusters. As previously stated, the $H^+(H_2O)_n$ and $H^+(NH_3)_1(H_2O)_n$ clusters share magic numbers, except that in the latter case, the ammonia molecule replaces one H_2O. The addition of a pyridine molecule to these two cluster types results in $H^+(pyridine)_1(H_2O)_n$ and $H^+(NH_3)_1(pyridine)_1(H_2O)_n$, where the former loses all its magic numbers and the latter retains them. This is discussed further in Section 4.3.2 where the $H^+(pyridine)_1(H_2O)_n$ forms $H^+(NH_3)_1(pyridine)_1(H_2O)_n$ by reacting with NH_3.

An abundance spectrum of $HSO_4^-(H_2O)_n$, $OH^-(H_2O)_n$ and $SO_4^{2-}(H_2O)_n$ clusters produced from a solution of 15 mM $NaHSO_4$ and 15 mM crown ether is shown in Figure 25. In addition to the high abundance displayed by the bisulphate ion, magic numbers are indicated for bisulphate-containing clusters with 5, 12, 14, 20, 26 and 28 water molecules. While the magic numbers are not so dramatic in their appearance as in the $H^+(H_2O)_n$ series, many of them display the characteristic z-shaped kink in the curve when their larger neighbour has lower than expected abundance.

The $OH^-(H_2O)_n$ abundance in Figure 25 shows some peaks that might be considered weaker magic numbers: n = 11, 13, 17, 21 and 30. The detailed structure exhibited by the $OH^-(H_2O)_n$ series in Figure 25 is in good agreement with previously published abundance spectra using the same equipment [56]. However, the high intensity seen for n = 30 is absent in the latter, instead there is somewhat enhanced intensity for n = 31 followed by a decrease in abundance for n = 32. The strong magic number found at m/z = 989 (n = 54) [56] is outside the spectrum range in Figure 25. An $OH^-(H_2O)_n$ abundance spectrum measured by Yang and Castleman [74] using a fast flow reactor showed weak magic numbers for n = 11, 14, 17, 20 and 30, some of which are shared by the spectra in Figure 25, some of which are not. The clusters containing SO_4^{2-} show an interesting odd/even effect with alternating higher and lower intensities. This pattern is broken by the clusters following n = 23, and by the clusters surrounding n = 36. Also note that due to the clusters carrying two charges, their actual mass is twice that of the other cluster series in the spectrum.

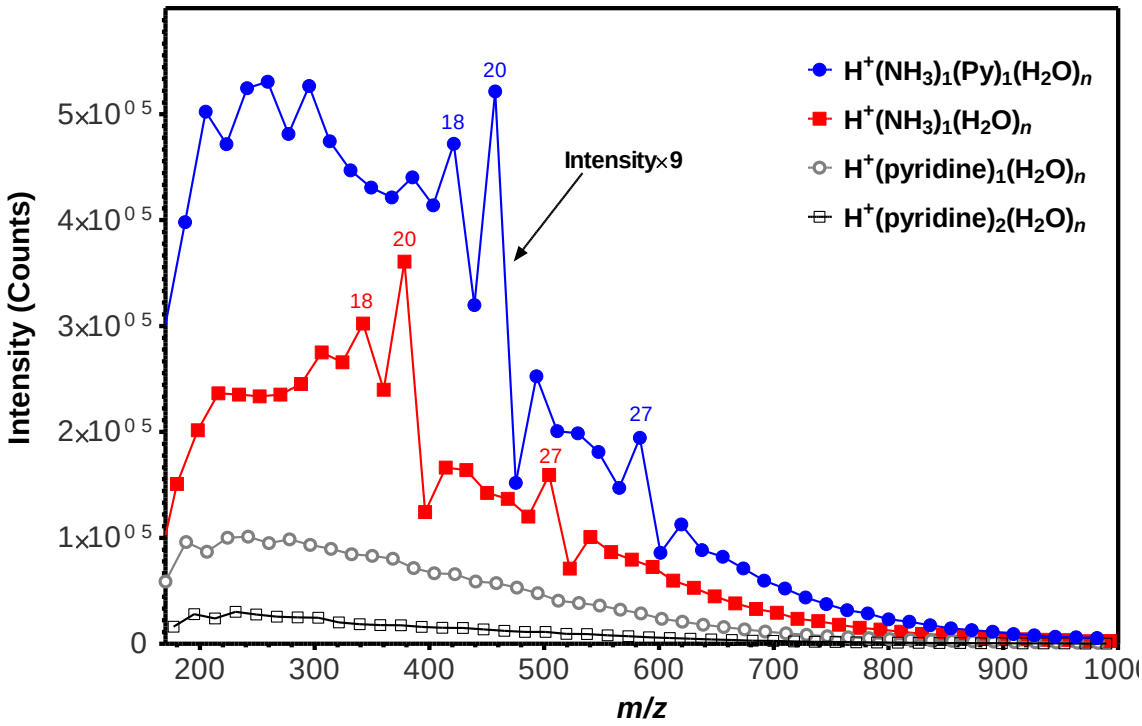

Figure 24. Abundance spectrum from Paper V. obtained from a solution with 30 mM NH_3 and 2.5 mM pyridine. The $H^+(NH_3)_1(pyridine)_1(H_2O)_n$ clusters are shown with the intensity increased nine-fold for clarity. Some peaks in the $H^+(NH_3)_1(H_2O)_n$ and $H^+(NH_3)_1(pyridine)_1(H_2O)_n$ series are labelled with the number of water molecules in the cluster.

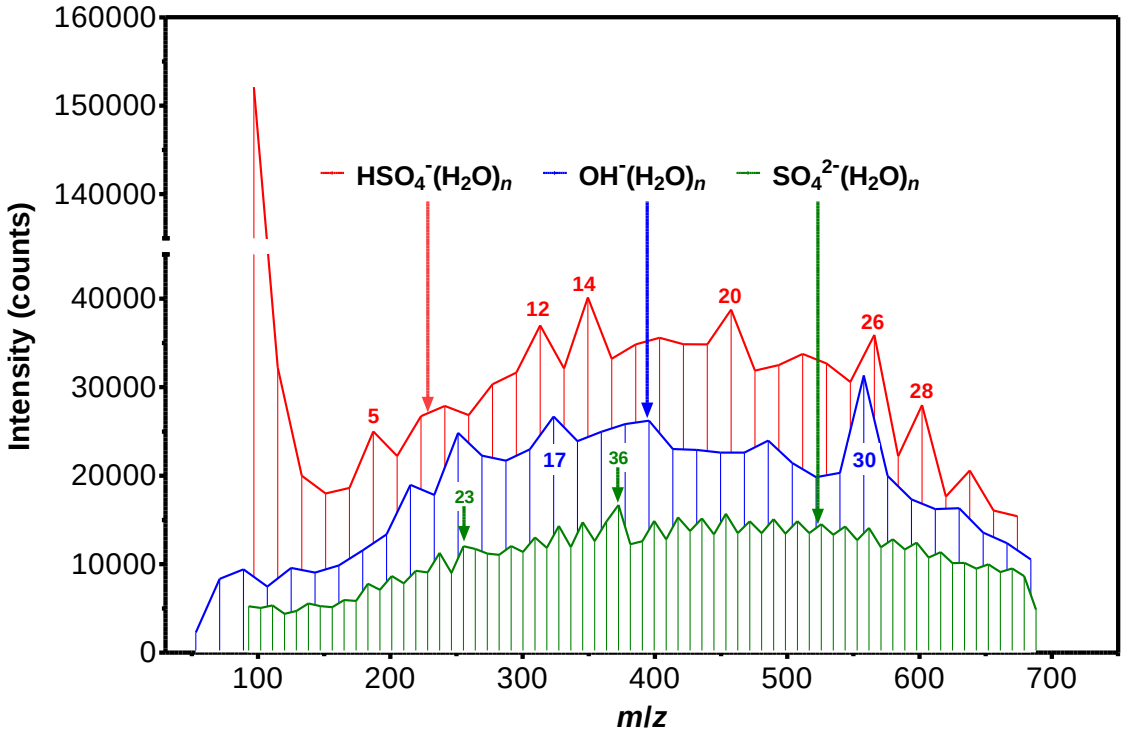

Figure 25. Abundance spectrum from Paper III, showing $HSO_4^-(H_2O)_n$, $OH^-(H_2O)_n$ and $SO_4^{2-}(H_2O)_n$ clusters, produced from a solution of 15 mM $NaHSO_4$ and 15 mM crown ether. The numbers indicate the amount of water molecules in the clusters.

4.1.2 Evaporation patterns

Spontaneous evaporation from clusters was measured by passing them through an empty collision cell at velocities that would correspond to a centre-of-mass energy of 0.1 eV if they would collide with D_2O (Paper I–III) or a centre-of-mass energy of 0.085 eV if they were to collide with NH_3 (Paper V). In some experiments a lower limit of 0.6 eV in the lab-frame was used for clusters of mass less than 100 u. Since the cluster velocity through the cell varies as the square root of the reduced mass when the centre-of-mass energy is kept constant, the flight time is essentially the same for all cluster sizes in the investigated range (see "Experimental time frame" in Table 4). More importantly, the difference in flight time is negligible for clusters of adjacent sizes. The relative intensity of the first step evaporation, *i.e.* the loss of one H_2O molecule from the cluster, is shown in Figure 26 for all investigated clusters. The general trend is that evaporation of a water molecule increases in a fairly linear fashion with cluster size.

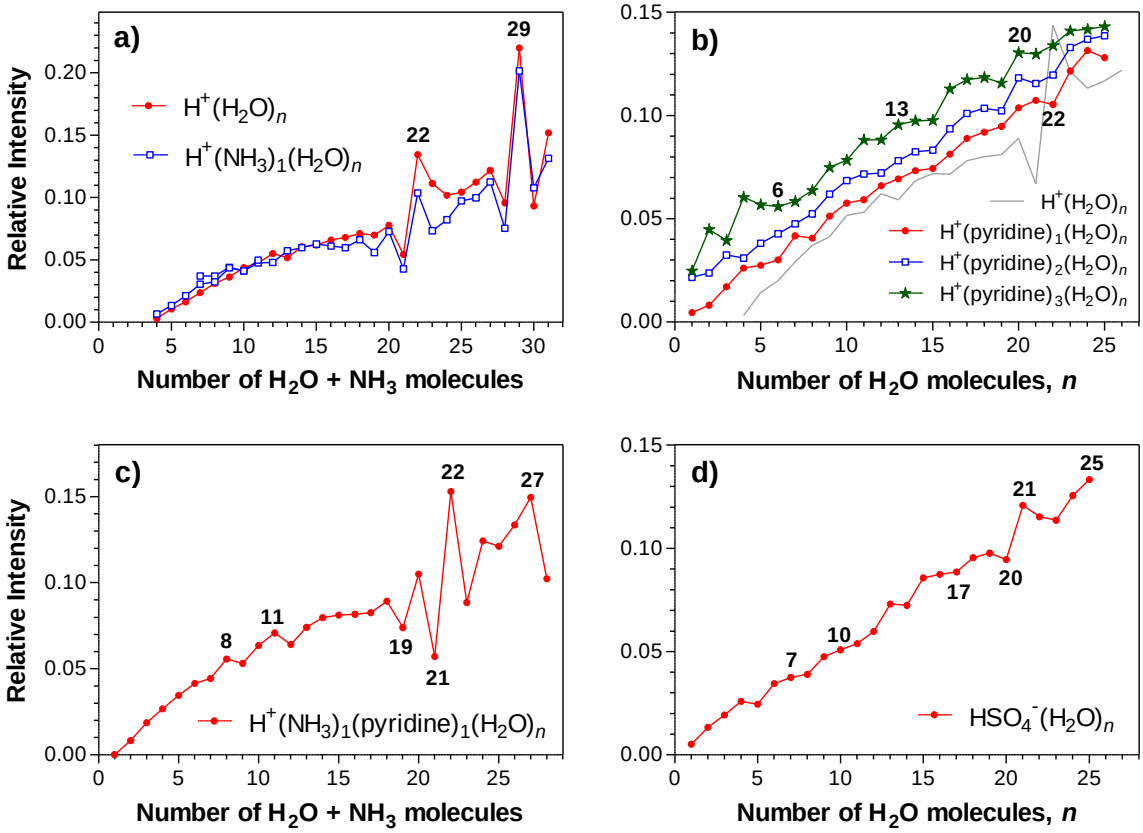

Figure 26. The relative abundance of clusters that have lost one water molecule when passing through the empty collision cell. a) $H^+(H_2O)_n$ and $H^+(NH_3)_1(H_2O)_n$ as function of the number of molecules in the cluster. b) $H^+(pyridine)_{1-3}(H_2O)_n$ as function of the number of H_2O in the cluster, a $H^+(H_2O)_n$ measurement is shown for comparison. c) $H^+(NH_3)_1(pyridine)_1(H_2O)_n$ as function of the number of H_2O and NH_3 molecules in the cluster. d) $HSO_4^-(H_2O)_n$ as a function of the number of H_2O in the cluster.

Figure 26a shows the relative abundance of $H^+(H_2O)_n$ and $H^+(NH_3)_1(H_2O)_n$ clusters (Paper I) that lost one water molecule during their flight through the QTOF 2 instrument collision chamber, *i.e.* it is the relative abundance of the $m/z - 18$ peak that is shown. The evaporation intensity is presented as a function of the total number of molecules in the cluster, H_2O or NH_3. Again we note the very similar behaviour of pure water clusters and clusters containing an ammonia molecule (*cf.* Section 4.1.1), indicating similar structural properties and/or energetics. A marked increase in evaporation is evident for both cluster types having 22 or 29 molecules (water or ammonia). In addition, evaporation is suppressed for clusters with 21, 28 and 30 molecules. The evaporation patterns seen in Figure 26a clearly mirrors the abundance of magic numbers presented in the abundance spectrum in Figure 22: evaporation is suppressed for a magic number and is enhanced for the clusters being one size larger than a magic one.

The corresponding evaporation measurements for clusters containing water and pyridine, $H^+(pyridine)_{1-3}(H_2O)_n$, are shown in Figure 26b, along with a $H^+(H_2O)_n$ curve measured simultaneously for reference. In this case, the abundances are given as a function of the number of water molecules in the clusters. Again we see a general trend that evaporation of one H_2O increases—quite linearly—with the number of water molecules n in the clusters. No clear magic numbers are indicated for pyridine-containing clusters in this size range, in agreement with the findings from the abundance spectrum. There is a clear similarity in the fine-structure of the $H^+(pyridine)_2(H_2O)_n$ and $H^+(pyridine)_3(H_2O)_n$ curves for $n \geq 15$ which might be significant; the similarity in shape of the curves is not shared by the $H^+(pyridine)_1(H_2O)_n$ clusters. Evaporation also increases with the number of pyridine molecules present in the cluster. Overall, the addition of one pyridine molecule seems to be equivalent of adding 2–3 water molecules. This is a clear contrast to Figure 26a, where we see a very close overlapping between the $H^+(H_2O)_n$ and $H^+(NH_3)_1(H_2O)_n$ clusters. These findings may be related to the increase in the number of internal degrees-of-freedom of a cluster as more pyridine molecules are present. No real evaporation of pyridine molecules was observed for any of the $H^+(Pyridine)_{1-3}(H_2O)_n$ clusters with $n > 0$. The highest observed relative abundance at $m/z - 80$ was less than 0.0004. It would seem that pyridine molecules are reluctant to leave their clusters; even if as many as three of them are present.

The loss of H_2O from the $H^+(NH_3)_1(pyridine)_1(H_2O)_n$ cluster is shown in Figure 26c. The detailed structure of the abundance spectrum in Figure 24 is mirrored by the evaporation pattern for this cluster also, especially for the prominent magic number clusters containing 19, 21 and 28 water or ammonia molecules. Just as the magic numbers in the abundance spectrum were found to mimic those of the $H^+(NH_3)_1(H_2O)_n$ cluster, the evaporation pattern of the two cluster types is also very similar.

The evaporation pattern of bisulphate containing water clusters in Figure 26d again correlates well with the abundance spectrum (Figure 25). The deviations from the straight line due to magic numbers are small compared to the $H^+(H_2O)_n$ and $H^+(NH_3)_1(H_2O)_n$ clusters. Nevertheless, there are shallow dips for $n = 5$ and 14 observed in Figure 26d that correspond with the increased intensity for these clusters in the abundance spectrum. The peak for $HSO_4^-(H_2O)_{12}$, that shows a somewhat higher intensity in the abundance spectrum, is not represented by any particular change in intensity in the evaporation plot. Possibly, the increased intensity might not be due to a particularly stable $n = 12$ cluster: but due to an unstable $n = 13$ cluster. The magic

number $HSO_4^-(H_2O)_{20}$, which in Figure 25 can be seen to be followed by a sharp decrease to somewhat lower than expected intensity for $HSO_4^-(H_2O)_{21}$, is mirrored well by the evaporation pattern: a decrease for n = 20, followed by increased evaporation for n = 21.

4.2 Reactions of clusters with D_2O

This section describes the reactions of the clusters $H^+(H_2O)_n$, $H^+(NH_3)_1(H_2O)_n$, $H^+(\text{pyridine})_{1-3}(H_2O)_n$ and $HSO_4^-(H_2O)_n$ with D_2O.

4.2.1 The effect of D_2O on cluster evaporation

The presence of collision gas in the flight path of the cluster ions might influence the way clusters evaporate. In turn, the way clusters evaporate might affect which products are formed in a reaction and to which extent. When performing the experiments with D_2O, one question was whether evaporation of H_2O from clusters is enhanced by the collision gas or not. Figure 27 shows the evaporation curves from Figure 26b (protonated clusters containing 0–3 pyridine molecules and water) accompanied by curves representing the same measurements with D_2O present in the collision cell.

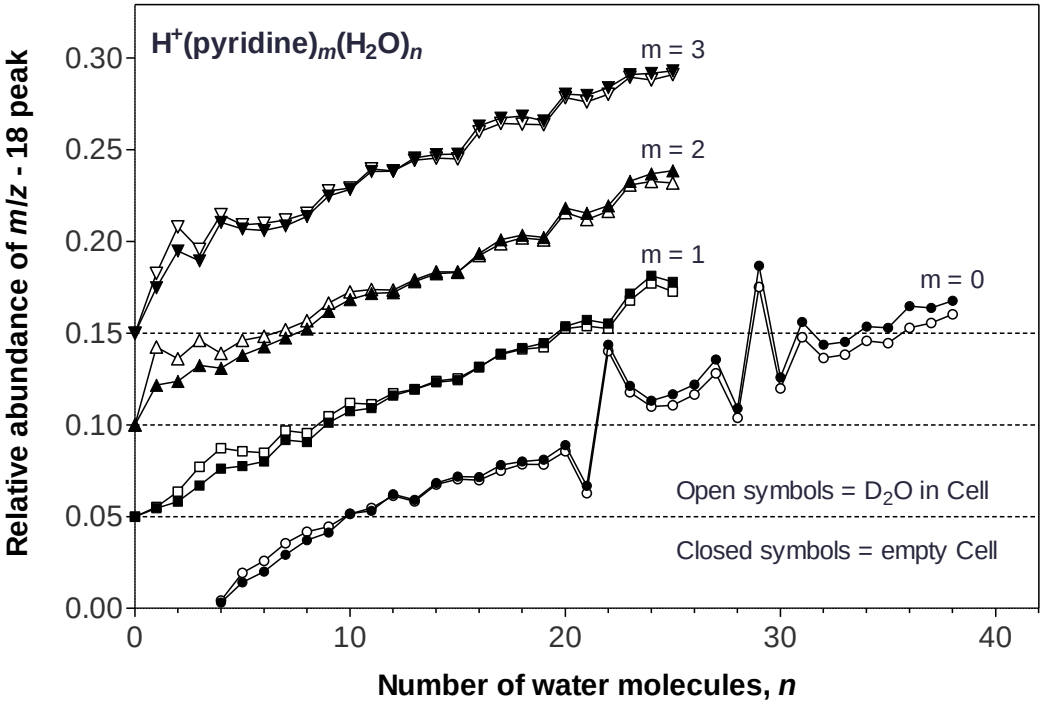

Figure 27. The effect of D_2O in the collision cell on the* m/z *– 18 peak. Three pairs of curves are shown, from top down: $H^+(\text{pyridine})_3(H_2O)_n$, $H^+(\text{pyridine})_2(H_2O)_n$, $H^+(\text{pyridine})_1(H_2O)_n$ and $H^+(H_2O)_n$. Each pair of curves is shifted by 0.05 for clarity. Open and closed symbols signify the presence and absence of D_2O in the cell, respectively.

As seen in Figure 27, the size of the $m/z - 18$ peak is largely unaffected by the presence of D_2O collision gas. This is reasonable considering that the majority (≈90%) of the clusters do not collide with D_2O, and would therefore not behave any differently.

For the clusters that do react with D_2O, the majority will have experienced increased cluster mass after decomposition of the reaction intermediate (Figure 7, Figure 8). Even if the rate of evaporation for a reaction product is greater than for a reactant, this is unlikely to be detected in the $m/z - 18$ peak because most evaporation products would end at $m/z - 17$ and $m/z - 16$. For smaller clusters—where the probability of D_2O leaving the reaction complex is not insignificant—there should be an increase in intensity of the $m/z - 18$ peak if there was an increased evaporation rate for products after the collapse of the reaction intermediate. For the smallest clusters there is a slight enhancement in evaporation when collision gas is present. However, this may also originate from evaporation of a HDO or D_2O molecule from a cluster that has reacted to form products containing these molecules—possibly without an accompanying increase in evaporation rate. The probability of spontaneous evaporation of HDO or D_2O from a product would also only be significant for smaller clusters.

There is a slight decrease in the $m/z - 18$ peak with collision gas present for the largest clusters in Figure 27, most evident for the curve for pure water clusters ($m = 0$). As the cross section increases with size the probability for evaporated clusters ($m/z - 18$) to collide and react with the collision gas is higher. This leads to products of $m/z - 17$ and $m/z - 16$. The other possibility is that, as larger number of clusters react, fewer parent ion clusters are left to form the $m/z - 18$ clusters upon evaporation. Instead they form the $m/z - 17$ and $m/z - 16$ ions. Thus, there are two ways to form the $m/z - 17$ and $m/z - 16$ peaks: reaction of evaporated clusters and evaporation from reacted clusters. As will be discussed in Section 4.2.2 the latter mechanism tends to dominate.

The total first-step-evaporation (combined intensity of the −18, −17 and −16 peaks) is shown in Figure 28 for an empty collision cell and for D_2O collision gas. There is a clear signal that evaporation increases with D_2O when including the additional peaks. Since the $m/z - 18$ peak remained largely unchanged in Figure 27 above, the increase in total evaporation can be attributed to an increased evaporation of H_2O from product clusters.

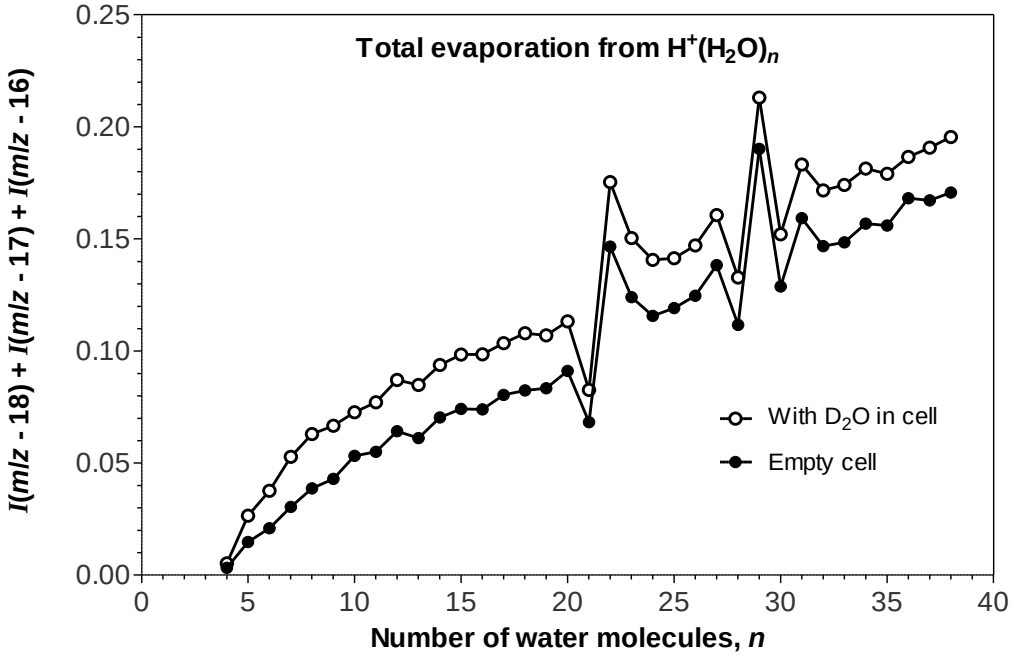

Figure 28. Total evaporation of a water molecule (H_2O, D_2O or HDO) from a pure protonated water cluster $H^+(H_2O)_n$ dependent upon if it passes through and empty collision cell (closed symbols) or a collision cell with D_2O (open symbols).

4.2.2 The fraction of exchange and cross section

The cross section for a reaction is a measure of the reactivity of that cluster–molecule interaction and is of interest should one want to know how fast water molecules adsorb to clusters. While D_2O reactions are not directly relevant for the atmosphere, they are used here instead of H_2O in order to enable the detection of products. The molecules are similar enough to consider any results as interchangeable with H_2O.

For the reaction of a cluster ion with D_2O we define the fraction of exchange (Φ) as the sum of the normalised product peaks where one or two deuterium atoms have been incorporated into the cluster (the reaction pathways (5b) and (5c) in Section 2.3.4). Thus, $\Phi = I(m/z + 1) + I(m/z + 2)$.

The fraction of exchange is assumed to be the same as the actual fraction of clusters that react with D_2O. The fraction of exchange misses the intensity from reactions where D_2O molecules leave when the reaction complex fragments (Reaction (5a)). Unfortunately, there is no way in our experiments to detect these products. However, the missing reaction pathway represents negligible abundance (Figure 7 and Figure 8).

As mentioned in the previous section, it is possible to have evaporation of water molecules from a product cluster. It warrants consideration, because it will reduce the measured fraction of exchange. The main loss of water due to post reaction evaporation will be in the form of H_2O, especially for larger clusters. The primary effect is therefore a loss of intensity from the $m/z + 1$ and $m/z + 2$ product peaks to the $m/z - 17$ and $m/z - 16$ peaks respectively. This can be compensated for by adding the intensity of the latter peaks to the fraction of exchange, thus producing the corrected fraction of

exchange $\Phi_{corr} = I(m/z+1) + I(m/z+2) + I(m/z-17) + I(m/z-16)$. However, one should make sure that the intensity measured in the $m/z-17$ and $m/z-16$ peaks do indeed originate from additional fragmentation of a product, and not from the reaction of a $H^+(H_2O)_{n-1}$ reactant. The fraction of exchange, the combined intensity of the $I(m/z-17)$ and $I(m/z-16)$ peaks as well as the corrected fraction of exchange is shown below in Figure 29 for the experiment where $H^+(NH_3)_{0-1}(H_2O)_n$ reacts with D_2O at 0.1 eV reduced collision energy (Paper I).

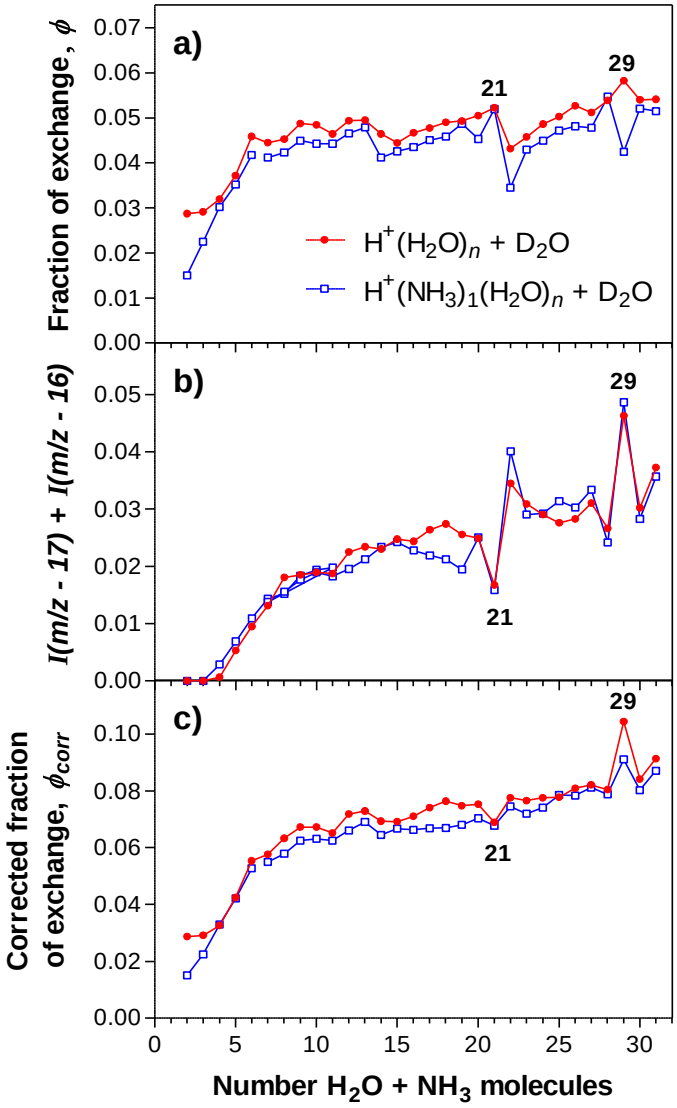

Figure 29. (a) The fraction of exchange (Φ) for the reaction $H^+(NH_3)_{0-1}(H_2O)_n$ colliding with D_2O. (b) Combined intensity for the fragmentation peaks I(m/z – 17) and I(m/z – 16). (c) The fraction of exchange corrected for post-reaction evaporation of H_2O. The number of molecules in the cluster is given on the abscissa. E_{COM} = 0.1 eV was used, except when the number of molecules was 5 or less, in which case E_{LAB} = 0.6 eV was used.

The shapes of the curves in Figure 29a is influenced by the magic numbers for $H^+(H_2O)_n$ and $H^+(NH_3)_1(H_2O)_n$ (Section 4.1). The post reaction evaporation depends on the stability of the clusters, resulting in decreased evaporation from magic numbers and increased evaporation for their larger neighbours. Hence the mirrored appearance of the curves in Figure 29a and b, indicating that the $m/z - 17$ and $m/z - 16$ peaks constitute "missing" intensity from the primary product peaks. This conclusion is further supported by the comparably smooth nature of the corrected fraction of exchange. The smooth curve in Figure 29c further indicates that cluster stability and magic numbers have little influence on the actual reaction cross section. Because the reaction cross section (Equation (2)) is essentially proportional to the fraction of exchange, the cross sections for reactions with D_2O are almost identical for $H^+(H_2O)_n$ and $H^+(NH_3)_1(H_2O)_n$ given the same number of cluster molecules. The two cluster types are nearly equal in size and the charge state is identical; their difference lies in their protonation site and proton mobility. In a $H^+(H_2O)_n$ cluster the proton is free to move, while in a $H^+(NH_3)_1(H_2O)_n$ cluster the proton is bound to the ammonia molecule, forming a NH_4^+ core ion (Section 4.2.3). Furthermore, there may be a difference between the clusters regarding whether the proton is found at the cluster surface or if it is found at the cluster centre; the term "core ion" for NH_4^+ is used here in the sense of a fundamental constituent of the cluster ion and do not necessarily imply that it is located at the centre of the cluster. Nevertheless, these differences between $H^+(H_2O)_n$ and $H^+(NH_3)_1(H_2O)_n$ clusters do not influence the fraction of exchange to any detectable degree.

Of the two models of Kummerlöve and Beyer ([54], Section 2.3.2), the Hard Sphere Average Dipole Orientation (HSA) model assumes a charge fixed in position at the cluster centre, and results in lower cross sections than the Surface Charge Capture (SCC) model. The HSA model is relevant for ammonia-containing clusters provided the NH_4^+ is found at the cluster centre. The SCC model assumes that the charge moves freely in the cluster and is drawn to the surface by the dipole interaction. The SCC model would therefore be expected to give satisfactory results for pure protonated water clusters. The SCC model may also work for $H^+(NH_3)_1(H_2O)_n$ clusters provided that the ammonium molecule itself is mobile within the clusters, or, if the charge is located at the surface, the moment of inertia of the cluster is sufficiently low to allow for reorientation towards the dipole. Nevertheless, given that the experimentally determined cross sections of the two clusters are nearly identical, a similar mechanism for the dipole attraction is expected.

The cross section for the reaction between collision gas and clusters can be calculated as $\sigma = -\ln(I/I_0)/(cL)$, where c is the collision gas concentration, L the length of the collision cell, and I_0 and I represent the intensity of the parent cluster ion in the beam before and after the collision cell, respectively (Section 2.3.2). The entity I/I_0 is of course related to the fraction of clusters that react in the collision cell and equals $1-\Phi$. Due to the difficulty of measuring the pressure of the approximately 10^{-5} mbar D_2O in the collision cell with any reasonable accuracy, only a relative cross section (σ_r) can be obtained. Still, this gives a qualitative picture of the cross sectional size dependence. Furthermore, it makes it possible to calculate cross section values for all clusters, should a reference value be available. The relative cross section corrected for post reaction evaporation is given in Figure 30 for an experiment where clusters containing a proton, 0–3 pyridine molecules and n water molecules react with D_2O at E_{COM} = 0.1 eV. The cross sections are given relative to the uncorrected cross section of the $H^+(H_2O)_{11}$ cluster (*cf.* Paper II).

There is a clear trend that cross sections increase with the number of water molecules. The number of pyridine molecules in the cluster seems to have little effect apart from the fact that $H^+(H_2O)_n$ clusters have up to 40% larger cross section for n = 5–20 water molecules. Given the trends of the pyridine-containing clusters in Figure 30, it seems likely that they will overlap with the curve for pure water clusters as the number of water molecules increases above 25. Kummerlöwe and Beyer [54] suggested that the HSA and SCC models could be calculated to give a lower and an upper collision cross section limit. In both cases, the collision cross sections between pure water clusters and D_2O at velocities corresponding to E_{COM} = 0.1 eV were calculated (Table 7). The computed HSA and SCC cross sections were linearly scaled to produce a fit to the corrected relative cross sections of the pyridine-containing clusters in Figure 30. Both models were equally able to reproduce the shape of the curves, thus only the HSA model is shown for clarity.

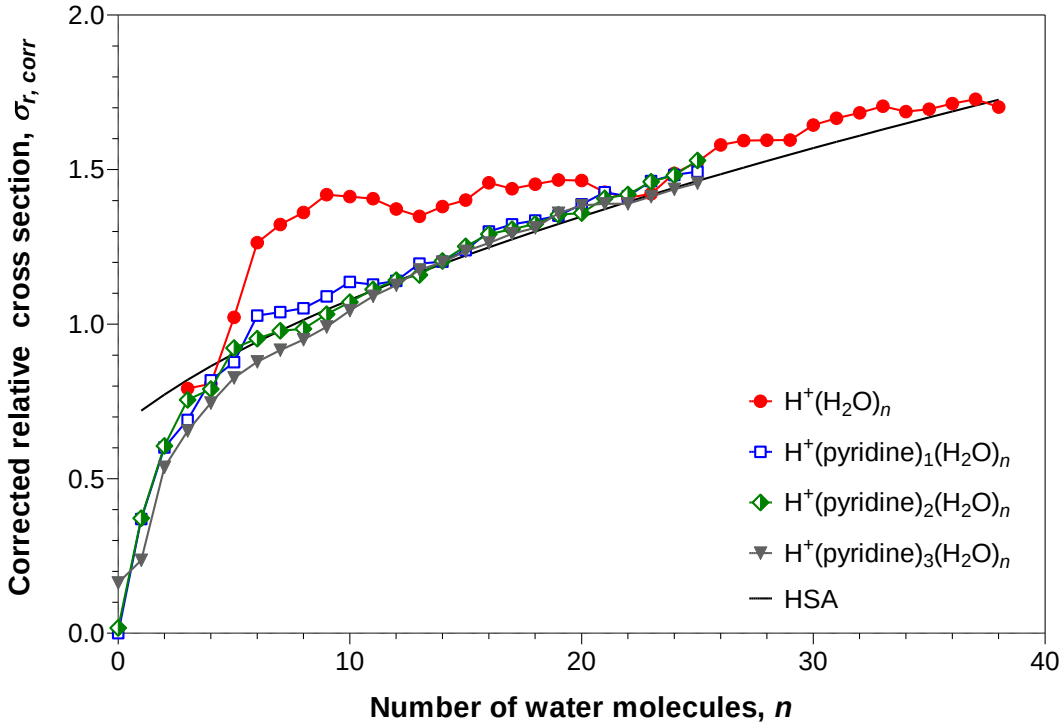

Figure 30. The relative cross sections for the reaction between clusters $H^+(pyridine)_{0-3}(H_2O)_n$ and D_2O at 0.1 eV reduced collision energy (0.6 eV in the lab frame below 100 u). Also shown is a fitted curve for the Hard Sphere Average dipole model.

Interestingly enough, the HSA and SCC models produce good fits when scaled to the size dependent cross sections of pyridine-containing clusters and perform more poorly when compared with the water clusters for which they were calculated. However, for n = 4, both models compare rather well to experimentally determined values, some of which are shown in Table 8.

Table 7. Collision cross sections for $H^+(H_2O)_n + D_2O$ at velocities corresponding to E_{COM} = 0.1 eV calculated using the HSA and SCC models.

n	v (ms^{-1})	σ_{HSA} (10^{-18} m^2)	σ_{SCC} (10^{-18} m^2)	Average (10^{-18} m^2)
1	1407	1.13	1.93	1.53
4	1109	1.36	2.51	1.94
5	1085	1.42	2.64	2.03
10	1035	1.70	3.16	2.43
15	1018	1.92	3.55	2.74
20	1009	2.12	3.87	3.00
25	1004	2.30	4.16	3.23
30	1000	2.47	4.42	3.44
35	998	2.63	4.65	3.64

Table 8. Previously measured cross sections (σ) for the reaction $H^+(H_2O)_4 + D_2O$.

Reaction	E_{COM} (eV)	σ (10^{-18} m^2)	Reference
$H^+(H_2O)_4 + D_2O$	0.1	1.0	Honma and Armentrout [65]
$H^+(H_2O)_4 + D_2O$	0.1	1.45	Yamaguchi *et al.* [66]

4.2.3 The κ_{HDO} ratio—the reactions where HDO leaves the cluster

The ratio κ_{HDO}, defined as $I(m/z+1)/(I(m/z+1)+I(m/z+2))$ relates the extent to which a water-containing cluster reacts with D_2O to form a product where one protium is exchanged for one deuterium (Reaction (5b)). Thus, it is an indication of whether H/D rearrangements take place between water molecules in the reaction intermediate or not. The ratio κ_{HDO} is expected to vary between 0 (for a cluster with no H/D exchange) and a value representing evaporation of a random water molecule from a cluster with a completely random H/D distribution. For a cluster with $2n+1$ protium atoms—like a pure protonated water cluster—the latter value is $\kappa_{HDO} = 2/(2+n)$ if the collision gas is pure D_2O (Section 2.3.4).

Proton mobility in the clusters is a requirement for the H/D exchange mechanism to take place [65-67]. The presence or absence of charge mobility yields important information on possible cluster structures and charge location. The κ_{HDO} ratio also connects with other aspects of cluster reactions. For instance, the mechanism by which the cluster charge attracts a dipole might depend on the mobility of the charge (*cf.* The HSA and SCC cross section [54]).

Figure 31 shows κ_{HDO} for the two cluster types studied in Paper I: $H^+(H_2O)_n$ and $H^+(NH_3)_1(H_2O)_n$. Also included are curves for randomised intermediates with a pure D_2O collision gas (solid line) and for a contaminated collision gas with 4% HDO (dashed line). The highest degree of HDO contamination is estimated by the lowest single value of measured κ_{HDO}. Thus, from the κ_{HDO} values for $H^+(NH_3)_1(H_2O)_n$ in Figure 31, 4% HDO contamination is estimated. This estimate is also supported by the agreement between the $H^+(H_2O)_n$ curve and the 4% HDO curve for larger n. For $H^+(H_2O)_n$ clusters, 0.6 eV collision energy in the lab frame was used for n = 2–5, and for the other sizes 0.1 eV (COM) was used. For $H^+(NH_3)_1(H_2O)_n$ clusters, E_{LAB} = 0.6 eV was used for n = 1–10, and E_{COM} = 0.1 eV was used for n = 6–30. Hence there are two data points for certain clusters in Figure 31.

Although the pure water clusters and ammonia-containing clusters have been shown to be similar in the case of magic numbers, evaporation and cross section, here they show a dramatic difference in behaviour. The pure water clusters exhibit H/D exchange reactions to a degree that corresponds to a cluster with complete hydrogen scrambling, while this reaction channel is absent for $H^+(NH_3)_1(H_2O)_n$ as is evident from the low κ_{HDO} values. This indicates that the proton in the reaction complex $[H^+(NH_3)_1(H_2O)_n(D_2O)]^*$ is not free, but bound to a single molecule—ammonia being the obvious candidate in light of it being a better base than water. Proton affinities and pK_a values are found in Table 9. As can be seen, the proton affinity of ammonia is greater than that of a single water molecule. As cluster size increases, the proton affinity of combined water molecules increases until it reaches bulk value; however, the proton affinity of ammonia in bulk remains greater. Work by Khan [75] on possible sites of protonation for the $H^+(NH_3)_1(H_2O)_{20}$ cluster indicates that transfer of a proton in the manner: $(NH^+_4)_1(H_2O)_{20} \rightarrow (NH_3)_1(H_3O^+)_1(H_2O)_{19}$ costs roughly 1 eV (≈96.5 kJmol^{-1}).

Table 9. Proton affinities and acid dissociation constants relevant for the experiments presented in this thesis.

Compound	Proton affinity (kJmol^{-1})	Proton affinity in water (kJmol^{-1})	pK_a of conjugate acid
H_2O	723 [76], 691 [35]	1130 [76]	
$(H_2O)_3$	888 [77]		
NH_3	865 [76], 853.6 [35]	1182 [76]	9.25 [78]
pyridine	930 [35]	1160 [76]	5.23 [79]

Numbers in brackets indicate references. All values given for T = 298 K.

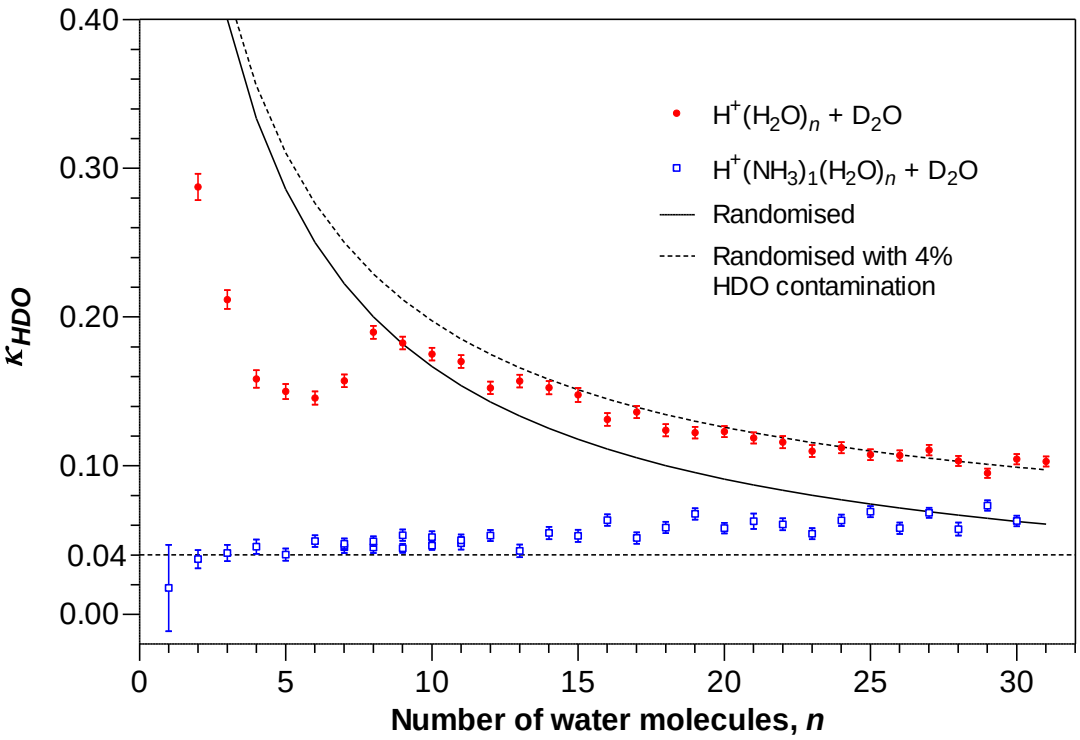

Figure 31. *κ_{HDO} for clusters $H^+(H_2O)_n$ and $H^+(NH_3)_1(H_2O)_n$ reacting with D_2O. Also included for each point is one statistical standard deviation. Curves representing the expected κ_{HDO} value for a water cluster with a completely randomised hydrogen distribution are shown for pure D_2O and for the case of 4% contamination of the D_2O by HDO.*

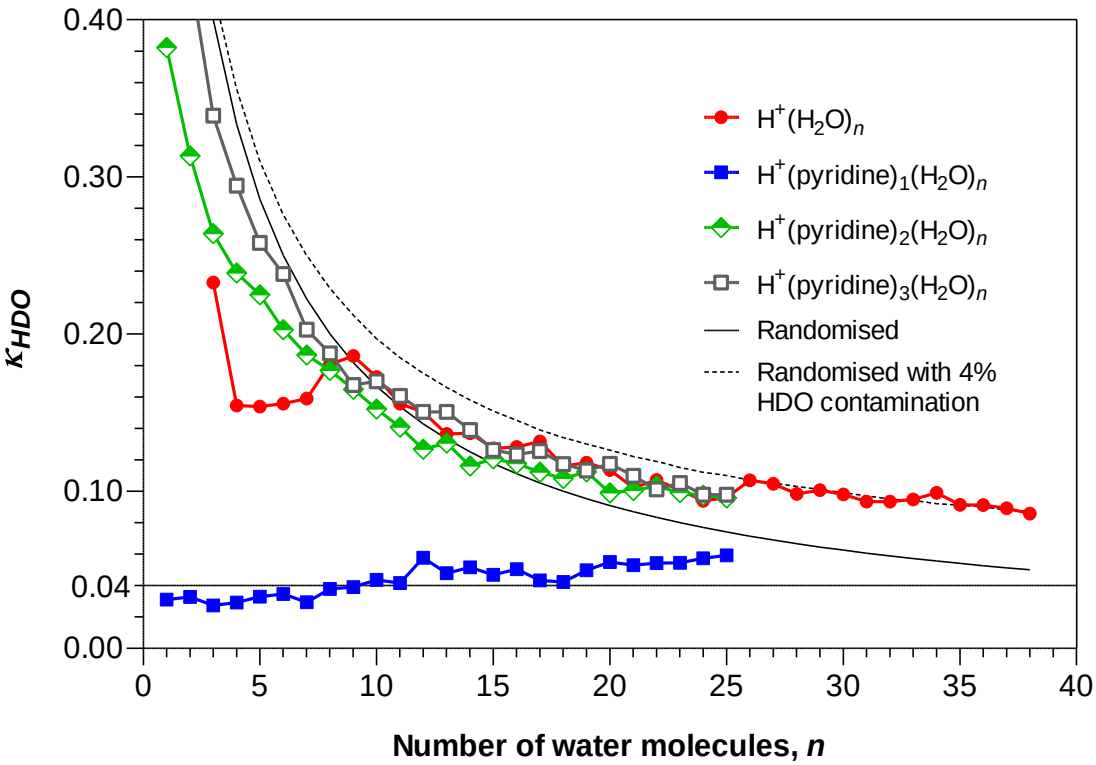

Figure 32. *κ_{HDO} for clusters $H^+(H_2O)_n$ and $H^+(pyridine)_{1-3}(H_2O)_n$ reacting with D_2O. Also included are curves representing expected κ_{HDO} values for a water cluster with a completely randomised hydrogen distribution in the case of 0% and 4% HDO contamination.*

In Figure 31, there is a marked deviation from the randomised curves for water clusters in the range n = 2–7 with lower abundance of the $H^+(H_2O)_{n-1}(HDO)$ product than expected for a cluster having complete hydrogen scrambling. A similar effect was observed by Honma and Armentrout [65] for protonated water clusters with n = 1–4 at E_{COM} = 0.04 eV. In addition, this deviation was found to increase with increasing collision energy. Honma and Armentrout showed using a simple kinetic model that this deviation is the result of a short reaction-complex lifetime compared to the rate of H/D rearrangements. For the specific reaction $H^+(H_2O)_4$ + D_2O, Honma and Armentrout reported branching ratios corresponding to κ_{HDO} = 0.26 at E_{COM} = 0.04 eV and κ_{HDO} = 0.22 at E_{LAB} = 0.6 eV (E_{COM} = 0.13 eV). This is somewhat higher than the value given in Figure 31 for the same cluster: κ_{HDO} = 0.16. However, the experiments are in qualitative agreement in that the κ_{HDO} values are significantly lower than expected. The influence of a possible HDO contamination is not mentioned by Honma and Armentrout. Apart from the deviations due to short reaction complex lifetime, there are no dramatic changes in the shape of the curves in Figure 31. Magic numbers seem to have no influence on the κ_{HDO} value for these clusters or in fact for any clusters investigated in this work. In addition, the proton mobility in the clusters indicate that the magic numbers of $H^+(H_2O)_n$ are not static entities locked in a single most stable structure.

Figure 32 shows κ_{HDO} for the clusters studied in Paper II: $H^+(H_2O)_n$ and $H^+(pyridine)_{1-3}(H_2O)_n$ at E_{COM} = 0.1 eV (E_{LAB} = 0.6 eV for clusters ≤ 80 u). Just as before, curves representing decomposition of a randomised intermediate in the case of pure D_2O collision gas (solid line) and in the case of a 4% HDO impurity in the collision gas (dashed line) are also included. The possible contamination of HDO in the D_2O collision gas is likely around 4% here as well as indicated by the experimental values. As seen in Figure 32, the pure water clusters behave in the same manner as in the experiment presented in Figure 31. We also see that the $H^+(pyridine)_1(H_2O)_n$ clusters behave in a similar manner to the $H^+(NH_3)_1(H_2O)_n$ clusters, indicating that the proton is immobile in this cluster. This comes as no surprise because the basicity of pyridine is expected to bind the proton to the nitrogen atom also in this case, even if pyridine is a weaker base than ammonia in bulk (Table 9).

The most interesting result of the above experiment is that the protonated clusters containing two or three pyridine molecules exhibits complete hydrogen scrambling in the same way that protonated water clusters do. This indicates that the hydron in $H^+(pyridine)_{2-3}(H_2O)_n$ clusters is free to move between different water molecules, thereby catalyzing H/D rearrangements in the reaction complex. Quantum chemical calculations performed on small pyridine-containing clusters (see Paper II for details) support these conclusions. The most stable cluster structures for $H^+(pyridine)_1(H_2O)_{1-6}$ show a network of water molecules, connected through a hydrogen bond to a pyridinium ion. In all cases, the most thermodynamically stable structure has the extra proton bound to the nitrogen atom. No cluster showed a local potential energy minimum for a structure with the proton located in the water network of the cluster. Thus, the quantum chemical calculations and experimental results are in agreement. Clusters containing two pyridine molecules have a typical structure where the two pyridine molecules are completely separated by the network of water molecules. Each pyridine molecule is connected to the water network of the cluster by a hydrogen bond and the most stable structures are found for protonation on one of the pyridine molecules. For n = 4–6 some local potential energy minima structures were found where the proton had been transferred to the water part of the cluster (always found in

the Eigen form, never in Zundel form). However these structures were all higher in energy (by 11.0, 16.4 and 2.4 kJmol^{-1}) than the most stable forms. Although the most stable structures found for $H^+(pyridine)_2(H_2O)_{1-6}$ all have the proton bound to one of the pyridine molecules, it seems likely that the proton can transfer to the water subsystem of the cluster with increasing ease as cluster size increases. The experiments indicate high κ_{HDO} values also for the smallest clusters with two pyridine molecules, n = 1–3, even if there are no stable structures with the proton transferred to a water molecule. It is known that protons might be transferred quickly between water molecules with pre-aligned hydrogen bonds [80]. For this reason, some transition structures for proton transfer were located based on the stable structures, and are shown in Figure 33. For a cluster consisting of two pyridine molecules, one water molecule and a proton, the barrier for transfer of protonation between the two nitrogen atoms is essentially zero. For the clusters containing 2–4 H_2O, the transfer wire between the two pyridine molecules is made up of two H_2O; additional water molecules are attached to the wire by hydrogen bonds. The Zundel structure of the transition state represents a barrier height for proton transfer that is approximately 20 kJmol^{-1} (0.21 eV).

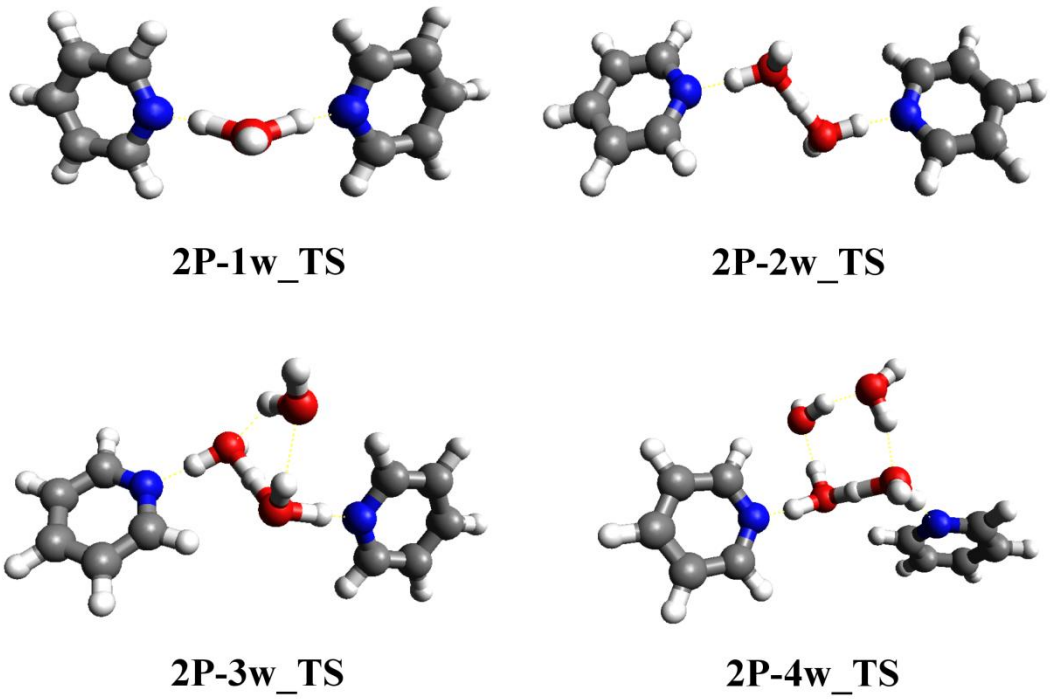

Figure 33. Transition structures (TS) for proton transfer in clusters with 2 pyridine molecules (P) and 1–4 water molecules (w).

We also see in Figure 32 that the $H^+(pyridine)_2(H_2O)_n$ and $H^+(pyridine)_3(H_2O)_n$ clusters do not deviate as strongly from the curve for a completely randomised cluster as $H^+(H_2O)_n$ does for $n \leq 7$. This is to be expected due to the presence of two pyridine molecules, which increase the number of internal degrees of freedom for a cluster

otherwise consisting of a few water molecules. Hence, the reaction complex lifetime will undoubtedly increase, allowing for more H/D rearrangements before the intermediate fragments. The effect is even more pronounced for clusters with three pyridine molecules.

Figure 34 shows the κ_{HDO} ratio measured for the bisulphate containing water cluster $HSO_4^-(H_2O)_n$ measured in Paper III. Error bars are given for every fifth cluster. The κ_{HDO} ratio is initially small, accounting for the 4% HDO contamination in the collision gas. The ratio increases steadily in the region $n = 8–13$, and then seems to follow the 4% HDO-line for statistical fragmentation of a cluster with complete hydrogen scrambling. Thus, the experiments indicate that hydrogen rearrangements are absent in small $HSO_4^-(H_2O)_n$ clusters, becoming successively more abundant as cluster size increases.

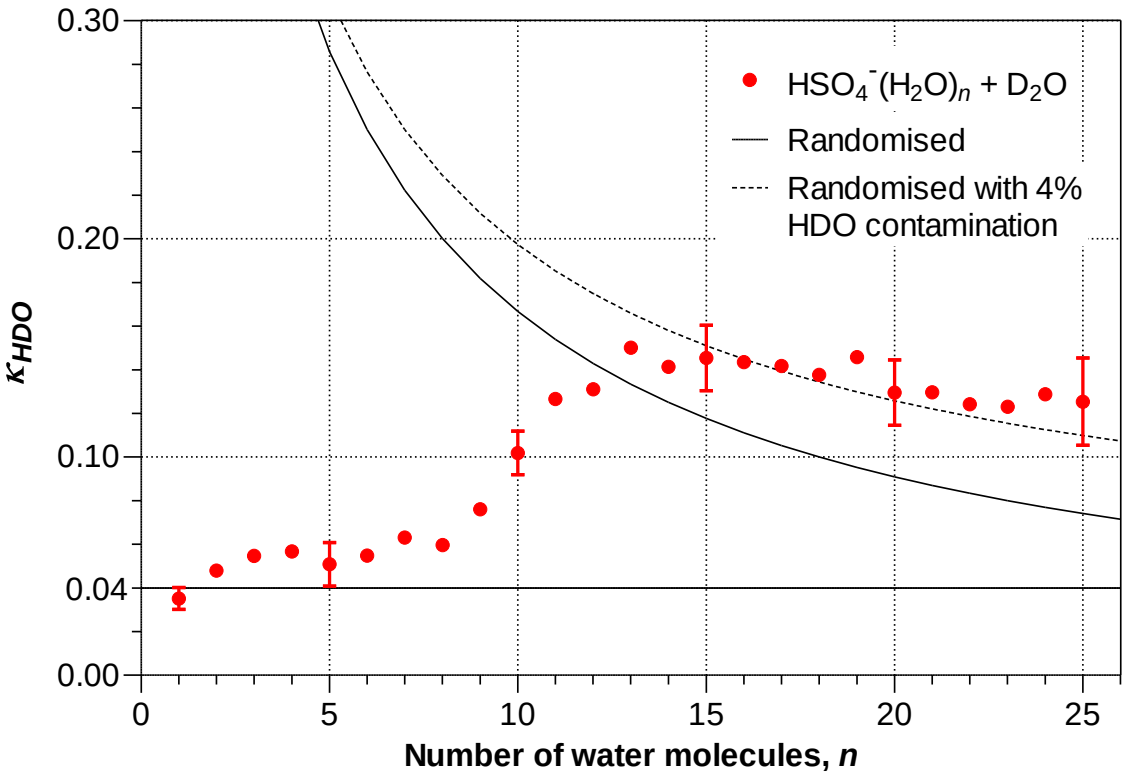

Figure 34. The κ_{HDO} ratio for the bisulphate-containing cluster $HSO_4^-(H_2O)_n$ reacting with D_2O. Error bars represent two standard deviations.

Quantum Chemical Calculations were again used for comparison (details found in Paper III). The stable structures calculated for $HSO_4^-(H_2O)_n$ with $n = 1–10$ took the shape of a hydrogen bonded network of water molecules, with the intact bisulphate ion attached by hydrogen bonds. The possibility of forming charges in the water network was investigated by two different mechanisms. In the first, $HSO_4^-(H_2O)_n \rightarrow HSO_4^-(H_2O)_{n-2}(OH^-)_1(H_3O^+)_1$, stable structures were found for the products in the case of $n = 9$ and 10, with reaction energies 72–82 kJmol^{-1}. The second mechanism involves transfer of the proton defect into the water subsystem of the cluster: $HSO_4^-(H_2O)_n \rightarrow$

$H_2SO_4(H_2O)_{n-1}(OH^-)_1$. Stable structures were found for n = 7–10 with reaction energies in the range 67–83 kJmol^{-1}. In addition to these, proton transfer along pre-aligned hydrogen bonds within the clusters was investigated, in analogy to the mechanism presented for pyridine-containing clusters. The structures are presented in Figure 35.

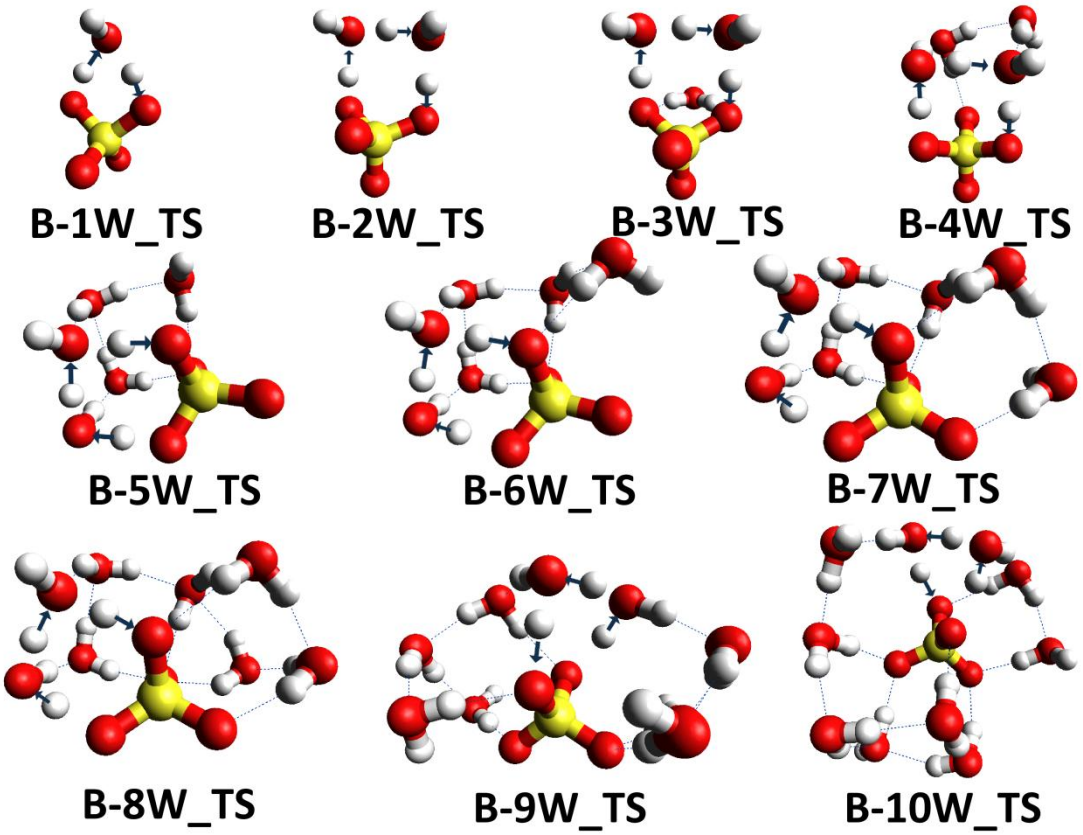

Figure 35. Transition states for proton transfer in bisulphate-containing clusters, from Paper III. Labelling: B = bisulphate, W = water. The arrows indicate the reaction coordinate.

Generally, the transfer process involves a hydrogen bond bridge of two water molecules (with the exception of n = 1) and the bisulphate molecule. The proton is abstracted from HSO_4^- and transferred to a water molecule, which in turn transfers a hydrogen atom to a second water molecule, which transfers a hydrogen atom back to the bisulphate ion. The critical energy for these transition structures (the difference between the transition structure and the most stable structure, *i.e.* the barrier height or activation energy) is found in Table 10 for n = 1–10. The energy barrier generally decreases with size, indicating that this transfer mechanism should be increasingly easy for larger clusters. In light of the trend in energy barrier for this mechanism, it seems likely that it explains the proton mobility observed in the bisulphate-containing clusters. Especially when compared with the reaction energies associated with the other two mechanisms investigated.

Table 10. Critical energy (at 0 K) for the transition structures in Figure 35, as calculated in Paper III. Values are given in kJmol^{-1} for the number of water molecules in the cluster, **n**.

n	1	2	3	4	5	6	7	8	9	10
Critical energy	43.1	49.2	60.3	39.8	39.2	34.3	31.8	30.5	15.1	17.4

Figure 36 shows the κ_{HDO} ratio as a function of reduced collision energy. As seen, the collision energy has little influence on κ_{HDO} for moderately sized water clusters below 0.21 eV in the centre-of-mass frame. Thus, there is no reason to expect that a cluster having a complete randomization of hydrogens at E_{COM} = 0.1 eV would exhibit any changes in branching ratio at thermal collision energies (0.04 eV at 298 K).

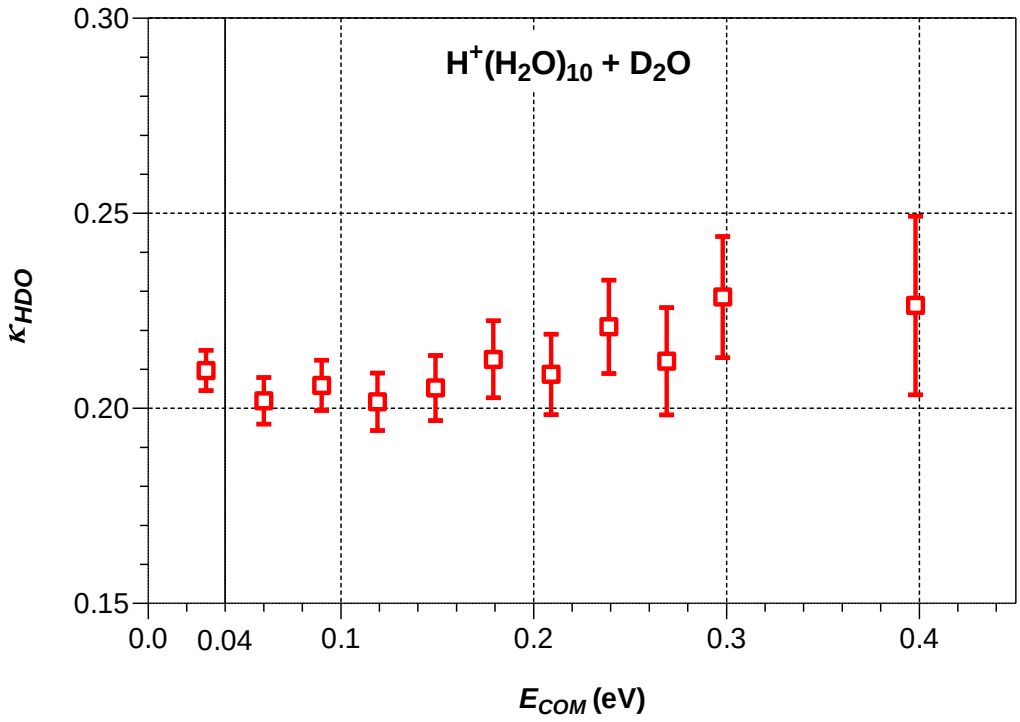

Figure 36. The κ_{HDO} ratio for the reaction $H^+(H_2O)_{10} + D_2O$ as a function of reduced collision energy. The vertical line indicates 0.04 eV, corresponding to 3/2RT at room temperature. Error bars indicate one standard deviation.

4.3 Reactions of clusters with NH_3

This section discusses the most important findings from our experiments using NH_3 as collision gas. The investigated clusters include: $H^+(H_2O)_n$, $H^+(\text{pyridine})_1(H_2O)_n$, $H^+(\text{pyridine})_2(H_2O)_n$ and $H^+(NH_3)(\text{pyridine})_1(H_2O)_n$.

4.3.1 Rate coefficient and tropospheric ion model

It is of course interesting to know the rate coefficients for cluster reactions on account of calculating growth rates and abundances of different species in the atmosphere. The modelling work by Beig and Brasseur [34] indicates that clusters containing pyridine may be the most abundant cluster ion in the lower troposphere. Beig and Brasseur proposed two reaction pathways for formation of "pyridinated cluster ions". They are given below with the X molecule representing pyridine, picoline or lutidine. Note that the original notation is somewhat ambiguous as to how many water molecules and ammonia molecules that are involved in the different reaction steps.

Mechanism A

$$H^+(H_2O)_n + mNH_3 \rightarrow H^+(NH_3)_m(H_2O)_n \quad (12)$$

$$H^+(NH_3)_m(H_2O)_n + X \rightarrow H^+(X)_1(NH_3)_{m-x}(H_2O)_{n-y} + xNH_3 + yH_2O \quad (13)$$

Mechanism B

$$H^+(H_2O)_n + X \rightarrow H^+(X)_1(H_2O)_{n-1} + xH_2O \quad (14)$$

$$H^+(X)_1(H_2O)_n + mNH_3 \rightarrow H^+(NH_3)_m(H_2O)_n + X \quad (15)$$

$$H^+(NH_3)_m(H_2O)_n + X \rightarrow H^+(X)_1(NH_3)_{m-x}(H_2O)_{n-y} + xNH_3 + yH_2O \quad (16)$$

The experimental investigation into the reactions of Paper IV sought to find the reaction rate coefficient for Reaction (15) and to identify which products forms; the reaction had not been studied before. The other reactions presented above have been studied by Viggiano *et al.* for X = pyridine [81, 82]. The relative reaction rate coefficients determined in the experiments in Paper IV are given in Figure 37 and are expressed relative to the $H^+(H_2O)_4$ cluster rate coefficient (see Section 2.3.2). They were measured at a centre-of-mass collision energy of 0.085 eV (8 $kJmol^{-1}$). Overall, the rate coefficients are lowest for the smallest clusters, increase rapidly for n = 1–4 and level off at n = 5. Water clusters generally have a higher rate coefficient in this size range. The rate coefficients for the $H^+(\text{pyridine})_1(H_2O)_n$ clusters with $n \geq 5$ can generally be found rather close to the rate coefficient of the reference cluster, which was chosen on account of there being experimentally determined values available in the literature. For the reaction $H^+(H_2O)_4 + ND_3$ Honma *et al.* [83] determined the reaction cross section to be approximately 1.5×10^{-14} cm^2, corresponding to a reaction rate coefficient of 1.6×10^{-9} cm^3s^{-1} when the velocity of the cluster in the collision cell is used. Viggiano *et al.* [81] gave the thermal rate coefficient for the reference cluster as $1.91\times10^{-9}(300/T)^{0.39}$ cm^3s^{-1}.

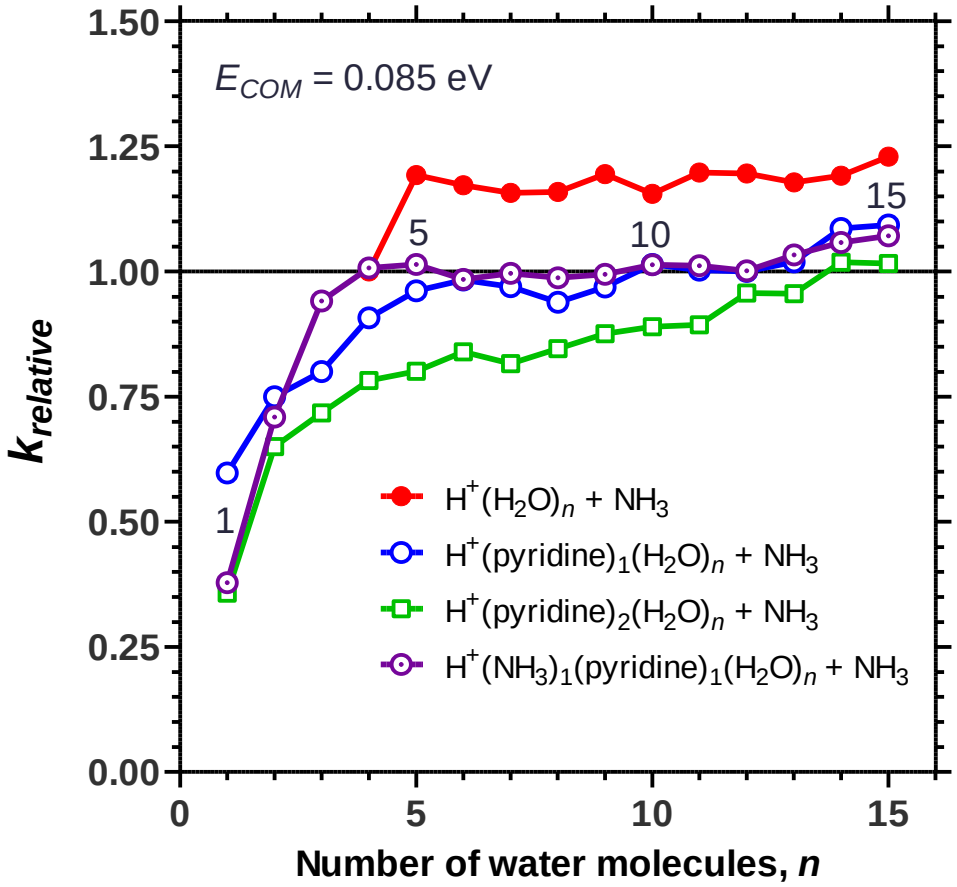

Figure 37. Relative rate coefficients for the clusters $H^+(H_2O)_n$, $H^+(pyridine)_1(H_2O)_n$, $H^+(pyridine)_2(H_2O)_n$ and $H^+(pyridine)_1(NH_3)_1(H_2O)_n$ reacting with NH_3 at 0.085 eV.

Concerning the products formed from the reactions, it was found that addition of ammonia to the clusters resulted in loss of water molecules: 2–3 H_2O in the case of pure water clusters; 1–2 H_2O for pyridine-containing clusters, and generally 2 H_2O for larger clusters. For clusters containing both pyridine and ammonia, 1–2 H_2O were lost in approximately equal amounts for all sizes $n \leq 15$. Loss of pyridine was as a rule not observed to a significant extent, neither as a product of reactions nor as spontaneous evaporation from the clusters. The maximum relative rate coefficient for loss of pyridine was estimated to 8×10^{-4} ($\pm$ 2.4×10^{-4}) with typical values near 1×10^{-4}. These correspond to reaction rates that are 7 and 50 times lower than the rate assumed by Beig and Brasseur (1×10^{-11} cm^3s^{-1}). In light of these experimental findings, a kinetic model was constructed for the abundance of cationic clusters at ground level (see details for Model A in Paper IV); the model was based on one employed by Beig and Brasseur [34], and included two significant changes. Firstly, we allowed for reactions whereby clusters containing two pyridine molecules could be formed. Secondly, Reaction (15) was excluded and replaced with the reaction $H^+(X)_1(H_2O)_n + NH_3 \rightarrow H^+(NH_3)_1(X)_1(H_2O)_n$, using the experimentally determined rate coefficient.

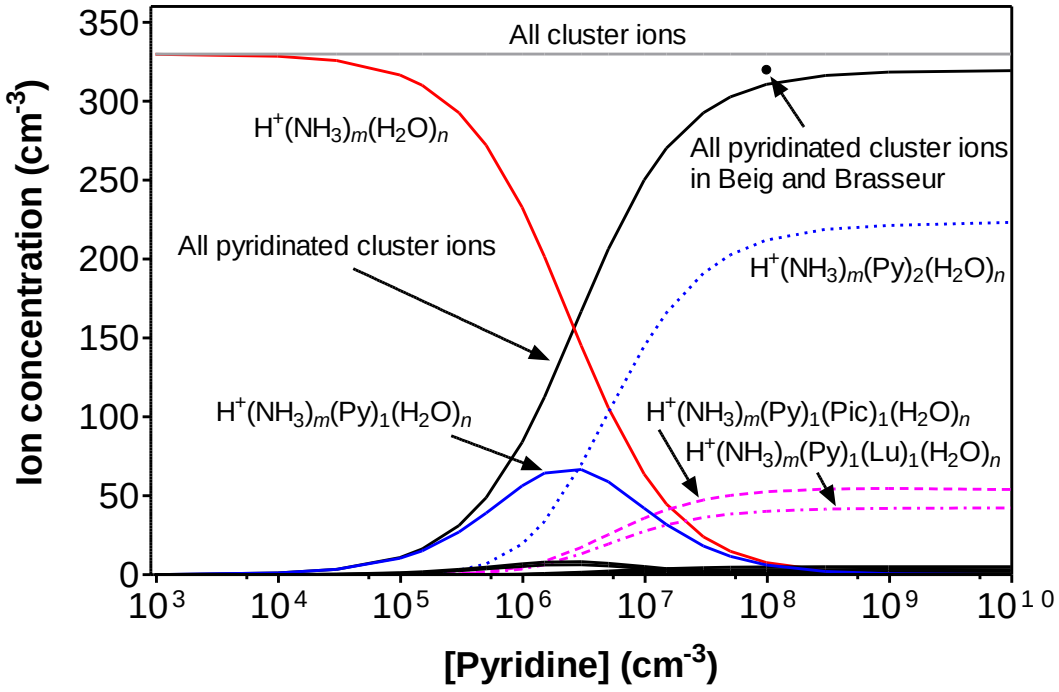

Figure 38. Results from the tropospheric cation model in Paper IV (Model A): concentration of cluster ions given as a function of the pyridine concentration. The model was calculated for ground level conditions.

The results from the model are presented in Figure 38 which shows ion concentration as a function of tropospheric pyridine concentration. The results are in good agreement with Beig and Brasseur's modelled concentration of pyridinated clusters. However, the details differ in that the pyridinated clusters in Figure 38 are dominated by clusters with two pyridine molecules for the higher half of pyridine concentrations investigated, whereas the Beig and Brasseur model only allowed for a single pyridine in a cluster. The measurements by Eisele and Eisele & Tanner put the pyridine concentration at 2.5–10 ppt = 6×10^7–2.5×10^8 cm^{-3} at 298 K [32, 43]. For these pyridine concentrations, the modelling work presented in Figure 38 suggests that clusters containing two pyridine molecules could be the dominant cluster ion in the troposphere. Our experiments have not indicated any significant degree of evaporation of pyridine from the clusters, nor have we seen any indication that clusters containing two pyridine molecules should be less stable than clusters with one pyridine.

4.3.2 Branching ratios and magic numbers

As seen from the abundance spectra and evaporation patterns (Sections 4.1.1 and 4.1.2), clusters of $H^+(NH_3)_1(\text{pyridine})_1(H_2O)_n$ have very interesting magic numbers. What makes these magic numbers interesting is they are identical to those observed for $H^+(NH_3)_1(H_2O)_n$ clusters, and arguably the same as the magic numbers for $H^+(H_2O)_n$. However, clusters containing only water molecules, pyridine and a proton do not have any magic numbers. In order to investigate this matter further, branching ratios for cluster reactions with NH_3 was determined.

Figure 39 shows the branching ratios for reactions with NH_3 for all clusters investigated: $H^+(H_2O)_n$, $H^+(\text{pyridine})_1(H_2O)_n$, $H^+(\text{pyridine})_2(H_2O)_n$ and

$H^+(NH_3)_1(pyridine)_1(H_2O)_n$ (n = 16–27). The left panels (a–d) show the branching ratios calculated for the peak intensities measured in the experiments on a logarithmic scale. Error bars for one standard deviation is included. As described in Section 2.3.5, there may be overlapping between products where the parent ion has lost several water molecules and products from clusters that have lost H_2O prior to reaction. Hence, not all intensity detected in the peaks can be said to originate from the parent ion. Using the model for peak attribution (Section 2.3.5), the intensity of each product peak that could safely be assumed to result from a parent ion reaction was calculated. New branching ratios were calculated from these intensities and are shown in the right hand side panels (e–h) of Figure 39. It is evident from Figure 39 that the magic numbers have a dramatic effect on branching ratios.

Addition of NH_3 to pure water clusters (Figure 39a, e) results in the loss of two or three water molecules for smaller n. For the $H^+(H_2O)_{22}$ cluster, formation of $H^+(NH_3)_1(H_2O)_{20}$ is clearly preferred over formation of $H^+(NH_3)_1(H_2O)_{19}$. For the n = 23 cluster loss of three H_2O is preferred, enhancing $H^+(NH_3)_1(H_2O)_{20}$ formation while $H^+(NH_3)_1(H_2O)_{21}$ formation is suppressed. Interestingly, formation of the weak magic number $H^+(NH_3)_1(H_2O)_{18}$ is not enhanced in this case. In addition, the fact that the $H^+(H_2O)_{21}$ cluster is itself a magic number does not seem to influence the branching ratios. Loss of four H_2O after the addition of NH_3 can be attributed to a parent ion reaction only when the product cluster was the magic number $H^+(NH_3)_1(H_2O)_{20}$. The branching ratios are clearly in agreement with the results obtained from the abundance spectra and the evaporation patterns for $H^+(NH_3)_1(H_2O)_n$.

In Figure 39b–c and Figure 39f–g we see the branching ratios for clusters containing one and two pyridine molecules. These two clusters have almost identical branching ratios, for $n \leq 22$ dominated by loss of two water molecules after addition of ammonia and loss of a single H_2O to a lesser extent. The $-2H_2O$ curve constitutes the entire branching ratio for $H^+(pyridine)_{1-2}(H_2O)_{20}$ + NH_3, forming the $H^+(NH_3)_1(pyridine)_{1-2}(H_2O)_{18}$ cluster. This is followed by a slight decrease at n = 21 and then an increase again at n = 22 (forming $H^+(NH_3)_1(pyridine)_{1-2}(H_2O)_{20}$). However, at this point, the $-H_2O$ products have disappeared and $-3H_2O$ products begin to appear. The latter is the dominant product for the reaction $H^+(pyridine)_{1-2}(H_2O)_{23}$ + NH_3, before the loss of two water molecules again become the major product at n = 24, indicating a weak magic number for $H^+(NH_3)_1(pyridine)_{1-2}(H_2O)_{22}$ (*cf.* Figure 24).

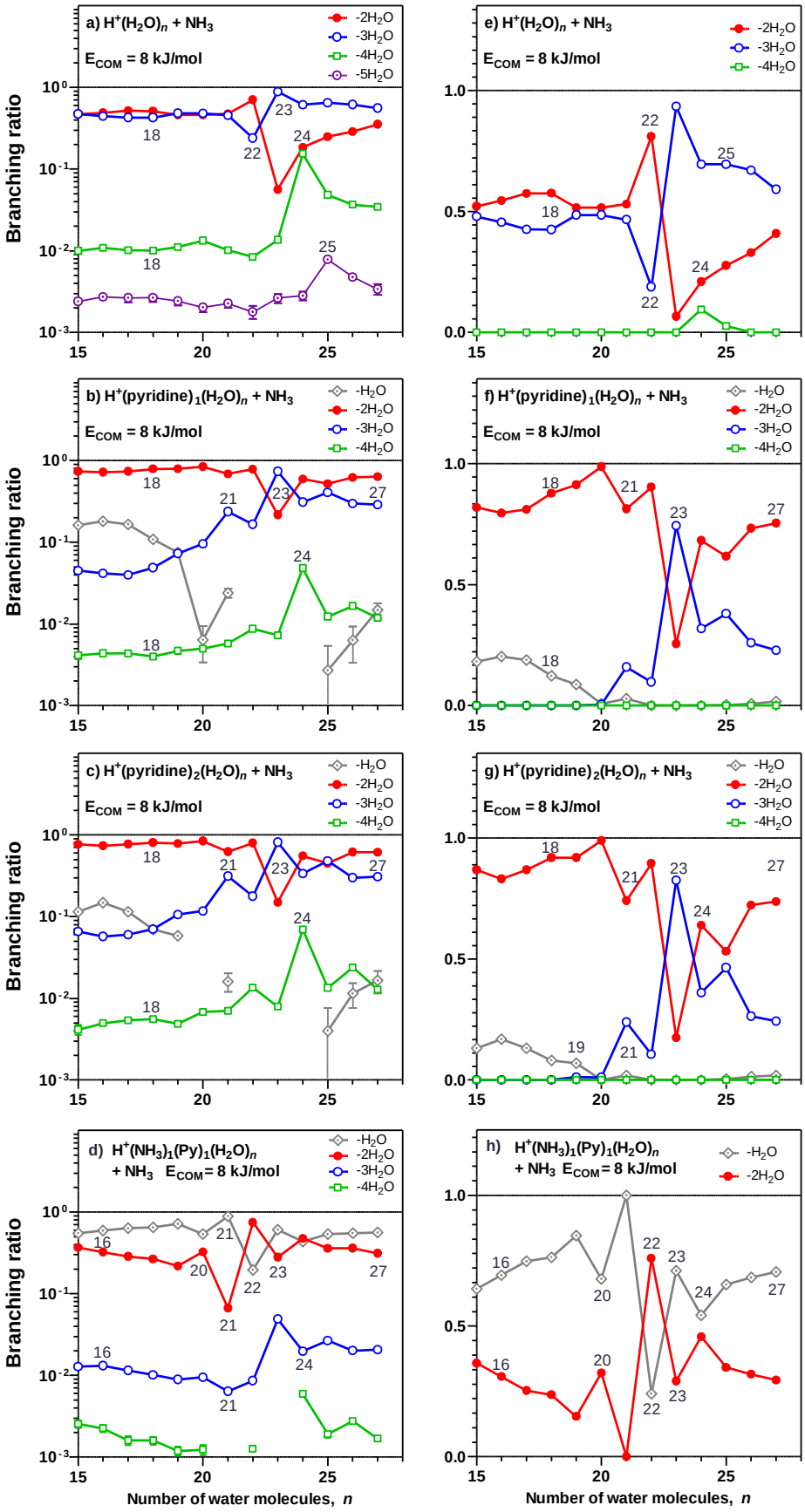

Figure 39. Branching ratios for clusters reacting with NH_3. Panels a–d show the values for peak intensities as measured in the experiments; error bars are shown. Panels e–h show the branching ratios for the peak intensity attributed to the parent ion.

In contrast to the previous clusters for which the loss of two or three water molecules are the typical products, the reaction $H^+(NH_3)_1(pyridine)_1(H_2O)_n$ + NH_3 is characterised by the loss of one or two water molecules. The trends in branching ratios are the same as for the previous clusters, with enhanced branching ratio for the reaction channel forming clusters containing 18, 20 and 22 water molecules, while the other reaction channel is suppressed. However, in this case, the magic clusters all contain two NH_3. As noted above, when comparing $H^+(H_2O)_n$ and $H^+(NH_3)_1(H_2O)_n$ clusters, an ammonia molecule takes the place of a water molecule when counting the number of molecules in the magic clusters. This is likely a consequence of both molecules having the ability to form multiple hydrogen bonds and being similar in size. The results of Shinohara *et al.* [71, 72] indicate that this is only true for the first ammonia molecule as the magic clusters with more than one ammonia all contain 20 water molecules. Hence, it is reasonable that the magic numbers found for $H^+(NH_3)_2(pyridine)_1(H_2O)_n$ are the same as those found for $H^+(NH_3)_1(pyridine)_1(H_2O)_n$.

For clusters consisting of water and pyridine, quantum chemical calculations indicate that in the most stable structures, the proton is attached to the nitrogen of a pyridine molecule. The pyridinium ion is attached to a separate network of water molecules by a hydrogen bond to the charge carrying proton (Section 4.2.3), *i.e.* a structure like PyH^+--$(H2O)_n$ where Py = pyridine. It is possible that the removal of the proton from the water network is responsible for the loss of magic numbers in these clusters. In a $H^+(NH_3)_1(pyridine)_1(H_2O)_n$ cluster, the ammonia molecule is likely found as part of the hydrogen bonded network of water molecules, owing to the similarity of NH_3 and H_2O. There are studies that suggest that the ammonium ion in a $NH_4^+(H_2O)_{20}$ cluster is found at the surface, with a N–H bond dangling free on the clusters outside [84, 85]; there are also studies that indicate that the ammonium ion is found at the cluster centre [86, 87]. Regardless, the addition of another basic molecule is likely to affect the energetics and structure of the cluster. Protonation in the form of an ammonium core ion is expected also for $H^+(NH_3)_1(pyridine)_1(H_2O)_n$ clusters, in light of the higher proton affinity and basicity of ammonia (Table 9). A plausible structure for $H^+(NH_3)_1(pyridine)_1(H_2O)_n$ is a hydrogen bonded network containing H_2O and NH_4^+, with the pyridine molecule attached to a dangling hydrogen, likely one from the ammonium ion. This would also explain the reoccurrence of magic numbers; the proton is now back in the hydrogen bonded network. If the ammonium ion only has one dangling N–H bond, a second pyridine molecule must bond to a water molecule instead.

4.4 Collision induced dissociation of $H^+(NH_3)_m(H_2O)_n$

In the Separator 1 instrument, it was possible to obtain cluster ions containing several ammonia molecules (up to six in this case). While this might be possible also in the QTOF 2 instrument, it is impractical on account of the highly concentrated ammonia solutions needed.

The formation of $H^+(NH_3)_m(H_2O)_n$ clusters from the ions produced by the corona discharge tends to favour NH_3 over H_2O for the first few molecules. The clusters in the mass spectra consisted of only ammonia molecules up to $H^+(NH_3)_5$. However, heavier clusters all contained at least one water molecule, with $H^+(NH_3)_4(H_2O)_1$ being the first mixed cluster at m/z = 87. No $H^+(NH_3)_6$ clusters were found in agreement with the results of Shinohara *et al.* [72]. When water molecules began to appear in the clusters, the spectrum become dominated by three types of clusters: $H^+(NH_3)_4(H_2O)_n$, $H^+(NH_3)_5(H_2O)_n$ and $H^+(NH_3)_6(H_2O)_n$. Some of these clusters were collided with air in

order to investigate collision induced dissociation (CID). Figure 40 shows the ratio of loss of H_2O to loss of NH_3 for clusters with 4–6 ammonia molecules and 1–6 water molecules (note the different scales on the ordinate).

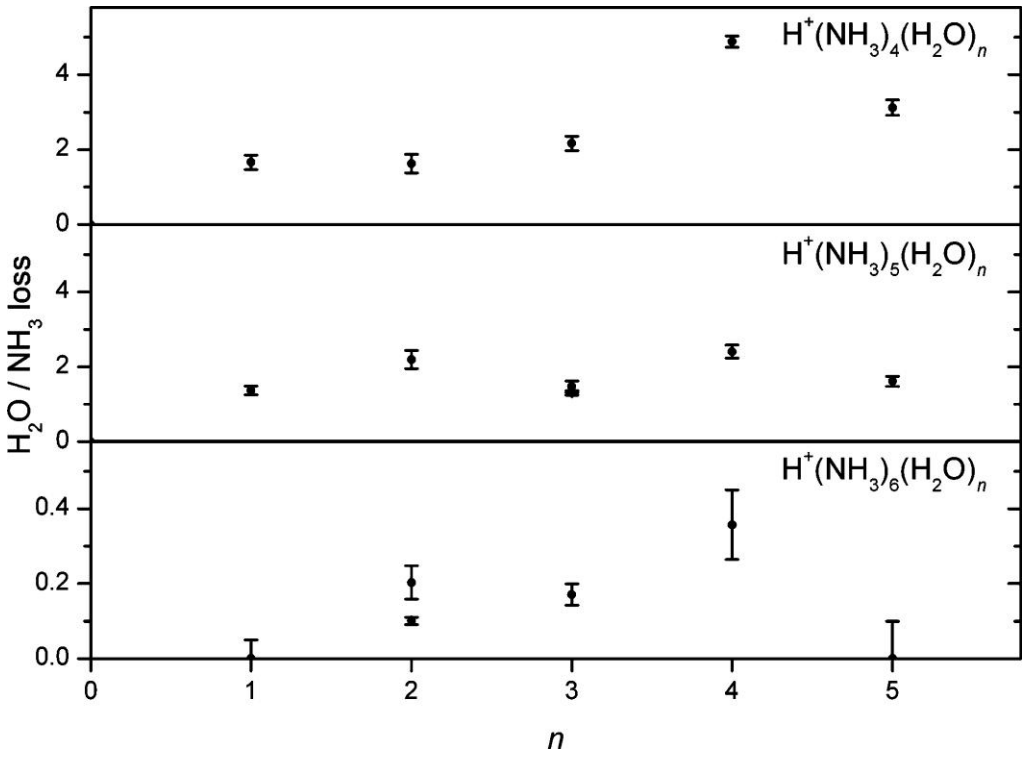

Figure 40. Loss of H_2O relative loss of NH_3 for collision induced dissociation of $H^+(NH_3)_m(H_2O)_n$ with* m *= 4–6 and* n *= 1–6. From Paper VI.

While clusters containing four or five ammonia molecules prefer to lose a water molecule, loss from the $H^+(NH_3)_6(H_2O)_n$ clusters are primarily in the form of NH_3. This tendency is observed for larger clusters as well. For example, $H^+(NH_3)_6(H_2O)_{20}$ preferred to lose an ammonia while $H^+(NH_3)_5(H_2O)_{21}$ preferred to lose a water molecule with both favouring the formation of the magic number $H^+(NH_3)_5(H_2O)_{20}$ cluster (see [72]). It would seem from the CID experiments that clusters prefer to have no more than 5 ammonia molecules, since $H^+(NH_3)_6$ clusters were not observed, $H^+(NH_3)_6(H_2O)_n$ clusters prefer to lose NH_3 and mixed clusters having 5 ammonia molecules prefer to lose H_2O. This agrees with the supposition of a central NH_4^+ surrounded by four NH_3 in a first solvation shell with additional H_2O and NH_3 molecules found in a second solvation shell [88, 89]. Quantum chemical calculations performed in connection to the experiments suggest a somewhat more complicated picture.

In the most stable calculated structures, clusters having 5–6 NH_3 and 1–3 H_2O were found to have at least one water molecule in the inner solvation shell surrounding the NH_4^+ core ion. For clusters with one H_2O, the water molecule was always found in the first solvation shell, with the fifth NH_3 molecule banished to the outer solvation shell. Furthermore, the formation of the second solvation shell begins with addition of the fifth ammonia molecule to the water molecule in the inner shell. Clusters with two H_2O

had one or two water molecules in the first solvation shell, dependent upon whether the enthalpy or Gibbs free energy was minimised. Likewise, clusters containing three H_2O had two or three water molecules in the first solvation shell, dependent upon if minimization was done for the enthalpy or the Gibbs free energy, respectively. Nevertheless, calculations on the enthalpy of evaporation clearly indicates that clusters having one or two water molecules prefer evaporation of one of those if the number of ammonia molecules in the cluster is ≤ 5, while they prefer to lose an ammonia molecule should the number of those be six or seven.

Thus, for $H^+(NH_3)_5(H_2O)_1$, the quantum chemical calculations suggest a minimum energy structure that may be somewhat counter-intuitive in that the water molecule is found in the first solvation shell; in addition, the calculations suggest that the water molecule is the first molecule to leave the cluster upon fragmentation, in agreement with the experiments (Figure 41). The evaporation process is therefore likely associated with an intra-cluster ligand exchange or rearrangement, indicating again that clusters should be thought of as dynamic, changing entities.

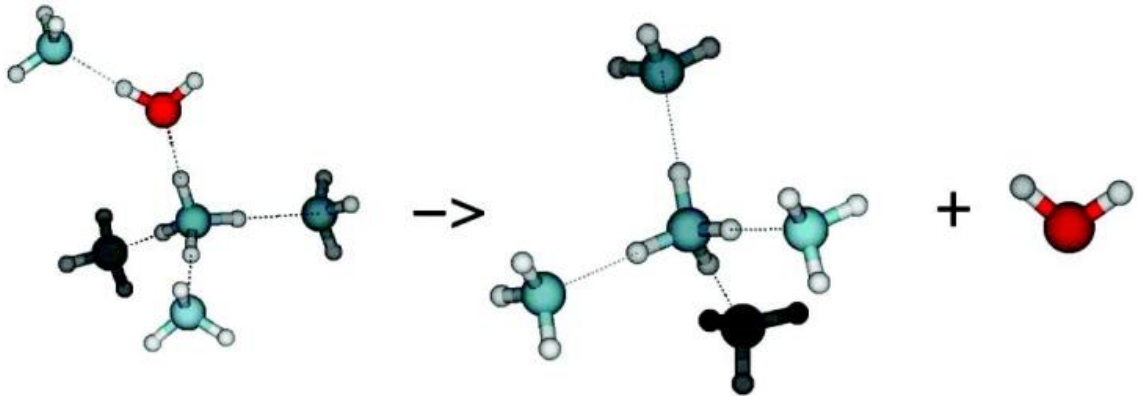

Figure 41. Evaporation of H_2O from the most stable structure of the $H^+(NH_3)_5(H_2O)_1$ cluster.

5 Conclusions

Magic numbers found for clusters $H^+(H_2O)_n$ and $H^+(NH_3)_1(H_2O)_n$ are in agreement with previous studies [59, 71, 72]. Apart from increased abundance of species like $H^+(pyridine)_2$ and $H^+(pyridine)_3(H_2O)_1$, no clear magic numbers were found for clusters having between one and three pyridine molecules, a proton and water molecules (25 or less). However, magic numbers were found for clusters of the type $H^+(NH_3)_1(pyridine)_m(H_2O)_n$ with $m = 1$ or 2 and for clusters of the type $H^+(NH_3)_2(pyridine)_1(H_2O)_n$. Furthermore, these magic numbers coincide with the magic numbers for $H^+(NH_3)_1(H_2O)_n$, found for $n = 18$, 20 and 27. While the reason is unclear, a possible explanation for the difference in terms of magic numbers between $H^+(pyridine)_m(H_2O)_n$ and $H^+(NH_3)_1(pyridine)_m(H_2O)_n$ is that the former has the proton attached to the pyridine molecule—outside the hydrogen bonded water network; the latter likely has a NH_4^+ ion situated in the water subsystem of the cluster, in analogy with $H^+(H_2O)_n$ and $H^+(NH_3)_1(H_2O)_n$ clusters.

It was found that magic numbers did not influence the reaction cross section for any of the investigated clusters reacting with D_2O or NH_3 ($n = 1$–15); however, the magic numbers did influence the degree to which clusters lost additional water molecules after fragmentation of the reaction intermediate. Results from cross section measurements were used to improve an existing kinetic model on atmospheric ion composition [34]. The improved model indicates that the positive cluster-ion spectrum at ground level may be dominated by clusters containing more than one pyridine molecule, in addition to water and ammonia.

Reactions of water-containing clusters with D_2O show to what extent the clusters are able to rearrange their hydrogens between different water molecules (and other molecules). This hydrogen scrambling process was found to occur for pure protonated water clusters, in agreement with previous studies [65, 66], while it was absent for $H^+(NH_3)_1(H_2O)_n$ clusters; a consequence of the formation of a NH_4^+ core ion in the latter. Hydrogen scrambling was also absent in the $H^+(pyridine)_1(H_2O)_n$ clusters, for reasons inherit to inclusion of a basic molecule: bonding the proton to a single molecule. However, addition of a second or even third pyridine molecule results in a mobile proton once again, evident from the emission of HDO from the reaction complex to an extent corresponding to a completely statistical composition of the leaving water molecule. Quantum chemical calculations suggest that this is in part due to existence of stable structures with a hydroxonium ion, in part due to a relay mechanism whereby the site of protonation is transferred from one pyridine to the other along a pre-aligned wire of hydrogen bonds. A similar mechanism was also suggested as the explanation for the proton scrambling taking place in bisulphate-containing clusters, $HSO_4^+(H_2O)_n$. Although in this case, the protonation transfer was between different oxygen atoms of the bisulphate ion. The bisulphate/water clusters show a transition region for $n = 8$–12, where they go from having no hydrogen scrambling to having full hydrogen scrambling. This coincides with changes in the energy barrier associated with the proton transfer mechanism, which drops from about 30 $kJmol^{-1}$ at $n = 8$ to around 16 $kJmol^{-1}$ for $n = 9$ and 10. Other mechanisms were also investigated for this cluster, namely, autoprotolysis of water in the cluster (bisulphate ion intact) and abstraction of hydrogen from water by the bisulphate ion. However, the reaction energies for these processes were approximately 70 $kJmol^{-1}$. Magic numbers did not influence the degree of hydrogen scrambling for any clusters in these experiments.

6 Outlook

Given the very interesting difference in inter-cluster dynamics between clusters with a single pyridine molecule and clusters with two or three, and the parallel drawn from the former to clusters having an ammonia molecule, the question naturally arises whether a cluster with two or more ammonia molecules will show H/D exchange reactions or not. This, and the D_2O reactions of clusters having both pyridine and ammonia molecules is the subject of experimental and computational investigations currently under way. In addition, initial experiments have been performed on the reactions between D_2O and cationic water clusters containing alkali metals. The reactions of anionic clusters $OH^-(H_2O)_n$ and $Cl^-(H_2O)_n$ with D_2O will also be studied.

The role of molecular clusters in the scope of atmospheric chemistry, particle formation and ultimately impact on the global radiation budget is to a large extent associated with uncertainties, and will likely be subjected to substantial scientific attention during the coming years. In addition, there is much to be learned about the clusters themselves: structure, magic numbers, reactions and thermochemistry. No doubt new efforts and discoveries will continue to be made in these research areas.

7 Acknowledgements

The author wishes to express his gratitude to the Swedish Research Council and to the Nanoparticle in Interactive Environments platform at the Faculty of Science at University of Gothenburg for funding this work.

The author is also grateful for travel grants that have been awarded from the following funds and foundations: Göteborgs Universitets Jubileumsfond, Filosofiska Fakulteternas gemensamma donationsnämnd (Göteborgs Universitet), Barbro Bryngelssons minnesfond, Lundgrenska Stiftelserna, Knut och Alice Wallenbergs stiftelse, Stiftelsen Lars Hiertas Minne.

On a more personal note, I would first of all like to thank my head supervisor Patrik Andersson. When I started working towards my Ph.D., a lot of people told me that I was very fortunate to get such a helpful, knowing and patient person as supervisor. They were right. I would also like to thank my assistant supervisor Klavs Hansen, from whom I have learned many a useful thing. To my examiner Jan Pettersson: your encouragement and concern is much appreciated, thank you. To Einar Uggerud and the other people at University of Oslo, thank you for our excellent collaboration and for your hospitality. Finally, to everyone else, family and friends, people at the atmospheric science group and in the Nanoparticle platform: thank you for your support, encouragement, and for good times.

8 Scientific Ancestors

This is the scientific genealogy of Mauritz Johan Ryding: a lineage of advisors/mentors and their students (dashed lines indicate scientific influences that are not of the advisor–doctoral student type). These records build to a great degree on earlier efforts by Jan B. C. Pettersson, who in addition to being a scientist is also an amateur genealogist. The records have been supplemented by investigations by the author, primarily using online sources[d]. The author makes no claim of these records being complete or devoid of error. In addition, the facts and trivia given herein are in no way meant to be representative of the lives or scientific work of the individuals in question; they are merely things that the author found interesting.

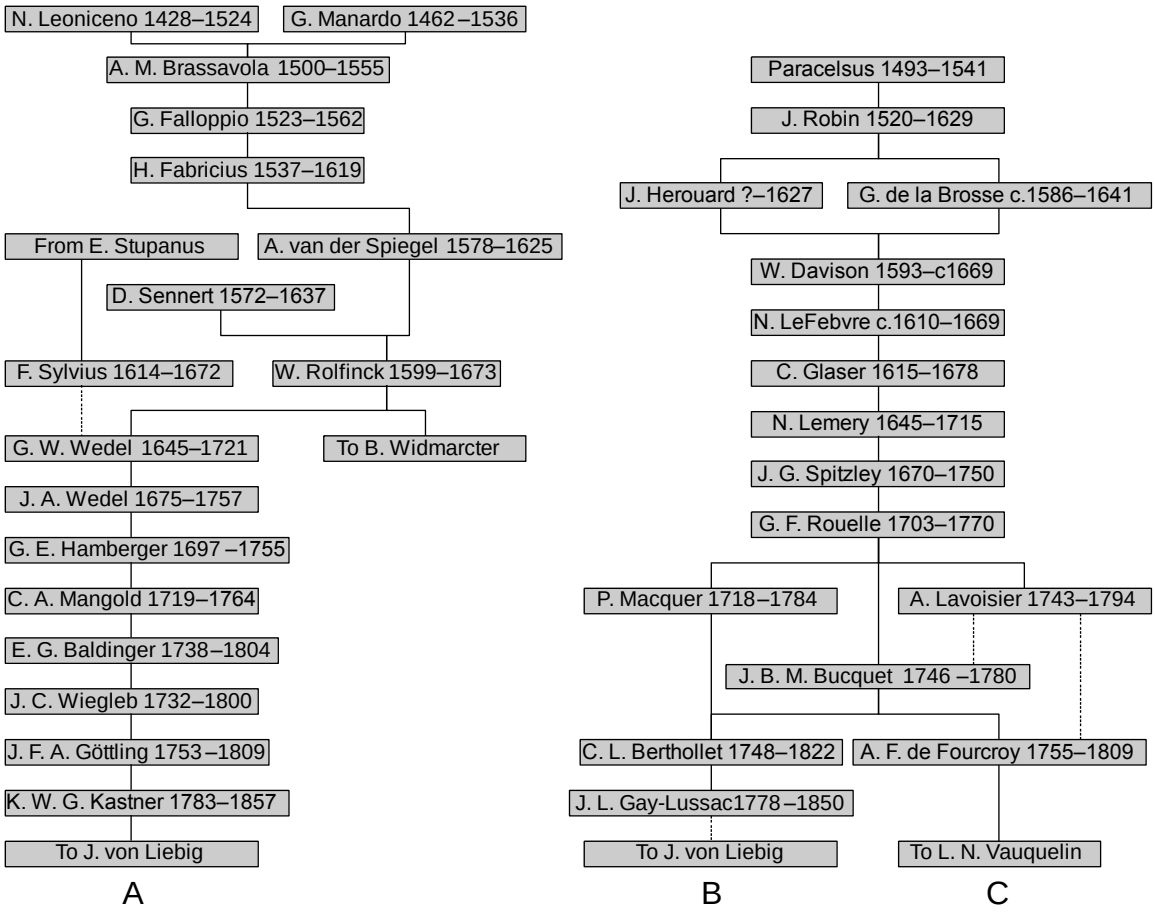

[d] Mathematics Genealogy Project (http://genealogy.impa.br/index.php)
Wikipedia (http://www.wikipedia.org)

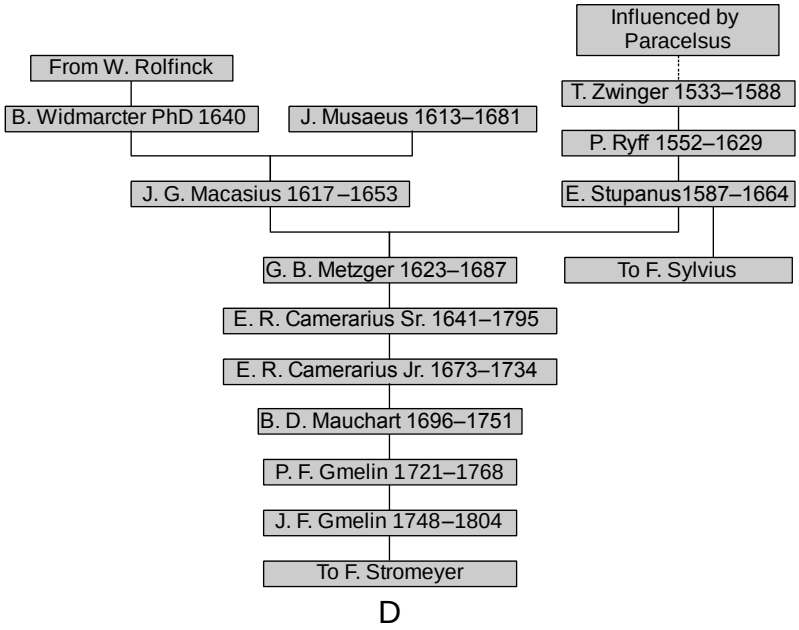
Influenced by Paracelsus
From W. Rolfinck
T. Zwinger 1533–1588
B. Widmarcter PhD 1640
J. Musaeus 1613–1681
P. Ryff 1552–1629
J. G. Macasius 1617–1653
E. Stupanus1587–1664
G. B. Metzger 1623–1687
To F. Sylvius
E. R. Camerarius Sr. 1641–1795
E. R. Camerarius Jr. 1673–1734
B. D. Mauchart 1696–1751
P. F. Gmelin 1721–1768
J. F. Gmelin 1748–1804
To F. Stromeyer
D

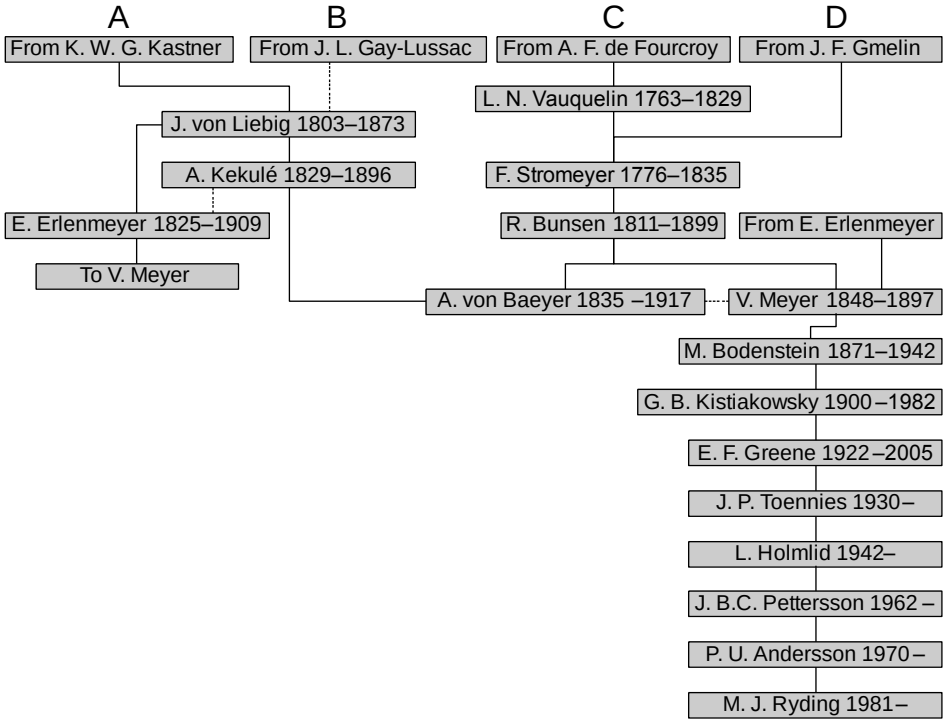
A
B
C
D
From K. W. G. Kastner
From J. L. Gay-Lussac
From A. F. de Fourcroy
From J. F. Gmelin
L. N. Vauquelin 1763–1829
J. von Liebig 1803–1873
A. Kekulé 1829–1896
F. Stromeyer 1776–1835
E. Erlenmeyer 1825–1909
R. Bunsen 1811–1899
From E. Erlenmeyer
To V. Meyer
A. von Baeyer 1835 –1917
V. Meyer 1848–1897
M. Bodenstein 1871–1942
G. B. Kistiakowsky 1900 –1982
E. F. Greene 1922 –2005
J. P. Toennies 1930–
L. Holmlid 1942–
J. B.C. Pettersson 1962 –
P. U. Andersson 1970 –
M. J. Ryding 1981–

Adolf von Baeyer, 1835–1917. German chemist. Doctorate in 1858. Nobel Prize in Chemistry 1905.

Antonio Muso Brassavola, 1500–1555. Italian physician. Consulting physician of Kings Francis I, Charles V, Henry VIII and Popes Paul III, Leo X, Clement VIII and Julius III. Performed the first successful tracheotomy.

Guy de la Brosse, c.1586–1641. French physician and botanist. Physician to King Louis XIII of France.

Robert Bunsen, 1811–1899. German chemist, Ph.D. in 1831. Discovered caesium and rubidium together with Gustav Kirchhoff. Developed the Bunsen burner together with Peter Desaga.

Emil Erlenmeyer, 1825–1909. German chemist. Inventor of the Erlenmeyer flask.

Gabriele Fallopio, 1523–1562. One of the most important physicians and anatomists of the sixteenth century. Advocated the use of condoms, and initiated what may have been the first clinical trial of the device.

Antoine François, comte de Fourcroy, 1755–1809. French chemist. Doctor of Medicine. Co-discovered Iridium. Elected a foreign member of the Royal Swedish Academy of Sciences in 1801.

George Bogdan Kistiakowsky, 1900–1982. Ukrainian–American, PhD in Physical chemistry 1925. Expert on the fundamentals of explosives. Joined the Manhattan Project in 1944 and lead the group that created the detonation device for the first atomic bomb. Became Science Advisor to President Eisenhower in 1959. Worked intensively for nuclear disarmament from the late sixties until his death.

Antoine-Laurent de Lavoisier, 1743–1794. French nobleman and scientist. Father of modern chemistry. Discovered and named hydrogen and oxygen. Performed some of the first truly quantitative chemical experiments. Helped construct the metric system, put together the first extensive list of elements and helped to reform chemical nomenclature (together with Claude-Louis Berthollet, Antoine Fourcroy and Guyton de Morveau). Guillotined.

Niccolò Leoniceno, 1428–1524. Italian physician and humanist. Wrote the first scientific paper on syphilis.

Justus von Liebig, 1803–1873. German chemist. Regarded as one of the greatest chemistry teachers of all time, and the "father of the fertilizer industry".

Pierre Joseph Macquer, 1718–1784. Wrote Dictionnaire de chymie (1766). Elected a foreign member of the Royal Swedish Academy of Sciences in 1768.

Viktor Meyer, 1848–1897. German chemist. Loved poetry. Suicide by cyanide.

Paracelsus, 1493–1541. Real name: Philippus Aureolus heophrastus Bombastus von Hohenheim. Swiss alchemist, physician, astrologer and occultist. Credited for giving zinc its name. Regarded as the first systematic botanist. Sometimes referred to as the father of toxicology, as he concluded that "the dose makes the poison".

Guillaume François Rouelle, 1703–1770. Introduced the concept of a base. Elected a foreign member of the Royal Swedish Academy of Sciences in 1749.

Daniel Sennert, 1572–1637. German physician, alchemist and chemist. Made contributions to the development of an early version of atomic theory.

Friedrich Stromeyer, 1776–1835. German chemist, Doctor of Medicine in 1800. Discovered Cadmium.

Franciscus Sylvius, 1614–1672. Dutch physician and scientist. In 1669 Sylvius founded the first academic chemical laboratory. Credited with the invention of jenever.

Louis Nicolas Vauquelin, 1763–1829. Discoverer of beryllium and chromium. Elected a foreign member of the Royal Swedish Academy of Sciences in 1816. Co-discovered the first amino acid, in an asparagus.

9 References

1. IPCC, *Summary for Policymakers*, in *Climate Change 2007: The Physical Science Basis. Contribution of Working Group I to the Fourth Assessment Report of the Intergovernmental Panel on Climate Change*. Solomon, S., Qin, D., Manning, M., Chen, Z., Marquis, M., Averyt, K.B., Tignor, M., and Miller, H.L., Editors. 2007, Cambridge University Press: Cambridge, United Kingdom and New York, NY, USA.
2. Nordling, C. and Österman, J., *T – 9.4 Astronomical Quantities*, in *Physics Handbook for Science and Engineering*. 6th ed. 1999, Studentlitteratur: Lund, Sweden.
3. Brasseur, G. and Solomon, S., *Aeronomy of the Middle Atmosphere: Chemistry and Physics of the Stratosphere and Mesosphere.* 2nd ed. 1986, D. Reidel publishing company: Dordrecht, Netherlands.
4. Wayne, R.P., *Chemistry of Atmospheres*. 3rd ed. 2000, Oxford University Press: Cambridge, United Kingdom and New York, NY, USA.
5. Lutgens, F.K. and Tarbuck, E.J., *The Atmosphere: An Introduction to Meteorology*. 9th ed. 2003, Prentice Hall: New jersey, USA.
6. Hinds, W.C., *Aerosol Technology*. 2nd ed. 1999, John Wiley & Sons, Inc.: New York, USA.
7. Finlayson-Pitts, B.J. and Pitts, J.N., *Chemistry of the Upper and Lower Atmosphere*. 2000, Academic Press: San Diego, USA.
8. Whitby, K.T., Barsic, N.J., Husar, R.B., and Liu, B.Y.H., *Minnesota Aerosol-Analyzing System Used in Los-Angeles Smog Project.* Journal of Colloid and Interface Science, 1972. **39**(1): p. 136-164.
9. Whitby, K.T., Liu, B.Y.H., and Husar, R.B., *Aerosol Size Distribution of Los-Angeles Smog.* Journal of Colloid and Interface Science, 1972. **39**(1): p. 177-204.
10. Husar, R.B., Liu, B.Y.H., and Whitby, K.T., *Physical Mechanisms Governing Dynamics of Los-Angeles Smog Aerosol.* Journal of Colloid and Interface Science, 1972. **39**(1): p. 211-224.
11. Kurten, T., Loukonen, V., Vehkamaki, H., and Kulmala, M., *Amines are likely to enhance neutral and ion-induced sulfuric acid-water nucleation in the atmosphere more effectively than ammonia.* Atmospheric Chemistry and Physics, 2008. **8**(14): p. 4095-4103.
12. Pueschel, R.F., *Stratospheric aerosols: Formation, properties, effects.* Journal of Aerosol Science, 1996. **27**(3): p. 383-402.
13. Forster, P., Ramaswamy, V., Artaxo, P., Berntsen, T., Betts, R., Fahey, D.W., Haywood, J., Lean, J., Lowe, D.C., Myhre, G., Nganga, J., Prinn, R., Raga, G., Schulz, M., and Van Dorland, R., *Changes in Atmospheric Constituents and in Radiative Forcing.*, in *Climate Change 2007: The Physical Science Basis. Contribution of Working Group I to the Fourth Assessment Report of the Intergovernmental Panel on Climate Change*. Solomon, S., Qin, D., Manning, M., Chen, Z., Marquis, M., Averyt, K.B., Tignor, M., and Miller, H.L., Editors. 2007, Cambridge University Press: Cambridge, United Kingdom and New York, NY, USA.
14. Hughes, L.S., Cass, G.R., Gone, J., Ames, M., and Olmez, I., *Physical and chemical characterization of atmospheric ultrafine particles in the Los Angeles area.* Environmental Science & Technology, 1998. **32**(9): p. 1153-1161.

15. Colbeck, I. and Lazaridis, M., *Aerosols and environmental pollution.* Naturwissenschaften, 2010. **97**(2): p. 117-131.
16. Pope, C.A., Ezzati, M., and Dockery, D.W., *Fine-Particulate Air Pollution and Life Expectancy in the United States.* New England Journal of Medicine, 2009. **360**(4): p. 376-386.
17. Kulmala, M., *How particles nucleate and grow.* Science, 2003. **302**(5647): p. 1000-1001.
18. Kulmala, M. and Kerminen, V.M., *On the formation and growth of atmospheric nanoparticles.* Atmospheric Research, 2008. **90**(2-4): p. 132-150.
19. Kirkby, J., Curtius, J., Almeida, J., Dunne, E., Duplissy, J., Ehrhart, S., Franchin, A., Gagne, S., Ickes, L., Kurten, A., Kupc, A., Metzger, A., Riccobono, F., Rondo, L., Schobesberger, S., Tsagkogeorgas, G., Wimmer, D., Amorim, A., Bianchi, F., Breitenlechner, M., David, A., Dommen, J., Downard, A., Ehn, M., Flagan, R.C., Haider, S., Hansel, A., Hauser, D., Jud, W., Junninen, H., Kreissl, F., Kvashin, A., Laaksonen, A., Lehtipalo, K., Lima, J., Lovejoy, E.R., Makhmutov, V., Mathot, S., Mikkila, J., Minginette, P., Mogo, S., Nieminen, T., Onnela, A., Pereira, P., Petaja, T., Schnitzhofer, R., Seinfeld, J.H., Sipila, M., Stozhkov, Y., Stratmann, F., Tome, A., Vanhanen, J., Viisanen, Y., Vrtala, A., Wagner, P.E., Walther, H., Weingartner, E., Wex, H., Winkler, P.M., Carslaw, K.S., Worsnop, D.R., Baltensperger, U., and Kulmala, M., *Role of sulphuric acid, ammonia and galactic cosmic rays in atmospheric aerosol nucleation.* Nature, 2011. **476**(7361): p. 429-U77.
20. Kulmala, M., Riipinen, I., Sipila, M., Manninen, H.E., Petaja, T., Junninen, H., Dal Maso, M., Mordas, G., Mirme, A., Vana, M., Hirsikko, A., Laakso, L., Harrison, R.M., Hanson, I., Leung, C., Lehtinen, K.E.J., and Kerminen, V.M., *Toward direct measurement of atmospheric nucleation.* Science, 2007. **318**(5847): p. 89-92.
21. Hirsikko, A., Nieminen, T., Gagne, S., Lehtipalo, K., Manninen, H.E., Ehn, M., Horrak, U., Kerminen, V.M., Laakso, L., McMurry, P.H., Mirme, A., Mirme, S., Petaja, T., Tammet, H., Vakkari, V., Vana, M., and Kulmala, M., *Atmospheric ions and nucleation: a review of observations.* Atmospheric Chemistry and Physics, 2011. **11**(2): p. 767-798.
22. Kulmala, M., Vehkamaki, H., Petaja, T., Dal Maso, M., Lauri, A., Kerminen, V.M., Birmili, W., and McMurry, P.H., *Formation and growth rates of ultrafine atmospheric particles: a review of observations.* Journal of Aerosol Science, 2004. **35**(2): p. 143-176.
23. Angel, L. and Stace, A.J., *Reappraisal of the contribution from [O2(H2O)n]+ cluster ions to the chemistry of the ionosphere.* Journal of Physical Chemistry A, 1999. **103**(16): p. 2999-3005.
24. Ojekull, J., Andersson, P.U., Pettersson, J.B.C., Markovic, N., Thomas, R.D., Al Khalili, A., Ehlerding, A., Osterdahl, F., af Ugglas, M., Larsson, M., Danared, H., and Kallberg, A., *Dissociative recombination of water cluster ions with free electrons: Cross sections and branching ratios.* Journal of Chemical Physics, 2008. **128**(4): p. 044311/1-044311/9.
25. Thomas, R.D., Zhaunerchyk, V., Hellberg, F., Ehlerding, A., Geppert, W.D., Bahati, E., Bannister, M.E., Fogle, M.R., Vane, C.R., Petrignani, A., Andersson, P.U., Ojekull, J., Pettersson, J.B.C., van der Zande, W.J., and Larsson, M., *Hot Water from Cold. The Dissociative Recombination of Water Cluster Ions.* Journal of Physical Chemistry A, 2010. **114**(14): p. 4843-4846.
26. Ojekull, J., Andersson, P.U., Nagard, M.B., Pettersson, J.B.C., Markovic, N., Derkatch, A.M., Neau, A., Al Khalili, A., Rosen, S., Larsson, M., Semaniak, J.,

Danared, H., Kallberg, A., Osterdahl, F., and af Ugglas, M., *Dissociative recombination of H+(H2O)3 and D+(D2O)3 water cluster ions with electrons: Cross sections and branching ratios.* Journal of Chemical Physics, 2007. **127**(19): p. 194301/1-194301/8.
27. Coffman, D.J. and Hegg, D.A., *A Preliminary-Study of the Effect of Ammonia on Particle Nucleation in the Marine Boundary-Layer.* Journal of Geophysical Research-Atmospheres, 1995. **100**(D4): p. 7147-7160.
28. Berndt, T., Boge, O., and Stratmann, F., *Formation of atmospheric H2SO4/H2O particles in the absence of organics: A laboratory study.* Geophysical Research Letters, 2006. **33**(15): p. L15817/1-L15817/5.
29. Berndt, T., Stratmann, F., Sipila, M., Vanhanen, J., Petaja, T., Mikkila, J., Gruner, A., Spindler, G., Mauldin, R.L., Curtius, J., Kulmala, M., and Heintzenberg, J., *Laboratory study on new particle formation from the reaction OH + SO2: influence of experimental conditions, H2O vapour, NH3 and the amine tert-butylamine on the overall process.* Atmospheric Chemistry and Physics, 2010. **10**(15): p. 7101-7116.
30. Zhang, R.Y., *Getting to the Critical Nucleus of Aerosol Formation.* Science, 2010. **328**(5984): p. 1366-1367.
31. Perkins, M.D. and Eisele, F.L., *First mass-spectrometric measurements of atmospheric ions at ground level.* Journal of Geophysical Research [Atmospheres], 1984. **89**(D6): p. 9649-9657.
32. Eisele, F.L., *First tandem mass spectrometric measurement of tropospheric ions.* Journal of Geophysical Research [Atmospheres], 1988. **93**(D1): p. 716-24.
33. Schulte, P. and Arnold, F., *Pyridinium Ions and Pyridine in the Free Troposphere.* Geophysical Research Letters, 1990. **17**(8): p. 1077-1080.
34. Beig, G. and Brasseur, G.P., *Model of tropospheric ion composition: A first attempt.* Journal of Geophysical Research [Atmospheres], 2000. **105**(D18): p. 22671-22684.
35. Lide, D.R., *Proton Affinities*, in *CRC Handbook of Chemistry and physics, internet version 2006*. 86th ed. Lide, D.R., Editor. 2006, Taylor and Francis: Boca Raton, FL, USA.
36. Saintjalm, Y. and Moreetesta, P., *Study of Nitrogen-Containing Compounds in Cigarette-Smoke by Gas Chromatography-Mass Spectrometry.* Journal of Chromatography, 1980. **198**(2): p. 188-192.
37. Clemo, G.R., *Some Aromatic Basic Constituents of Coal Soot.* Tetrahedron, 1973. **29**(23): p. 3987-3990.
38. Beig, G., *Global change induced trends in ion composition of the troposphere to the lower thermosphere.* Annales Geophysicae, 2008. **26**(5): p. 1181-1187.
39. Eisele, F.L., *Identification of Tropospheric Ions.* Journal of Geophysical Research [Atmospheres], 1986. **91**(D7): p. 7897-7906.
40. Atkinson, R., Tuazon, E.C., Wallington, T.J., Aschmann, S.M., Arey, J., Winer, A.M., and Pitts, J.N., *Atmospheric Chemistry of Aniline, N,N-Dimethylaniline, Pyridine, 1,3,5-Triazine, and Nitrobenzene.* Environmental Science & Technology, 1987. **21**(1): p. 64-72.
41. Yeung, L.Y. and Elrod, M.J., *Experimental and computational study of the kinetics of OH + pyridine and its methyl- and ethyl-substituted derivatives.* Journal of Physical Chemistry A, 2003. **107**(22): p. 4470-4477.
42. Zhao, Z., Huskey, D.T., Olsen, K.J., Nicovich, J.M., McKee, M.L., and Wine, P.H., *Kinetics, mechanism, and thermochemistry of the gas-phase reaction of atomic*

chlorine with pyridine. Physical Chemistry Chemical Physics, 2007. **9**(31): p. 4383-4394.
43. Tanner, D.J. and Eisele, F.L., *Ions in Oceanic and Continental Air Masses.* Journal of Geophysical Research [Atmospheres], 1991. **96**(D1): p. 1023-1031.
44. Junninen, H., Ehn, M., Petaja, T., Luosujarvi, L., Kotiaho, T., Kostiainen, R., Rohner, U., Gonin, M., Fuhrer, K., Kulmala, M., and Worsnop, D.R., *A high-resolution mass spectrometer to measure atmospheric ion composition.* Atmospheric Measurement Techniques, 2010. **3**(4): p. 1039-1053.
45. Ehn, M., Junninen, H., Petaja, T., Kurten, T., Kerminen, V.M., Schobesberger, S., Manninen, H.E., Ortega, I.K., Vehkamaki, H., Kulmala, M., and Worsnop, D.R., *Composition and temporal behavior of ambient ions in the boreal forest.* Atmospheric Chemistry and Physics, 2010. **10**(17): p. 8513-8530.
46. Csaszar, A.G., Czako, G., Furtenbacher, T., Tennyson, J., Szalay, V., Shirin, S.V., Zobov, N.F., and Polyansky, O.L., *On equilibrium structures of the water molecule.* Journal of Chemical Physics, 2005. **122**(21): p. 214305/1-214305/10.
47. Andersson, P.U. and Pettersson, J.B.C., *Ionization of water clusters by collisions with graphite surfaces.* Zeitschrift Fur Physik D-Atoms Molecules and Clusters, 1997. **41**(1): p. 57-62.
48. Andersson, P.U., Tomsic, A., Andersson, M.B., and Pettersson, J.B.C., *Emission of small fragments during water cluster collisions with a graphite surface.* Chemical Physics Letters, 1997. **279**(1-2): p. 100-106.
49. Andersson, P.U. and Pettersson, J.B.C., *Water cluster collisions with graphite surfaces: Angular-resolved emission of large cluster ions.* Journal of Physical Chemistry B, 1998. **102**(38): p. 7428-7433.
50. Buck, U. and Huisken, F., *Infrared spectroscopy of size-selected water and methanol clusters.* Chemical Reviews, 2000. **100**(11): p. 3863-3890.
51. Ervin, K.M. and Armentrout, P.B., *Translational Energy Dependence of Ar+ + XY -> ArX+ + Y (XY=H2, D2, HD) from Thermal to 30 Ev c.m.* Journal of Chemical Physics, 1985. **83**(1): p. 166-189.
52. Bowers, M.T., Su, T., and Anicich, V.G., *Theory of ion-polar molecule collisions. Kinetic energy dependence of ion-polar molecule reactions: CH3OH+ + CH3OH -> CH3OH2+ + CH3O*.* Journal of Chemical Physics, 1973. **58**(11): p. 5175-5176.
53. Su, T. and Bowers, M.T., *Ion Polar Molecule Collisions. Proton Transfer Reactions of H3+ and CH5+ to the Geometric Isomers of Difluoroethylene, Dichloroethylene, and Difluorobenzene.* Journal of the American Chemical Society, 1973. **95**(5): p. 1370-1373.
54. Kummerlowe, G. and Beyer, M.K., *Rate estimates for collisions of ionic clusters with neutral reactant molecules.* International Journal of Mass Spectrometry, 2005. **244**(1): p. 84-90.
55. Chantry, P.J., *Doppler Broadening in Beam Experiments.* Journal of Chemical Physics, 1971. **55**(6): p. 2746-2759.
56. Hansen, K., Andersson, P.U., and Uggerud, E., *Activation energies for evaporation from protonated and deprotonated water clusters from mass spectra.* Journal of Chemical Physics, 2009. **131**(12): p. 124303/1-124303/7.
57. Deheer, W.A., *The Physics of Simple Metal-Clusters - Experimental Aspects and Simple-Models.* Reviews of Modern Physics, 1993. **65**(3): p. 611-676.
58. Martin, T.P., *Shells of atoms.* Physics Reports, 1996. **273**(4): p. 199-241.
59. Lin, S.S., *Detection of Large Water Clusters by a Low rf Quadrupole Mass Filter.* Review of Scientific Instruments, 1973. **44**(4): p. 516-517.

60. Searcy, J.Q. and Fenn, J.B., *Clustering of Water on Hydrated Protons in a Supersonic Free Jet Expansion.* Journal of Chemical Physics, 1974. **61**(12): p. 5282-5288.
61. Zwier, T.S., *The structure of protonated water clusters.* Science, 2004. **304**(5674): p. 1119-1120.
62. McQuinn, K., Hof, F., and McIndoe, J.S., *Collision-induced dissociation of protonated nanodroplets.* International Journal of Mass Spectrometry, 2009. **279**(1): p. 32-36.
63. Shin, J.W., Hammer, N.I., Diken, E.G., Johnson, M.A., Walters, R.S., Jaeger, T.D., Duncan, M.A., Christie, R.A., and Jordan, K.D., *Infrared signature of structures associated with the H+(H2O)n (n=6 to 27) clusters.* Science, 2004. **304**(5674): p. 1137-1140.
64. Bunnett, J.F. and Jones, R.A.Y., *Names for Hydrogen-Atoms, Ions, and Groups, and for Reactions Involving Them.* Pure and Applied Chemistry, 1988. **60**(7): p. 1115-1116.
65. Honma, K. and Armentrout, P.B., *The mechanism of proton exchange: Guided ion beam studies of the reactions, H(H2O)n+ (n=1-4) + D2O and D(D2O)n+ (n=1-4) + H2O.* Journal of Chemical Physics, 2004. **121**(17): p. 8307-8320.
66. Yamaguchi, S., Kudoh, S., Okada, Y., Orii, T., Takeuchi, K., Ichikawa, T., and Nakai, H., *Size-dependent reaction cross section of protonated water clusters H+(H2O)n (n = 2-11) with D2O.* Journal of Physical Chemistry A, 2003. **107**(50): p. 10904-10910.
67. Mella, M. and Ponti, A., *Alternative low-energy mechanisms for isotopic exchange in Gas-phase D2O-H+(H2O)n reactions.* Chemphyschem, 2006. **7**(4): p. 894-903.
68. Meotner, M., *The Ionic Hydrogen-Bond and Ion Solvation. 2. Solvation of Onium Ions by one to seven H2O Molecules - Relations between Monomolecular, Specific, and Bulk Hydration.* Journal of the American Chemical Society, 1984. **106**(5): p. 1265-1272.
69. Gross, J.H., *Mass Spectrometry*. 2004, Springer: Berlin, Germany.
70. Matsuo, S., Kuniyoshi, H., and Miyake, Y., *Vapor pressure of ice containing D2O.* Science, 1964. **145**(3639): p. 1454-1455.
71. Shinohara, H., Nagashima, U., and Nishi, N., *Mass Spectroscopic Observation of an Enhanced Structural Stability of Water Ammonia Binary Clusters at n=20 in the Series (H2O)n(NH3)mH+ (0 Less-Than-or-Equal-to n + m Less-Than-or-Equal-to 32).* Chemical Physics Letters, 1984. **111**(4-5): p. 511-513.
72. Shinohara, H., Nagashima, U., Tanaka, H., and Nishi, N., *Magic Numbers for Water Ammonia Binary Clusters - Enhanced Stability of Ion Clathrate Structures.* Journal of Chemical Physics, 1985. **83**(8): p. 4183-4192.
73. Li, Y., Lu, R.C., Hu, Y.J., and Wang, X.Y., *Multiphoton ionization and ab initio calculation studies of pyridine-water mixed clusters using time of flight mass spectrometer.* Chemical Physics Letters, 2001. **333**(1-2): p. 153-161.
74. Yang, X. and Castleman, A.W., *Production and Magic Numbers of Large Hydrated Anion Clusters X-(H2O)n=0-59 (X = OH, O, O2, and O3) under Thermal Conditions.* Journal of Physical Chemistry, 1990. **94**(23): p. 8500-8502.
75. Khan, A., *Theoretical studies of NH4+(H2O)20 and NH3(H2O)20H+ clusters.* Chemical Physics Letters, 2001. **338**(2-3): p. 201-207.
76. Shriver, D.F., Atkins, P.W., and Langford, C.H., *Table 5.3. Gas phase and solution proton affinities of bases*, in *Inorganic Chemistry*. 1990, Oxford University Press: Oxford, UK.

77. Uggerud, E., *Calculated energy barriers for the identity SN2 reaction H2O + CH3OH2+ --> +H2OCH3 + OH2 in the gas phase, in water clusters, and in aqueous solution.* International Journal of Mass Spectrometry, 1999. **182-183**: p. 13-22.
78. Lide, D.R., *Dissociation Constants of Inorganic Acids and Bases*, in *CRC Handbook of Chemistry and physics, internet version 2006*. 86th ed. Lide, D.R., Editor. 2006, Taylor and Francis: Boca Raton, FL, USA.
79. Lide, D.R., *Dissociation Constants of Organic Acids and Bases*, in *CRC Handbook of Chemistry and physics, internet version 2006*. 86th ed. Lide, D.R., Editor. 2006, Taylor and Francis: Boca Raton, FL, USA.
80. Agmon, N., *The Grotthuss Mechanism.* Chemical Physics Letters, 1995. **244**(5-6): p. 456-462.
81. Viggiano, A.A., Dale, F., and Paulson, J.F., *Proton transfer reactions of H+(H2O)n=2-11 with methanol, ammonia, pyridine, acetonitrile, and acetone.* J. Chem. Phys., 1988. **88**(4): p. 2469-2477.
82. Viggiano, A.A., Morris, R.A., Dale, F., and Paulson, J.F., *Tropospheric Reactions of H+(NH3)m(H2O)n with Pyridine and Picoline.* Journal of Geophysical Research [Atmospheres], 1988. **93**(D8): p. 9534-9538.
83. Honma, K., Sunderlin, L.S., and Armentrout, P.B., *Reactions of Protonated Water Clusters with Deuterated Ammonia - H(H2O)n+ (n = 1-4) + ND3.* International Journal of Mass Spectrometry and Ion Processes, 1992. **117**(1-3): p. 237-259.
84. Diken, E.G., Hammer, N.I., Johnson, M.A., Christie, R.A., and Jordan, K.D., *Mid-infrared characterization of the NH4+(H2O)n clusters in the neighborhood of the n=20 "magic" number.* Journal of Chemical Physics, 2005. **123**(16): p. 164309/1-164309/7.
85. Schmidt, M., Masson, A., Brechignac, C., and Cheng, H.P., *Hydrogen peroxide and ammonia on protonated ice clusters.* Journal of Chemical Physics, 2007. **126**(15): p. 154315/1-154315/5.
86. Douady, J., Calvo, F., and Spiegelman, F., *Structure, stability, and infrared spectroscopy of (H2O)nNH4+ clusters: A theoretical study at zero and finite temperature.* Journal of Chemical Physics, 2008. **129**(15): p. 154305/1-154305-13.
87. Anick, D.J., *Topology-energy relationships and lowest energy configurations for pentagonal dodecahedral, (H2O)20X clusters, X=empty, H2O, NH3, H3O+: The importance of O-topology.* Journal of Chemical Physics, 2010. **132**(16): p. 164311/1-164311/12.
88. Hogg, A.M. and Kebarle, P., *Mass-Spectrometric Study of Ions at near-Atmospheric Pressure. 2. Ammonium Ions Produced by Alpha Radiolysis of Ammonia and Their Solvation in Gas Phase by Ammonia and Water Molecules.* Journal of Chemical Physics, 1965. **43**(2): p. 449-456.
89. Payzant, J.D., Cunningh, A.J., and Kebarle, P., *Gas-Phase Solvation of Ammonium Ion by NH3 and H2O and Stabilities of Mixed Clusters NH4+(NH3)n(H2O)w.* Canadian Journal of Chemistry-Revue Canadienne De Chimie, 1973. **51**(19): p. 3242-3249.